

EXPERIMENTAL DETERMINATION OF METAL SORPTION AND TRANSPORT  
PARAMETERS FOR GRAPHENE OXIDE

A Dissertation

Submitted to the Graduate School  
of the University of Notre Dame  
in Partial Fulfillment of the Requirements  
for the Degree of

Doctor of Philosophy

by

Thomas Alan Duster

---

Jeremy B. Fein, Director

Graduate Program in Civil Engineering and Geological Sciences

Notre Dame, Indiana

December 2013

© Copyright 2013

Thomas Alan Duster

EXPERIMENTAL DETERMINATION OF METAL SORPTION AND TRANSPORT  
PARAMETERS FOR GRAPHENE OXIDE

Abstract

by

Thomas Alan Duster

The goal of this dissertation is to measure the ability of graphene oxide (GO) to sorb protons and metals, and to assess its mobility in saturated porous media. In Chapter 2 and Chapter 3, we illustrate that multi-layered GO (MLGO) exhibits a striking capacity to buffer aqueous solutions and sorb metals, with the sorption behaviors being influenced in varying degrees by pH and ionic strength. We use surface complexation modeling to calculate equilibrium constants for the surface sorption reactions between MLGO and protons, Cd, Pb, and U(VI), and we account for ionic strength effects as a competition between the target adsorbate and Na from the background electrolyte. In Chapter 4, we use deposition rate coefficient measurements to establish that pH, ionic strength, and sand surface coatings all play critical roles in determining the transport of single-layered GO (SLGO) through laboratory columns. Collectively, the sorption and mobility measurements in this dissertation are tailored to better inform remediation strategies that employ GO as a sorbent in natural and engineered systems.

## CONTENTS

Figures.....	iv
Tables.....	viii
Acknowledgments.....	ix
Chapter 1: Introduction.....	1
Chapter 2: Surface Complexation Modeling of Proton and Metal Sorption onto Graphene Oxide.....	8
2.1 Abstract.....	8
2.2 Introduction.....	9
2.3 Experimental Procedures.....	12
2.3.1 GO Preparation and Characterization.....	12
2.3.2 Potentiometric Titrations.....	13
2.3.3 Batch Metal Sorption Studies.....	14
2.4 Results and Discussion.....	16
2.4.1 SLGO and MLGO Characterization.....	16
2.4.2 Potentiometric Titrations of GO Particles.....	16
2.4.3 Batch Metal Sorption onto GO Particles.....	22
2.4.4 Electrostatic Surface Complexation Modeling of Proton and Metal Sorption.....	25
2.4.5 Modeling the Competitive Interactions between Protons, Cd or Pb, and Na.....	26
2.4.6 A Proposed Model for Proton and Metal Sorption to MLGO Particles.....	36
2.5 Conclusions.....	41
2.6 Acknowledgments.....	45
Chapter 3: Sorption of Aqueous Uranyl Complexes to Multi-Layered Graphene Oxide.....	46
3.1 Abstract.....	46
3.2 Introduction.....	47
3.3 Experimental Procedures.....	49
3.3.1 MLGO Preparation and Characterization.....	49
3.3.2 Batch U-MLGO Sorption Studies.....	51
3.3.3 Chemical Equilibrium Modeling.....	52
3.4 Results and Discussion.....	55

3.4.1 MLGO Nanosheet Characterization. ....	55
3.4.2 MLGO-Free U Speciation Modeling .....	55
3.4.3 Batch U Sorption Experiments .....	58
3.5 Conclusions.....	63
3.6 Acknowledgments.....	63
Chapter 4: Influence of pH and Ionic Strength on the Deposition Rates of Single-Layered Graphene Oxide Nanosheets in Quartz and Iron Oxide coated Sand Columns .....	65
4.1 Abstract .....	65
4.2 Introduction.....	66
4.3 Experimental Procedures .....	68
4.3.1 SLGO Preparation and Characterization .....	68
4.3.2 Porous Media Preparation and Characterization.....	70
4.3.3 Column Transport Studies .....	72
4.3.4 Quantitative Characterization of Transport Parameters.....	74
4.4 Results and Discussion .....	77
4.4.1 SLGO Nanosheet Characterization.....	77
4.4.2 Porous Media Characterization.....	80
4.4.3 Electrokinetic Characterization of SLGO and Collector Grains.....	81
4.4.4 Column Transport Studies .....	83
4.4.5 Physical and Electrochemical Mechanisms Associated with Transport Behaviors.....	89
4.5 Conclusions.....	92
4.6 Acknowledgments.....	93
Chapter 5: Conclusions.....	94
Appendix A: Additional Details Regarding Surface Complexation Modeling .....	101
A.1 Chemical Equilibrium Modeling .....	101
A.2 Electrostatic Modeling of the Potentiometric Titration Data.....	105
A.3 Electrostatic Modeling of Batch Cd Sorption Modeling .....	109
Appendix B: Additional Figures and Tables for Chapter 2 .....	111
Appendix C: Additional Figures and Tables for Chapter 3 .....	124
Appendix D: Additional Figures and Tables for Chapter 4.....	127
Appendix E: Replicate Breakthrough Curves for Chapter 4 .....	130
Bibliography .....	135

## FIGURES

- Figure 1.1: A well-accepted structural model for GO from Lerf et al. (1998), which illustrates the presence of epoxide, hydroxyl, and carboxyl functional groups.....4
- Figure 2.1: AFM images and height profiles for the cross-sections indicated in green for: (a) SLGO nanosheets; and (b) MLGO particles. Note that the peak heights change from ~1.3 nm to ~10 nm, respectively. ....17
- Figure 2.2: Representative concentration-normalized forward and reverse titration data for two replicate MLGO systems. Some data points have been removed for clarity. Experimental conditions: 100 mM ionic strength / ~1 g MLGO L<sup>-1</sup>.....18
- Figure 2.3: Potentiometric titration curves for MLGO particles from all ionic strength treatments normalized to their own average value. The normalization process allows for direct comparison of curves without regard to initial protonation state of the MLGO particles. Collectively, these curves illustrate the relatively small influence of ionic strength on MLGO protonation behaviors.....20
- Figure 2.4: Sorption of Cd ( $8.9 \times 10^{-6}$  M) by GO ( $200 \text{ mg L}^{-1}$ ) as a function of both pH and ionic strength. Red, blue, black, and green circles indicate the sorption of Cd to MLGO particles in 1 mM, 10 mM, 100 mM, and 300 mM ionic strength treatments, respectively. Red and black ×'s indicate the sorption of Cd to SLGO nanosheets in 1 mM and 100 mM ionic strength treatments, respectively.....23
- Figure 2.5: Sorption of Pb ( $4.8 \times 10^{-6}$  M) by MLGO particles ( $20 \text{ mg L}^{-1}$ ) as a function of both pH and ionic strength. Red, blue, and black circles indicate the sorption of Pb to MLGO particles in 1 mM, 10 mM, and 100 mM ionic strength treatments, respectively. ....24
- Figure 2.6: Calculated  $\text{pK}_a$  values for Site 2 as a function of ionic strength assuming: (a) no Na competition at the surface site; or (b) a  $\text{Log } K_{\text{Na-ads}} = 2.0$ . The horizontal line is the average of the four ionic strength-specific  $\text{pK}_a$  values in each panel. Note that the range and average of the ionic strength-specific  $\text{pK}_a$  values increases incorporating Na competition into the modeling of the titrations. Similar plots for each site and  $\text{Log } K_{\text{Na-ads}}$  value are provided in Figure B.1. In addition, the results of these two plots are referenced in Figure 2.7. Each point on these figures represents the average  $\text{pK}_a$  value calculated from between three and seven potentiometric titration replicates for each ionic strength. ....31

Figure 2.7:  $pK_a$  values averaged across all ionic strengths for each of the four surface sites as a function of  $\text{Log } K_{Na-ads}$ . Error bars indicate the standard deviation from the four ionic strength-specific  $pK_a$  value for each surface site and  $\text{Log } K_{Na-ads}$  combination. For example, the data used to calculate the two treatments marked with a star are shown in more detail in Figure 2.6. Note that the magnitude of the standard deviations increases with increasing  $\text{Log } K_{Na-ads}$  values, indicating that larger  $\text{Log } K_{Na-ads}$  values result in a greater range of  $pK_a$  values with respect to ionic strength. Numerical average  $pK_a$  values ( $\pm 1\sigma$ ) are shown for the selected model, which is fully described in Section 2.4.6.  $pK_a$  values plotted at  $\text{Log } K_{Na-ads} = 0$  are those calculated from models that do not include a binding affinity for Na at each site. ....32

Figure 2.8: Sum of the squared residuals (SSR) between the site-specific  $pK_a$  values calculated for each ionic strength and the average  $pK_a$  value across all ionic strengths for each site. These values are plotted as a function of  $\text{Log } K_{Na-ads}$ . See Figure B.1 for the complete data set from which these values are calculated. ....34

Figure 2.9: Predictions of  $\text{Cd}^{2+}$  sorption behaviors against pH for each ionic strength using the selected non-electrostatic model that incorporates a  $\text{Log } K_{Na-ads} = 1.0$  for Na-MLGO interactions and assumes the following site combination and equilibrium constants: Site 1 ( $\text{Log } K_{ads} = 5.03$ ;  $pK_a = 4.55$ ), Site 2 ( $\text{Log } K_{ads} = 4.44$ ;  $pK_a = 6.52$ ), and Site 4 ( $\text{Log } K_{ads} = 6.81$ ;  $pK_a = 9.98$ ). Prediction curves are shown in relation to actual measured Cd sorption extents for each ionic strength treatment. Axes are as follows: X (pH); Y (%Cd Sorbed).....42

Figure 2.10: Predictions of Pb sorption behaviors against pH for each ionic strength using the selected non-electrostatic model that incorporates a  $\text{Log } K_{Na-ads} = 1.0$  for Na-MLGO interactions and assumes the following site combination and equilibrium constants: Site 1-Pb<sup>2+</sup> ( $\text{Log } K_{ads} = 6.01$ ;  $pK_a = 4.55$ ) and Site 2-PbOH<sup>+</sup> ( $\text{Log } K_{ads} = 8.42$ ;  $pK_a = 6.52$ ). Prediction curves are shown in relation to actual measured Pb sorption extents for each ionic strength treatment. See Table 2.3 for further details regarding reactions. Axes are as follows: X (pH); Y (%Pb Sorbed). ....43

Figure 3.1: AFM image and height profile for the cross-section indicated in green for a representative MLGO particle. Note that the peak heights are ~10 nm. ....56

Figure 3.2: Aqueous U speciation modeling for MLGO-free systems in equilibrium with atmosphere. Only species that exceed 5% abundance are shown. The U concentration in this model is 3 ppm ( $1.3 \times 10^{-5}$  M) and the ionic strength is 1 mM with NaClO<sub>4</sub> as the background electrolyte. The solution is in equilibrium with atmospheric CO<sub>2</sub>. Species abundances are nearly identical for all ionic strengths below 100 mM. ....57

Figure 3.3: Sorption of U ( $1.26 \times 10^{-5}$  M) by MLGO particles ( $210 \text{ mg L}^{-1}$ ) as a function of both pH and ionic strength. Red, blue, and black circles indicate the sorption edges for 1 mM, 10 mM, and 100 mM ionic strength treatments, respectively. ...59

Figure 3.4: Prediction of U sorption behavior using a non-electrostatic model that assumes sorption of  $UO_2^{2+}$  to Site 1 only, with a  $\text{Log } K_{ads} = 5.76$  for this reaction. Prediction curves are shown in relation to actual measured U sorption extents for three ionic strength treatments. Axes are as follows: X (pH); Y (%U Sorbed).....61

Figure 4.1: Two characteristic non-contact AFM images of SLGO nanosheets deposited on freshly-cleaved mica. Note the change in scale between images (a) and (b). Panel (c) illustrates the height or z-dimension profile from the cross-section depicted in green on Panel (b). Collectively, these panels indicate the dominant presence of SLGO nanosheets that have been completely exfoliated. ....78

Figure 4.2: Typical UV-vis absorption spectra for a 25 mg SLGO  $L^{-1}$  suspension before (black) and after (grey) passing through a column packed with a porous media. This particular example is from a quartz sand experimental treatment exhibiting an ionic strength of 50 mM and an effluent pH ~5.6. The inset figure illustrates the relationship between the pre- and post-column absorbance values, which remains constant throughout the wavelength range depicted. ....79

Figure 4.3: Representative SEM images of (a) an uncoated quartz sand grain, and (b) an iron oxide coated sand grain. Note the change in scale between the two images. EDX spectra from the indicated boxes illustrate an extensive presence of iron in (b).....80

Figure 4.4: Electrophoretic mobility (EPM) measurements titrated against pH for SLGO, quartz sand grains (surface-associated colloidal material), and iron oxide coated sand grains (surface-associated colloidal material) suspended in an electrolyte solution exhibiting an ionic strength of 10 mM and 50 mM. ....82

Figure 4.5: Breakthrough curves for (a) quartz sand columns, 10 mM ionic strength; (b) quartz sand columns, 50 mM ionic strength; (c) iron oxide coated sand columns, 10 mM, ionic strength; (d) iron oxide coated sand columns, 50 mM ionic strength. On all figures, red, green, and blue curves represent the average breakthrough curves for treatments with an influent pH of 8.3, 7.0, and 5.6, respectively. The black curve in each figure is the average breakthrough curve for the conservative NaBr tracer solution transported through quartz sand. pH values to the right of the breakthrough curves follow the convention *Influent pH/Effluent pH*. Continuous flow of the SLGO suspension occurred between 12.5 and 62.5 pore volumes (marked with black ×'s), with a pH-matched SLGO-free ionic strength buffer solution flowing through the column at all other times. Not shown on these figures is a 12.5 pore volume rinse with ultrapure water, which preceded each transport experiment. A horizontal grey line is placed at 18 pore volumes, where we measured the clean-bed breakthrough concentrations. ....84

Figure 4.6: Deposition rate coefficients ( $k_d$ ) and attachment efficiencies ( $\alpha$ ) for SLGO nanosheets transported through columns packed with quartz sand and iron oxide coated sand in the pH and ionic strength conditions noted. All  $k_d$  values were calculated from the breakthrough concentrations presented in Figure 4.5 and are

plotted against the average effluent pH values recorded for replicates from each treatment. ....86

Figure B.1:  $pK_a$  values for each MLGO surface site calculated from models that incorporate Na-MLGO interactions with the indicated value of  $\text{Log } K_{Na-ads}$ . These  $pK_a$  values are plotted as a function of ionic strength. Each point is calculated as the average  $pK_a$  from the modeling of three to seven potentiometric titration replicates, with error bars indicating the standard deviations. Replicate data are provided in Table B.4. Horizontal lines indicate the average  $pK_a$  for a given surface site and  $\text{Log } K_{Na-ads}$  treatment across ionic strength (i.e., the average  $pK_a$  within a given panel). The arrow in the top-left panel provides an illustration of the measured distance between an individual  $pK_a$  value and value depicted by the horizontal line. We define this distance as the *residual*, and the sum of all squared residuals (SSR) for a given row is provided at the end of each row. We define a successful model as one that yields calculated  $pK_a$  values from the experimental data that do not vary as a function of ionic strength, and thus we use the SSR values as the metric by which we evaluate this goal. ....112

Figure B.2: Modeled Cd speciation as a function of pH for 100 mM ionic strength systems containing 1 ppm Cd. Speciation plots for all ionic strength solutions between 1 mM and 300 mM are virtually identical. ....114

Figure B.3: Modeled Pb speciation as a function of pH for 100 mM ionic strength systems containing 1 ppm Pb. Speciation plots for all ionic strength solutions between 1 mM and 300 mM are virtually identical. ....115

Figure C.1: Predicted of U sorption behavior using a non-electrostatic model that assumes sorption of  $UO_2^{2+}$  to Site 1 only ( $\text{Log } K_{ads} = 5.76$ ) and a  $\text{Log } K_{Na-ads} = 1.0$ . Prediction curves are shown in relation to actual measured replicate U sorption extents for three ionic strength treatments. Axes are as follows: X (pH); Y (%U Sorbed). ....126

Figure D.1: Regression analysis showing a linear relationship between SLGO concentration and UV-vis absorbance at  $\lambda = 230$  nm. ....128

Figure D.2: Breakthrough of the conservative NaBr tracer through quartz sand in the electrochemical environments listed in the figure legend. Virtually all breakthrough curves directly overlapped, so we averaged them and used this average curve for comparison to SLGO nanosheet transport, as depicted in Figure 4.5 in the text. ....129

## TABLES

Table 1.1 Maximum GO Sorption Capacities for Several Different Elements or Compounds .....	6
Table 2.1 Experimental Conditions for Batch Metal Sorption Studies .....	15
Table 2.2 Site Concentrations and V(Y) Values for Every 4-Site NEM Tested in this Study .....	22
Table 2.3 Stability Constant Values for Metal-MLGO Surface Sorption Reactions for the Selected Model.....	40
Table 3.1 MLGO Site Concentrations and Acidity Constants from a 4-Site Non-Electrostatic Surface Complexation Model .....	53
Table 3.2 Stability Constant Values for the Uranyl-MLGO Sorption Reaction Calculated using A Non-Electrostatic Surface Complexation Model .....	61
Table A.1 Site Concentrations and Acidity Constants from the Non-Electrostatic and Electrostatic Surface Complexation Modeling .....	107
Table A.2 Cd-MLGO Stability Constants Calculated from a CCM for each Ionic Strength Treatment .....	110
Table B.1 Log K values for Cd and Pb Aqueous Complexation Reactions Utilized in FITEQL.....	116
Table B.2 Calculated Stability Constants for Cd-MLGO Interactions for Models that Incorporate Varying Affinities Associated with Na-MLGO Binding .....	117
Table B.3 Calculated Stability Constants for Pb-MLGO Interactions for Models that Incorporate Varying Affinities Associated with Na-MLGO Binding .....	118
Table B.4 Site Concentrations and Acidity Constants for Each Experimental Replicate as a Function of Ionic Strength and Na-MLGO Affinity .....	119
Table C.1 Log K Values for Aqueous Uranyl Complexation Reactions Utilized in FITEQL.....	125

## ACKNOWLEDGMENTS

Numerous people assisted and supported me during my journey at the University of Notre Dame. First and foremost, I sincerely thank my advisor, Dr. Jeremy Fein, for his expert insights during my development as a scientist, as well as his patience and understanding during my development as a new husband and father. I acknowledge the efforts of Jennifer Szymanowski, who provided substantial technical assistance with experiments and instrumentation. I recognize the helpful technical contributions from and discerning discussions with my committee members and collaborators, including Dr. Chongzheng Na, Dr. Diogo Bolster, Dr. Amy Hixon, Dr. Bruce Bunker, and Allison Showalter. I am thankful for the mentorship provided by the late Dr. J. Keith Rigby, Jr., whose kindness will never be forgotten. I also sincerely appreciate the friendships I developed with my labmates.

Finally, I cannot begin to fathom how difficult the last four years could have been without the love, support, and escape provided by my wife Kathy and son Russell. You sacrificed significantly so that your husband/*Daddy* could live out a dream, and I am forever indebted to you both. In addition, I would be remiss if I did not recognize the efforts of my own parents, who provided a loving and stable home where I could focus on personal development and learning, which ultimately culminated in this dissertation.

In homage to all the incredibly hard work of the people recognized above, I use the personal pronouns *we* and *our* rather than *I* or *my* throughout this dissertation.

## CHAPTER 1: INTRODUCTION

Given its relationship to the written word, natural flake graphite – the primary component of pencil *lead* – has been an integral part of scientific endeavor for generations. In laboratory notebooks around the world, graphite marks on a page undoubtedly recorded many of the greatest discoveries of our time. However, for most of us, our intuitive understanding of graphite stopped there, with its direct use in our daily lives, without realizing that the actual material being deposited in those marks would someday revolutionize multiple fields of contemporary science. In fact, the research described within this dissertation focuses on characterizing the extraordinary properties of one graphitic derivative – graphene oxide – and its potential applications in chemical capture and environmental remediation.

At the nanoscale, natural flake graphite is comprised of atomically-thin laminations, with each layer consisting of a regular hexagonal lattice of  $sp^2$  bonded carbon atoms (Novoselov et al., 2004; Allen et al., 2010). With the proper force and angle, graphite is rather crudely deposited onto a page while writing via the cleavage of this layered structure along the planar boundaries [for an analytical treatment of this process, see Zhang et al. (2005)]. However, cleavage can also occur more methodically via a process called micromechanical exfoliation. In 2004, using what is now colloquially referred to as the *Scotch-tape method*, Drs. Andre Geim and Konstantin

Novoselov from the University of Manchester (U.K.) successively peeled apart highly-oriented pyrolytic graphite until they had isolated individual laminations, called graphene nanosheets, measuring only a single atom in thickness. Their isolation and initial characterization of the amazing electric properties of graphene (Novoselov et al., 2004) won Geim and Novoselov a Nobel Prize in Physics only six short years later (Geim, 2011).

In the years since, the demand for graphene has necessitated scaled-up production alternatives. Rather than the intensive mechanical peeling techniques, these new approaches have thus far focused on batch-based chemical exfoliation methods (Stankovich et al., 2007; Li et al., 2008; Wang et al., 2008; Park and Ruoff, 2009; Zhang et al., 2010). During this process, flake graphite is exposed to a strong mix of acids and chemical oxidants, which serves to interrupt and/or decorate the stacked six-membered graphene rings with various oxygen-containing functional groups on both the edges and basal planes. This intermediate oxidized form of graphite has been called graphitic acid (Brodie, 1859), graphite oxide (Nakajima and Matsuo, 1994; Cassagneau and Fendler, 1998; Lerf et al., 1998), or multi-layered graphene oxide (Acik et al., 2010; Kim et al., 2012) by various researchers [herein, we generally refer to all oxidized forms of graphite as graphene oxide (GO)]. The electrostatic repulsion between the functional groups on the consecutive layers of GO *loosens* the laminations, allowing either sonication or another energy input to exfoliate the bulk material into single-layered GO nanosheets.

If the goal is to create exfoliated graphene, the GO can then be chemically reduced, resulting in a suspension of nanosheets that closely resemble the structure of graphene (Zhang et al., 2010; Chua and Pumera, 2013). Nanosheets produced in this

manner are generally called chemically-reduced graphene oxide (e.g, Gómez-Navarro et al., 2007; Eda et al., 2008) or chemically-modified graphene (e.g, Dreyer et al., 2010) to distinguish them from the more pristine graphene sheets isolated via micromechanical exfoliation techniques. However, the GO intermediaries also exhibit an array of interesting characteristics, including tunable optical and electronic properties (Loh et al., 2010), an ability to self-assemble into free-standing membranes (Chen et al., 2009), and a striking capacity to sorb chemical contaminants (Lü et al., 2012). The last of these characteristics will be further illustrated by subsequent sections of this dissertation.

While graphene is a relatively new target of scientific investigation, the study of oxidized graphitic compounds extends over the past 150 years. For example, Brodie (1859) explored the reactivity and oxidation of graphite using fuming nitric acid and chlorate salts in a failed attempt to identify the molecular weight of graphite. Like graphene, GO can be exfoliated to a single atomically-thin nanosheet, but these nanosheets exhibit a high density of surface-associated proton-active functional groups. Since the initial investigations of Brodie, many studies have attempted to identify these groups on the GO surface. Multiple conceptual models have been formulated [see Dreyer et al. (2010) for a thorough review], yet a consensus structure for GO remains elusive.

Early structural models using elemental composition, reactivity, and X-ray diffraction provided a framework for later investigation using more advanced techniques. One of the first studies using solid state nuclear magnetic resonance (NMR) to characterize the laminations of GO and gain wide acceptance was by Lerf et al. (1998), which illustrated that the structure of GO nanosheets consists of unoxidized aromatic benzene rings and aliphatic regions randomly distributed across the nanosheet surface.

The aliphatic regions on the basal planes are primarily comprised of epoxide (1,2-ether) functional groups, while nanosheet edges are terminated with hydroxyl or carboxyl groups (Figure 1.1). Notable updates to the model of Lerf et al. by Szabó et al. (2006a) and Gao et al. (2009) provide evidence for ketone groups and five- or six-membered lactol rings, respectively, although each still identifies epoxide and hydroxyls as the most abundant functional groups on the GO surface. Adding to the overall complexity in describing the structure of graphitic materials, the identity of surface functional groups are likely influenced by the type and quality of graphite used (Seredych et al., 2009) and the level of oxidation achieved (Lerf et al., 1998; Szabó et al., 2006a), which limits the ability to establish structural agreement.

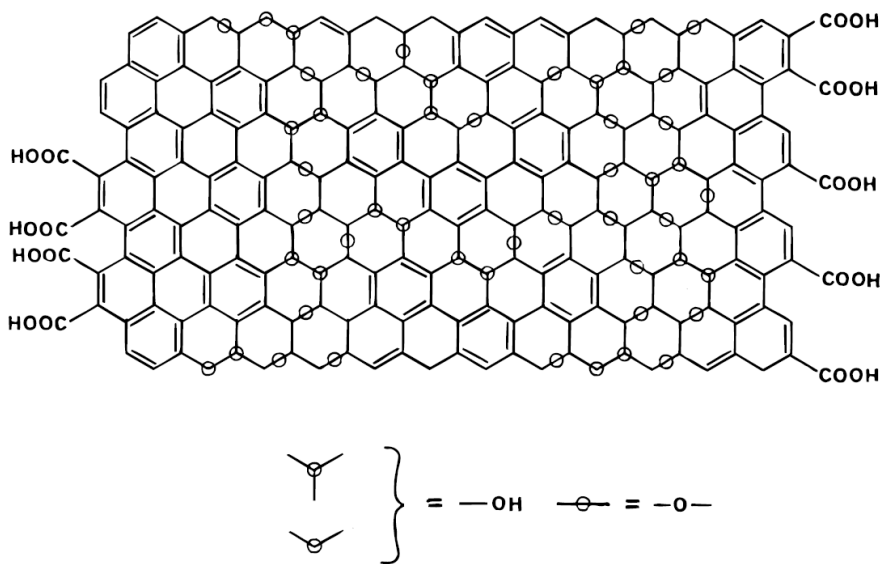


Figure 1.1: A well-accepted structural model for GO from Lerf et al. (1998), which illustrates the presence of epoxide, hydroxyl, and carboxyl functional groups.

Regardless of the exact structures involved, the extremely high surface area to mass ratio and the significant presence of a variety of proton-active functional groups on the GO surface result in an extraordinary capacity to sorb a variety of environmental contaminants. For example, the maximum sorption capacities for a variety of organic and inorganic compounds are provided in Table 1.1. In particular, the high capacity of GO to sorb metal cations from solution suggests potential for use in water treatment and reuse, or in *in situ* or *ex situ* remediation applications for metal-contaminated environments (Gao et al., 2011; Lü et al., 2012).

In order to make optimal use of GO in these applications, several largely unexplored topics need to be addressed. First, equilibrium modeling that results in *intrinsic* equilibrium constants for the reactions between GO functional groups and both protons and metals can aid in optimizing the size of the batch reactor, the material dose, and the operational parameters needed for treatment operations. To date, nearly all existing metal sorption studies [except Sun et al. (2012) which investigated Eu sorption onto GO] use non-mechanistic sorption approaches, such as Langmuir/Freundlich isotherms, that result in partitioning coefficients for metal-GO interactions. The application of the resulting models is therefore limited because partitioning coefficients can vary with pH, ionic strength, or the ionic composition of the solution (Bethke and Brady, 2000; Koretsky, 2000). Second, particularly for *in situ* remediation methods, an estimate of the mobility of GO through various types of soil and groundwater environments will be required to determine the extent to which these nanosheets can facilitate either contaminant removal or permanent retention within the matrix. A recent report from Lanphere et al. (2013) investigates the transport of GO nanosheets through

TABLE 1.1  
 MAXIMUM GO SORPTION CAPACITIES FOR SEVERAL DIFFERENT  
 ELEMENTS OR COMPOUNDS

Element/Compound	Maximum Sorption Capacity (mg g <sup>-1</sup> )	Environmental Conditions pH / Ionic Strength / Temp.	Citation
<i>Cd(II)</i>	106	pH 6.0 / 0.01 M / 303 K	Zhao et al. (2011a)
<i>Cd(II)</i>	530	pH 5.0 / NR / 298 K	Sitko et al. (2013)
<i>Co(II)</i>	682	pH 6.0 / 0.01 M / 303 K	Zhao et al. (2011a)
<i>Cu (II)</i>	47	pH 5.0 / NR / RT	Yang et al. (2010)
<i>Cu (II)</i>	294	pH 5.0 / NR / 298 K	Sitko et al. (2013)
<i>Eu (III)</i>	175	pH 6.0 / 0.01 M / 298 K	Sun et al. (2012)
<i>Pb(II)</i>	842	pH 6.0 / 0.01 M / 293 K	Zhao et al. (2011b)
<i>Pb(II)</i>	1119	pH 5.0 / NR / 298 K	Sitko et al. (2013)
<i>U(VI)</i>	98	pH 5.0 / 0.01 M / 293K	Zhao et al. (2012)
<i>Zn(II)</i>	345	pH 5.0 / NR / 298 K	Sitko et al. (2013)
<i>Humic Acid</i>	190	pH 5.0 / NR / 303K	Hortono et al (2009)
<i>Methylene Blue</i>	1939	pH 5.0 / NR / 293 K	Zhang et al. (2011)
<i>Phenol</i>	213	pH 6.0 / NR / RT	Ion et al. (2011)
<i>Tetracycline</i>	313	pH 3.6 / NR / 298K	Gao et al. (2012)

NR = Not reported  
 RT = Room temperature

quartz sand, but these initial findings need both validation and to be extended to other types of environmental systems.

Hence, the goal of this dissertation is to conduct experiments that result in sorption and transport parameters useful in metal remediation system design. In Chapter 2, we test several different surface complexation modeling approaches for their abilities to account for proton, Cd, and Pb binding onto the functional groups associated with multi-layered GO (MLGO) surfaces. We use MLGO particles, as opposed to more

exfoliated GO nanosheets, as their larger size facilitates removal from suspension during treatment operations. The results of this study indicate that MLGO particles exhibit large buffering capacities and a significant ability to remove Cd and Pb from environmentally-relevant aqueous solutions. We then calculate equilibrium constants for the relevant complexation reactions between MLGO surface sites and protons/metals that can be used to predict sorption behaviors throughout a range of environmental conditions. In Chapter 3, we examine U-MLGO interactions and quantify the affinity between MLGO surface sites and aqueous uranyl complexes. The results suggest that MLGO could be used as a selective sorbent for U in co-contaminated environments or those exhibiting high concentrations of electrolytes (e.g., brackish waters). Finally, in Chapter 4, we use laboratory column experiments to evaluate the mobility of single-layered GO (SLGO) through quartz and iron oxide coated sand media. The results of this study indicate that increasing deposition occurs with increasing ionic strength and decreasing pH, and in environments dominated by iron oxide coated sands. Collectively, the findings of these three studies are expected to inform remediation strategies that employ GO as a sorbent.

CHAPTER 2:  
SURFACE COMPLEXATION MODELING OF PROTON AND METAL SORPTION  
ONTO GRAPHENE OXIDE

2.1 Abstract

The objective of this investigation was to develop a surface complexation modeling approach to account for proton and metal (Cd, Pb) binding onto the surface of multi-layered graphene oxide (MLGO). The experimental approach required both potentiometric titrations of MLGO particles and batch metal sorption studies conducted between approximately pH 2 and pH 10 in 1 mM, 10 mM, 100 mM, and 300 mM NaClO<sub>4</sub> solutions to buffer ionic strength. The results of these investigations illustrate that MLGO particles exhibit large buffering and metal sorption capacities across a wide range of pH. While the potentiometric titration data indicate very little influence of ionic strength on MLGO buffering, the batch metal sorption data illustrate that increases in ionic strength substantially diminish the sorption of Cd or Pb by the MLGO surface. This difference in the sorption behaviors for protons and metals was best modeled using a 4-site non-electrostatic surface complexation model that accounts for ionic strength effects as a competition between Na and Cd or Pb for available MLGO sorption sites. Using this approach, titration data were used to constrain the site concentrations and pK<sub>a</sub> values for MLGO binding sites. The pK<sub>a</sub> values ( $\pm 1\sigma$ ) were calculated as 4.55 ( $\pm 0.91$ ), 6.52 ( $\pm 0.49$ ), 8.48 ( $\pm 0.21$ ), and 9.98 ( $\pm 0.21$ ). Using the proton-active site concentrations and

acidity constants determined from the potentiometric titrations, we used the metal sorption data to determine thermodynamic stability constants for each of the important Cd- and Pb-MLGO surface complexes. These findings illustrate the striking capacity of MLGO particles to sorb metals from aqueous solutions and highlight their potential usefulness in remediation applications. The site concentrations and equilibrium constants provided by this study can be used to tailor remediation approaches to specific water chemistries.

## 2.2 Introduction

Graphene oxide (GO) is produced from the oxidation and subsequent exfoliation of natural flake graphite. Single-layered GO (SLGO) nanosheets exhibit a thickness of only one atom, while few-layered (FLGO) and many-layered (MLGO) GO particles (also called graphite oxide) maintain a stacked arrangement of individual laminations. The exact chemical structure of GO is still a topic of significant debate in the literature (Dreyer et al., 2010), but it is generally agreed that chemical oxidation of the aromatic six-member carbon rings results in covalently-bonded epoxide, ketone, and hydroxyl functional groups on the basal planes, and carboxylic, lactol, and phenolic functional groups at the nanosheet edges (Lerf et al., 1998; Szabó et al., 2006a; Gao et al., 2009; Lee et al., 2010). However, the structure of GO may vary depending on the type and quality of graphite used, and the level of oxidation, which can impart distinct chemical characteristics (Szabó et al., 2006b; Seredych et al., 2009).

The extremely high surface area to mass ratio and the presence of a variety of proton-active functional groups on the GO surface result in a significant capacity to sorb

a variety of environmental contaminants. For example, GO and/or graphite oxide can serve as effective sorbents for humic acid (Hartono et al., 2009), cationic dyes (Zhang et al., 2011), ammonia (Petit et al., 2009), antibiotics (Gao et al., 2012), and organic (Ion et al., 2011; Liu et al., 2011) and metal contaminants (Lü et al., 2012) in polluted environments or engineered systems. In fact, GO nanosheets exhibit higher maximum sorption capacities (pH 5 to pH 6) for Pb (II) (1119 mg g<sup>-1</sup>), Cd (II) (530 mg g<sup>-1</sup>), Zn (II) (345 mg g<sup>-1</sup>), Cu (II) (294 mg g<sup>-1</sup>), U(VI) (98 mg g<sup>-1</sup>), and Co (II) (68 mg g<sup>-1</sup>) than any other currently-reported material (Yang et al., 2010; Zhao et al., 2011a, 2011b, 2012; Sitko et al., 2013). The high capacity of GO to sorb metal cations from solution suggests potential for use in water treatment and reuse, or in *in situ* or *ex situ* remediation applications for metal-contaminated environments.

In order to make optimal use of GO in these applications, equilibrium modeling is needed to determine material dose, reactor size, and operational parameters. Previous studies demonstrate metal sorption capacities of GO nanosheets by applying non-mechanistic models, such as Langmuir/Freundlich isotherms, which result in partitioning coefficients that vary as a function of the solution composition for which they were determined. Hence, the results of these sorption models cannot be applied with confidence to environments exhibiting different pH, adsorbate concentrations, or concentrations of competing cations and/or metal-binding ligands, relative to those directly studied in the laboratory. In contrast, the *intrinsic* equilibrium constants determined using surface complexation modeling are invariant with respect to most parameters which affect partitioning coefficients (Bethke and Brady, 2000; Koretsky, 2000), and therefore, would yield a more flexible and mechanistic model of metal

sorption onto GO nanosheets. Using this approach, we can determine discrete equilibrium constants in systems that isolate specific sorption reactions, and then combine the results into computational models that quantify the effects of GO sorption on the distribution and speciation of metals in more complex engineered or natural geologic systems.

In this study, we tested several different surface complexation modeling approaches for their abilities to account for proton and metal binding onto GO surfaces and enhance our molecular-scale understanding of these interactions. We used acid/base potentiometric titration experiments conducted as a function of ionic strength to provide constraints on the number of proton-active site types on the GO surface, their acidity constant ( $K_a$ ) values and their site concentrations. We also conducted bulk metal (Cd, Pb) sorption experiments as a function of pH under three to four ionic strength conditions in order to constrain the number of sites involved in metal binding, their pH ranges of influence, and the thermodynamic stability constants ( $K_{ads}$ ) for the important metal-GO surface complexes. This study focuses primarily on MLGO particles, as their larger size allows them to be more easily sedimented than SLGO or FLGO in an engineered remediation system, and therefore makes them more practical to separate from aqueous solutions during treatment operations. However, some potentiometric titrations and metal sorption experiments were also conducted using SLGO nanosheets to address specific research questions, as detailed in the following sections.

## 2.3 Experimental Procedures

### 2.3.1 GO Preparation and Characterization

GO nanosheets were synthesized from natural flake graphite (Alfa Aesar, 99.9995%) using the Hummer's method (Hummers and Offeman, 1958). Briefly, graphite was mixed with  $\text{NaNO}_3$ ,  $\text{H}_2\text{SO}_4$ , and  $\text{KMnO}_4$  in an ice bath. The mixture was then transferred to a water bath at 35 °C and stirred for 30 minutes. Next, ultrapure water ( $R > 18 \text{ M}\Omega \text{ cm}$ ,  $\text{TOC} < 2 \mu\text{gC L}^{-1}$ ) was added and the mixture was stirred for approximately 20 minutes. Residual permanganate was then consumed by the addition of hydrogen peroxide. Finally, GO was collected by centrifugation, washed repeatedly with ultrapure water, and freeze-dried under vacuum for 5 to 7 days before use.

The resulting dried mass was dispersed in ultrapure water using end-over-end rotation over a period of approximately 3 hours. Once fully suspended, MLGO particles were concentrated by repeatedly sedimenting the suspension under centrifugation ( $4000 \times g$  for 5 minutes), decanting the supernatant, and resuspending the pellet in fresh ultrapure water. After substantial removal of the SLGO/FLGO nanosheets that remained suspended during the centrifugation process, the sedimented material was resuspended a final time and these solutions were retained for potentiometric titration and batch metal sorption experiments. Conversely, SLGO nanosheets were concentrated via sonication of the dispersed suspension in a water bath for one hour, followed by centrifugation for 10 minutes at  $3000 \times g$ . In this case, the supernatant was retained and utilized for potentiometric titration and batch metal sorption experiments. Final MLGO and SLGO concentrations were determined as the difference between the wet and dry (105 °C for >24 hours) masses of a 20 mL aliquot of each final suspension. From this procedure, we

determined that each of the stock concentrations averaged  $\sim 2 \text{ g GO L}^{-1}$  suspension, with an inherent pH of between 2.8 and 3.2.

We characterized the physical properties of the MLGO particles and SLGO nanosheets used in subsequent sorption experiments using atomic force microscopy (AFM; XE-70, Park Systems, Santa Clara, CA). Aliquots from both the MLGO and SLGO stock suspensions were diluted 1:4 with ethanol and deposited on freshly cleaved mica. The instrument was operated in non-contact mode and images were flattened using the WSxM software package from Nanotec Electronica S.L. (Madrid, Spain). The AFM analyses resulted in determination of z-dimension, or height, which we used to infer the extent of exfoliation present in the suspension.

### 2.3.2 Potentiometric Titrations

We performed potentiometric titrations on  $\sim 1 \text{ g MLGO L}^{-1}$  suspensions under a  $\text{N}_2$ -headspace using an automated acid-base titrator (MT-70, Mettler-Toledo, Columbus, OH). To buffer ionic strength, we added appropriate quantities of  $\text{NaClO}_4$  to each suspension, such that the resulting initial ionic strength in the titrated solutions was 1 mM, 10 mM, 100 mM, or 300 mM. These suspensions were then purged with  $\text{N}_2$  for more than 20 minutes and immediately loaded for analysis. We completed between three and seven titrations for each ionic strength. In addition, we performed three titrations of SLGO nanosheets suspended in a 100 mM solution of  $\text{NaClO}_4$  to buffer ionic strength using an identical approach.

The titrator utilizes an automatic burette assembly to deliver precisely measured quantities of standardized 1.0 M HCl and NaOH solutions. During continuous stirring with a Teflon-coated magnetic stir-bar, the 100 mM and 300 mM ionic strength MLGO

suspensions were first acidified to pH ~2.5, at which point a *forward* titration commenced by slowly basifying the suspension to pH ~10, followed by a *reverse* titration that returns the solution back to pH ~2.5. In order to minimize the change in ionic strength caused by the added titrant over the course of the titration, the 1 mM and 10 mM ionic strength treatments were titrated from their initial pH forward, without an initial acidification to pH 2.5, and we did not performed reverse titrations for these systems. Even with this methodological amendment, we note that the forward titrations contributed an additional ~4 mM (in the form of H<sup>+</sup> ions) to the initial ionic strength.

The continuous monitoring of added titrant volumes and pH (i.e., a measure of the activity of free H<sup>+</sup> in solution in mol L<sup>-1</sup>), and the known concentration of MLGO in suspension, combine to ensure that these titrations result in a mass balance of acid and base in the system per gram of MLGO [(C<sub>a</sub> - C<sub>b</sub>) / (g MLGO L<sup>-1</sup>)] along a continuum of pH. The net excess/deficit of protons then serves as input for surface complexation models to determine individual site concentrations for distinct proton-active functional groups, as well as their respective pK<sub>a</sub> values.

### 2.3.3 Batch Metal Sorption Studies

Suspensions of MLGO particles were evaluated for their ability to sorb Cd and Pb from solution. Experimental conditions for each metal-bearing system are provided in Table 2.1. Ionic strength was buffered by addition of appropriate concentrations of NaClO<sub>4</sub>, while pH was adjusted using 0.1 to 1.0M NaOH or HNO<sub>3</sub>. The pH adjustment altered the ionic strength of the suspension (though addition of H<sup>+</sup> or Na<sup>+</sup> ions) by as much as 10 mM, particularly for low pH systems. MLGO-free control experiments across the experimental pH range indicated significant loss of Pb from solution above pH

TABLE 2.1

## EXPERIMENTAL CONDITIONS FOR BATCH METAL SORPTION STUDIES

<b>Metal</b>	<b>[GO] (mg L<sup>-1</sup>)</b>	<b>[M<sup>2+</sup>] (ppm)</b>	<b>[M<sup>2+</sup>] (M)</b>	<b>pH Range</b>	<b>Ionic Strengths (mM)</b>
<b>Cd<sup>2+</sup></b>	<b>200</b>	<b>~1</b>	<b><math>8.9 \times 10^{-6}</math></b>	<b>2.0 - 9.5</b>	<b>1, 10, 100, 300</b>
<b>Pb<sup>2+</sup></b>	<b>20</b>	<b>~1</b>	<b><math>4.8 \times 10^{-6}</math></b>	<b>2.0 - 8.0</b>	<b>1, 10, 100</b>

8.0, likely due to Pb-hydroxide precipitation and subsequent filter losses. Hence, Pb sorption analyses were limited to pH conditions below 8.0. Final Cd and Pb concentrations were achieved by adding appropriate quantities of a parent metal stock solution consisting of a pH-neutralized inductively coupled plasma optical emission spectroscopy (ICP-OES) standards [Cd(NO<sub>3</sub>)<sub>2</sub> or Pb(NO<sub>3</sub>)<sub>2</sub> dissolved in 5% HNO<sub>3</sub>]. Starting with freshly-prepared parent MLGO and metal solutions, we conducted two replicate batches for each ionic strength studied.

Exposure of the dissolved metal to the MLGO particles occurred for at least 4 hours, as kinetic studies associated with similar batch metal sorption studies indicated a sorption steady state occurs within this length of time (data not shown). After the equilibration period, a final pH was measured, and the MLGO particles were removed from suspension by centrifugation (4000 × g for 5 minutes) and filtration of the supernatant through 0.2 μm PTFE syringe filters. The resulting solutions were acidified and analyzed via ICP-OES (Optima 2000DV, Perkin-Elmer, Waltham, MA) against aqueous metal standards diluted into the same ionic strength matrix utilized during the

sorption experiments. Using an approach identical to the one presented above, we also conducted batch Cd sorption experiments for SLGO nanosheets suspended in either 1 mM or 100 mM solutions of NaClO<sub>4</sub> to buffer ionic strength.

## 2.4 Results and Discussion

### 2.4.1 SLGO and MLGO Characterization

Figure 2.1 depicts representative AFM images of SLGO nanosheets and MLGO particles from the stock suspensions used in this study. While the intent of the AFM images was not to obtain a precise quantitative measurement of the differences between suspensions, they do verify the substantial qualitative differences in the physical characteristics of the SLGO nanosheets and MLGO particles. For example, our suspension of SLGO nanosheets exhibited almost exclusively single- or few-layered characteristics, with heights around 1 to 2 nm. In contrast, MLGO suspensions mostly contained stacked particles ranging in height up to 10 nanometers.

### 2.4.2 Potentiometric Titrations of GO Particles

The concentration-normalized forward and reverse potentiometric titrations for two representative MLGO replicates are depicted in Figure 2.2. Forward and reverse titrations for each replicate generally overlap, which illustrates that proton sorption onto MLGO particles is rapid and reversible. The slopes and approximate inflection points of the titration curves for the replicates depicted in Figure 2.2 are similar, indicating good

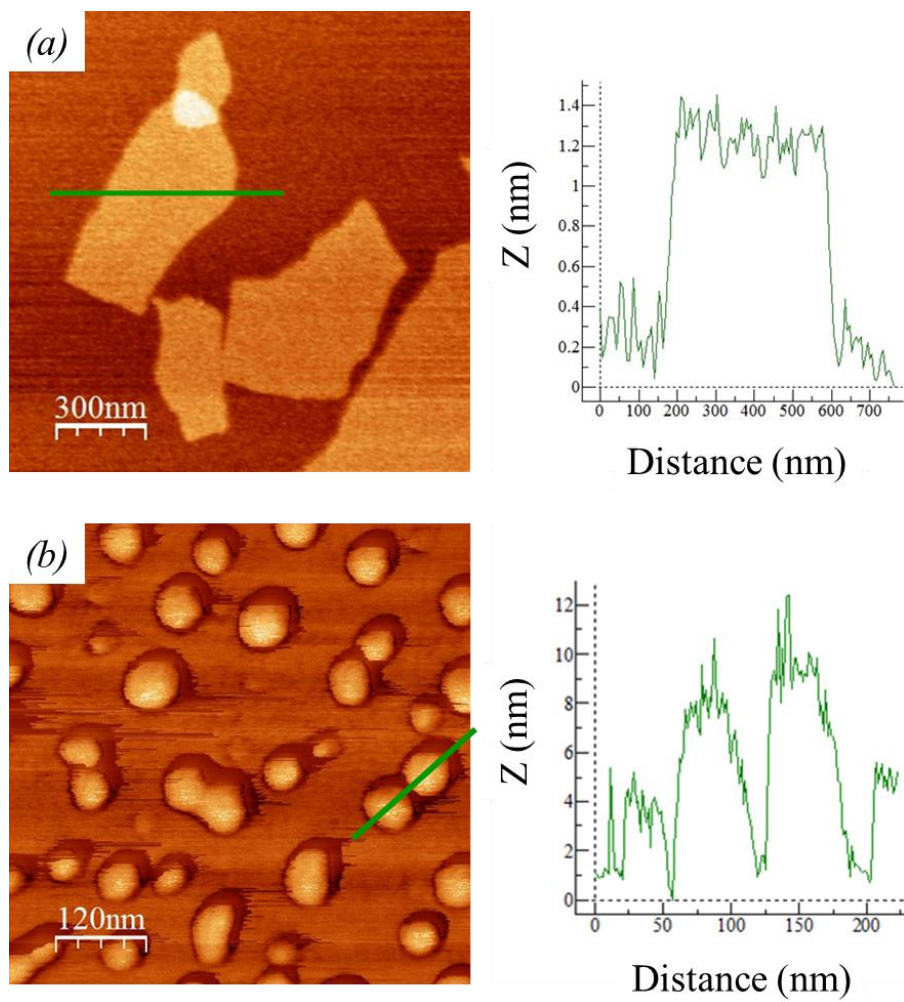


Figure 2.1: AFM images and height profiles for the cross-sections indicated in green for: (a) SLGO nanosheets; and (b) MLGO particles. Note that the peak heights change from  $\sim 1.3$  nm to  $\sim 10$  nm, respectively.

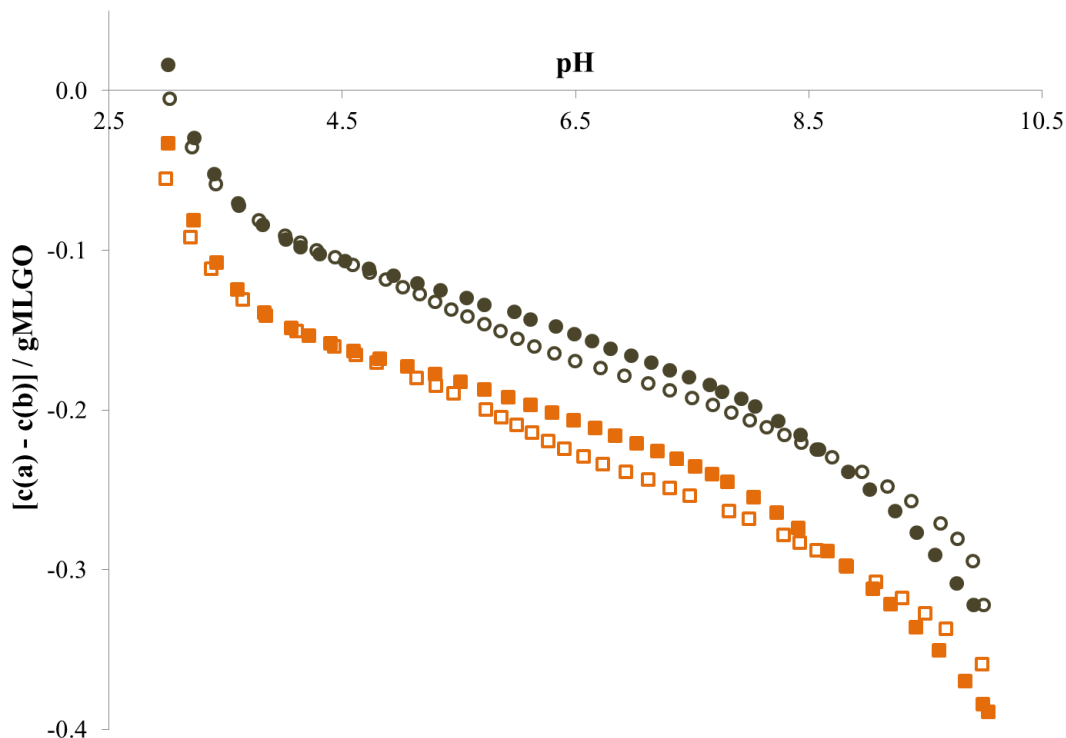


Figure 2.2: Representative concentration-normalized forward and reverse titration data for two replicate MLGO systems. Some data points have been removed for clarity. Experimental conditions: 100 mM ionic strength /  $\sim 1$  g MLGO L<sup>-1</sup>.

reproducibility. These replicate titration curves are vertically offset from each other, which suggests that each system contained a different concentration of acid (or, conversely, base) at the beginning of the titration, most likely due to variations in initial protonation states of the surface functional groups (i.e., the ratio between protonated and deprotonated surface sites). Still, we cannot discount the potential for trace quantities of residual H<sub>2</sub>SO<sub>4</sub> or HNO<sub>3</sub> contamination from the graphite oxidation steps of the nanosheet preparation procedure to influence the acid-base starting point for the titrations. However, the pK<sub>a</sub> values for each of these acids are below the titration range

modeled in this study. In addition, we use a mass balance approach for our potentiometric titration that is based on the excess/deficit of protons relative to an arbitrarily-designated zero-proton condition, rather than the tracking of absolute proton concentrations. These two factors combine to suggest that trace amounts of acid contamination would not influence the MLGO titration modeling results. Hence, we conclude that the vertical offsets between replicates from the same or different treatments do not indicate significant differences in overall protonation behaviors and instead we focus on comparing the overall nature of the curves.

Due to the complications described above, we cannot directly compare our MLGO potentiometric titration curves to provide insights regarding reproducibility of titration replicates and/or the influence of ionic strength on protonation behaviors. Consequently, we compared these treatments by normalizing each point of the forward titration curve to the average  $[c(a)-c(b) / g \text{ MLGO}]$  value throughout the entire pH range of each titration (Figure 2.3). This process preserves the shape of each titration curve but, by plotting them all on the same scale, allows all curves to be evaluated without regard to their respective initial protonation states (and resulting vertical offsets). Variability between replicates within a given ionic strength treatment is relatively low and approximately similar to the differences observed between ionic strength treatments. However, we do not discount the possibility of a very small influence of ionic strength, which we evaluate in later sections of this dissertation using electrostatic surface complexation models.

The normalized titration curves presented in Figure 2.3 suggest that the electric double layer effects at the MLGO surface are relatively small. In contrast, Szabó et al.

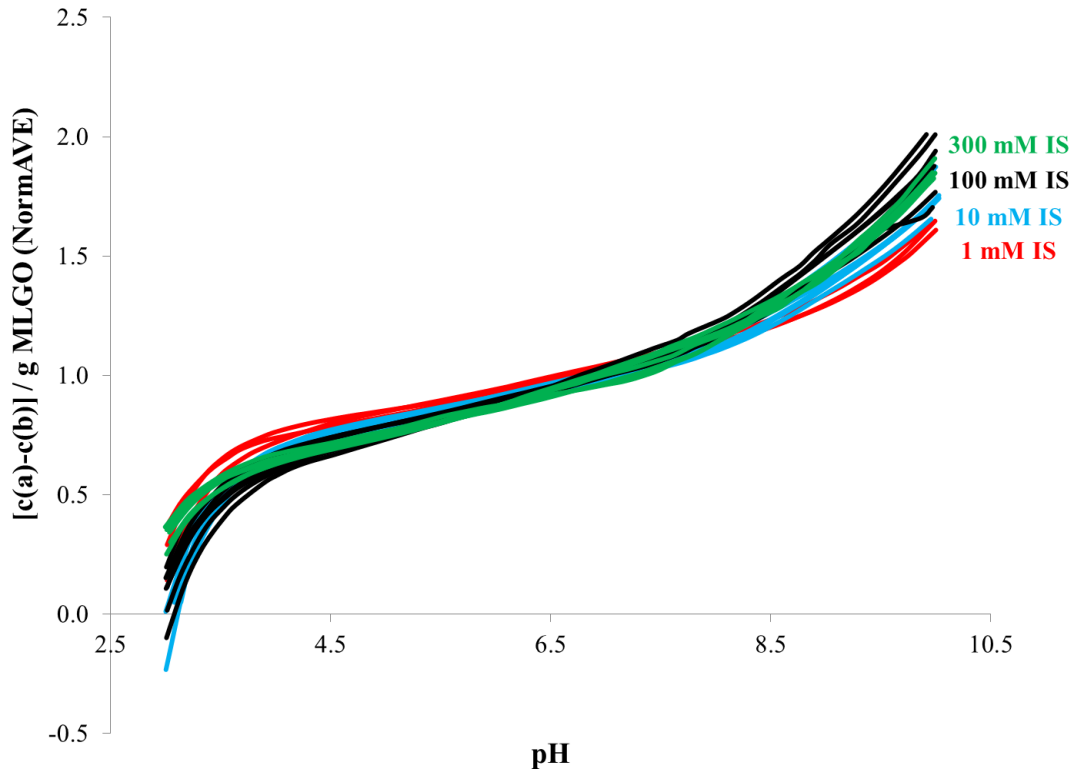


Figure 2.3: Potentiometric titration curves for MLGO particles from all ionic strength treatments normalized to their own average value. The normalization process allows for direct comparison of curves without regard to initial protonation state of the MLGO particles. Collectively, these curves illustrate the relatively small influence of ionic strength on MLGO protonation behaviors.

(2006b) observed an increase in the buffering capacity of graphite oxide when ionic strength increased from 5 mM to 500 mM (using NaCl as the background electrolyte). However, Szabó et al. only presented one titration for each ionic strength considered, and did not provide information regarding the variability of replicates within a given ionic strength treatment or the magnitude of these values in relation to the measured differences in the buffering capacity. Other studies have provided potentiometric titration results for varying forms of GO at one ionic strength (Sun et al., 2012; Zhao et al., 2012).

To our knowledge, our study is one of the first to report variability in the buffering capacity of GO materials for multiple replicates at different ionic strength values.

Interlayer spaces between laminations in an MLGO particle presumably contain functional groups situated on the basal planes. In order to determine whether protons can sorb to these sites, we conducted potentiometric titrations using SLGO nanosheets and compared these results to those from the MLGO-bearing systems. Assuming that MLGO particles contain 10 individual layers of SLGO nanosheets (Figure 2.1) and that the proton-active sites on the GO surfaces are evenly distributed (i.e., not concentrated at the edges), we would anticipate an order-of-magnitude decrease in the sorption of protons (or, as we discuss in later sections, metals) if they could not access interlayer sorption sites. We note that this calculation does not consider the negligible abundance of edge sites for those GO nanosheets existing within the laminated stacked structure. We applied a basic 4-site non-electrostatic surface complexation model to the titration results from a single ionic strength (100 mM) for SLGO- and MLGO-bearing suspensions to provide an estimate of the total numbers of sites available for proton sorption in each system. The details of this surface complexation modeling approach will be provided in later sections. We calculated an average (from three replicates) total site concentration ( $\pm 1\sigma$ ) of  $3.0 (\pm 0.2) \times 10^{-3} \text{ mol g}^{-1}$  for SLGO nanosheets in 100 mM ionic strength buffer. Using an identical modeling approach yielded a total average site concentration of  $2.9 (\pm 0.4) \times 10^{-3} \text{ mol g}^{-1}$  for MLGO particles suspended in 100 mM ionic strength buffer (Table 2.2). These values are between the previously-reported total site concentrations calculated for few-layered GO of  $2.4 \times 10^{-3}$  and  $3.6 \times 10^{-3} \text{ mol g}^{-1}$  determined via diffuse-layer surface complexation modeling by Zhao et al. (2011a, 2011b; 2012). The similarity

TABLE 2.2  
SITE CONCENTRATIONS AND V(Y) VALUES FOR EVERY 4-SITE NEM TESTED  
IN THIS STUDY

4-Site NEM							
Ionic Strength		Site 1	Site 2	Site 3	Site 4	Total	V(Y)
		[Site <sub>1</sub> ] (mol/g)	[Site <sub>2</sub> ] (mol/g)	[Site <sub>3</sub> ] (mol/g)	[Site <sub>4</sub> ] (mol/g)	[Site <sub>T</sub> ] (mol/g)	
<b>1 mM</b>	AVE	3.3E-04	4.2E-04	4.7E-04	1.4E-03	2.6E-03	0.21
	SD	1.0E-04	2.2E-05	6.8E-05	2.4E-04	3.1E-04	
<b>10 mM</b>	AVE	7.1E-04	3.8E-04	7.0E-04	1.0E-03	2.8E-03	0.40
	SD	3.5E-04	4.0E-05	5.3E-05	7.8E-05	4.3E-04	
<b>100 mM</b>	AVE	3.9E-04	4.6E-04	7.6E-04	1.2E-03	2.9E-03	0.84
	SD	7.4E-05	7.2E-05	2.4E-04	1.4E-04	4.0E-04	
<b>300 mM</b>	AVE	4.0E-04	4.0E-04	7.2E-04	1.4E-03	3.0E-03	0.47
	SD	4.5E-05	8.7E-05	1.8E-04	1.6E-04	2.5E-04	
<b>Combined</b>	AVE	<b>4.6E-04</b>	<b>4.2E-04</b>	<b>6.6E-04</b>	<b>1.3E-03</b>	<b>2.8E-03</b>	<b>0.48</b>
	SD	1.7E-04	3.7E-05	1.3E-04	1.9E-04	1.5E-04	

in the titration results for SLGO nanosheets and MLGO particles suggests that protons can access the interlayer sorption sites between laminations in MLGO-bearing systems.

#### 2.4.3 Batch Metal Sorption onto GO Particles

Figure 2.4 and Figure 2.5 illustrate the sorption of Cd and Pb, respectively, onto GO nanosheets across a range of pH and ionic strength conditions. For both Cd and Pb, the sorption edges for each ionic strength treatment contain two replicates, which largely

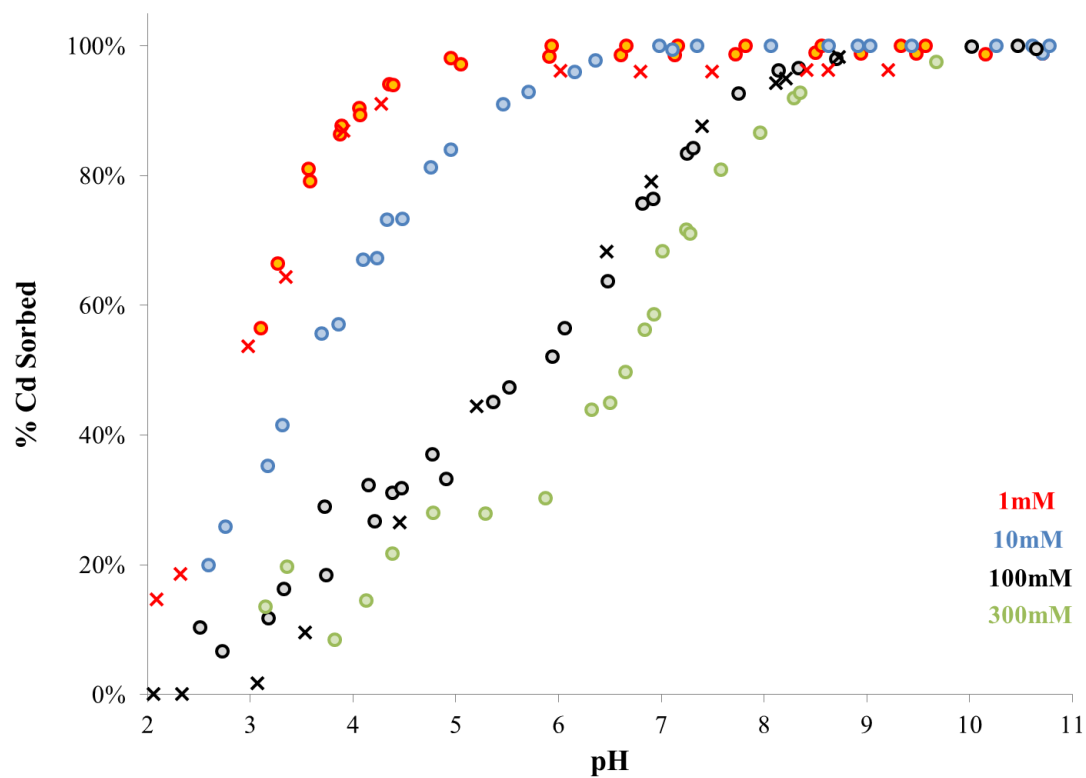


Figure 2.4: Sorption of Cd ( $8.9 \times 10^{-6}$  M) by GO ( $200 \text{ mg L}^{-1}$ ) as a function of both pH and ionic strength. Red, blue, black, and green circles indicate the sorption of Cd to MLGO particles in 1 mM, 10 mM, 100 mM, and 300 mM ionic strength treatments, respectively. Red and black  $\times$ 's indicate the sorption of Cd to SLGO nanosheets in 1 mM and 100 mM ionic strength treatments, respectively.

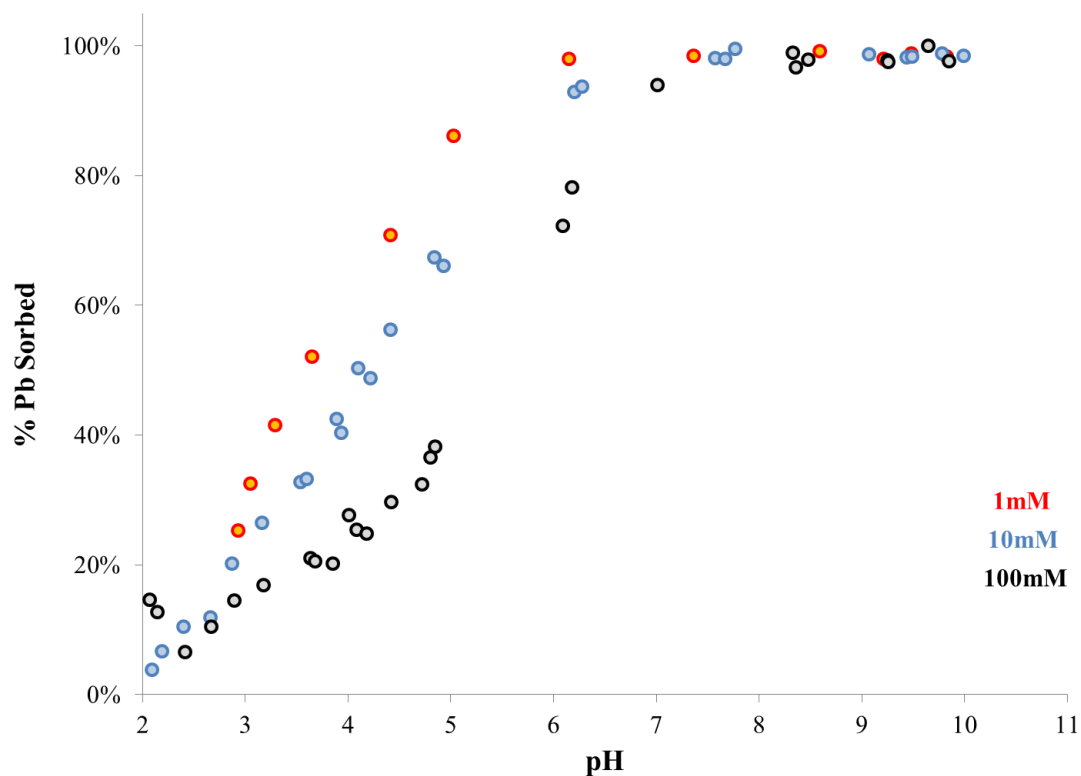


Figure 2.5: Sorption of Pb ( $4.8 \times 10^{-6}$  M) by MLGO particles ( $20 \text{ mg L}^{-1}$ ) as a function of both pH and ionic strength. Red, blue, and black circles indicate the sorption of Pb to MLGO particles in 1 mM, 10 mM, and 100 mM ionic strength treatments, respectively.

overlapped and are therefore not distinguished in these figures. In the 1 mM and 100 mM ionic strength treatments, the extents of Cd sorption onto SLGO nanosheets is within the experimental uncertainty of the extents of Cd sorbed onto the same mass of MLGO particles suspended (Figure 2.4). Hence, we conclude that metals with an atomic radius smaller than or equal to that of Cd can access interlayer sorption sites between laminations in MLGO-bearing systems. These findings are consistent with studies that indicate ammonium ions can sorb to the interlayer surfaces of graphite oxide (Liu et al., 2002; Seredych and Bandosz, 2007). However, it is also possible to account for our data

if all of the metal-binding sites are located at the edges of the GO material, so that SLGO and MLGO each exhibit the same concentration of binding sites per mass of material.

In each system, GO particles exhibit a significant capacity to sorb Cd and Pb across a wide range of pH values. However, in marked contrast to the potentiometric titrations, batch metal sorption experiments for both Cd and Pb illustrate that ionic strength dramatically influences the sorption of these metals onto GO particles. For example, the point at which 50% of the initial Cd concentration is sorbed by MLGO particles shifts from pH ~3 to pH ~6.7 in the 1 mM and 300 mM ionic strength systems, respectively. Similarly, 50% of the initial Pb concentration is sorbed to MLGO particles at pH ~3.5 in the 1 mM ionic strength systems and at pH ~5.3 in the 100 mM ionic strength systems.

#### 2.4.4 Electrostatic Surface Complexation Modeling of Proton and Metal Sorption

Collectively, the potentiometric titrations and batch metal sorption experiments illustrate a dramatic and unexpected difference in sorption behaviors for protons and metals at the MLGO particle surface. While the titration data indicate very little influence on MLGO buffering with increases in ionic strength, the batch metal sorption data suggest that ionic strength substantially impacts the interactions between Cd or Pb and the MLGO surface. Hence, we evaluated several different surface complexation modeling approaches, including a non-electrostatic model (NEM), a constant capacitance model (CCM), and a diffuse layer model (DLM), for their abilities to account for the variation in proton and metal sorption behaviors as a function of ionic strength. The two electrostatic models of sorption used in this study, namely the CCM and DLM, have been successfully employed to describe changes in proton and metal sorption at environmental

surfaces in response to changes in ionic strength [see reviews by Goldberg (1992) and Koretsky (2000)].

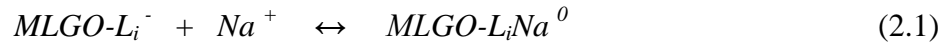
A successful model would yield calculated equilibrium constants ( $pK_a$  and  $K_{ads}$ ) from the experimental data that do not vary as a function of ionic strength. Consistency in these equilibrium constants as a function of ionic strength, calculated from a specific sorption model, would indicate that the model alone adequately accounts for the electrostatic effects occurring at the GO surface and that these singular values for  $pK_a$  or  $K_{ads}$  could be utilized to model the sorption of protons and metals, respectively, throughout a range of environmental conditions. However, we determined that the DLM yields a strong positive trend in the  $pK_a$  values as a function of ionic strength. Conversely, the CCM yields a strong negative trend in the  $K_{ads}$  for both the Cd and Pb sorption data as a function of ionic strength. Hence, neither of these electrostatic surface complexation models could account for the influence of ionic strength on the sorption behaviors of protons and metals across the range of conditions evaluated. A complete description of the modeling approaches and results is available in Appendix A.

#### 2.4.5 Modeling the Competitive Interactions between Protons, Cd or Pb, and Na

Both the CCM and DLM implicitly assume the absence of complexation reactions between the surface being modeled and the background electrolyte (Goldberg, 1995). However, Alessi et al. (2010) illustrated that ionic strength effects on divalent cation sorption can be considered as a competition between divalent cation sorption and the sorption of monovalent cations present in the background electrolyte. We test whether the observed ionic strength effects for Cd and Pb sorption can be modeled by invoking a similar approach, and we explicitly account for the competitive interaction with Na at

available binding sites on the MLGO surface. However, we assume that the Na-MLGO interaction is an intrinsic property that can occur in the presence or absence of metals, and as such, we must also consider the effect of Na competition on MLGO protonation reactions, even though we did not see a strong ionic strength effect in our potentiometric titration data. By assuming the same affinities for Na-MLGO interaction in the modeling of both the titration and metal sorption data, we can calculate a suite of equilibrium constants that account for the observed sorption behaviors under all of the conditions studied here.

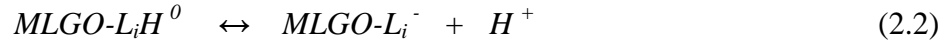
We explicitly account for these competitive interactions in the modeling of the potentiometric titrations and the batch metal sorption extents by incorporating into a 4-site NEM the following interactions between each MLGO surface site and Na:



where  $L_i$  is assumed to be a discrete surface functional group type responsible for cation sorption and  $MLGO-$  represents the remainder of the MLGO particle to which the functional group is attached. Because the potentiometric titration data do not exhibit a significant or consistent trend with respect to ionic strength, we cannot use these data to constrain values for the  $\text{Log } K_{ads}$  for Reaction 2.1 (herein denoted as  $\text{Log } K_{Na-ads}$ ) at each surface site. Rather, our approach is to assume a value for  $\text{Log } K_{Na-ads}$  for each site and to find the value that yields the best fit to both the potentiometric titration data and the Cd and Pb sorption data. We begin by testing  $\text{Log } K_{Na-ads}$  values between 0.5 and 2.0 at 0.5-step intervals. By setting the  $\text{Log } K_{Na-ads}$  for each site at the same value, we are applying

the interaction of the background electrolyte uniformly amongst all sites, rather than allowing a different degree of influence at each specific site type. We propose that this approach is more consistent with the way traditional electrostatic models integrate the influence of ionic strength. To provide a baseline result, we also model our potentiometric titration and metal sorption data without incorporating Reaction 2.1.

For each potentiometric titration replicate from the four different ionic strength treatments, we first attempted to fit the data between pH 3.0 and pH 10.0 (or pH 3.2 and pH 10.0 for the two lowest ionic strengths) using a 4-site NEM (for discussion of the selection of this model, see Appendix A). The chemical equilibrium modeling associated with this approach was conducted using FITEQL 2.0 (Westall, 1982). We represent the deprotonation of surface sites as follows:



We assume that MLGO surface sites are not capable of being doubly-protonated. Prior to a given titration, we do not know the degree to which the MLGO particles are protonated, nor do we have an initial estimate of the total concentration of H in these systems.

Hence, the modeling of potentiometric titrations compares the excess/deficit protons in a system to an arbitrarily-assigned zero proton condition (Westall and Jones, 1995; Fein et al., 2005). As indicated in Reaction 2.2, we designate the fully protonated MLGO surface as the zero proton condition.

FITEQL uses the measured extents of proton sorption at each measured pH and the known equilibrium constants for aqueous complexation reactions occurring in each system (Table B.1) to constrain acidity constants ( $K_a$ ) for Reaction 2.2 as follows:

$$K_{a(i)} = \frac{[GO-L_i^-] * a_{H^+}}{[GO-L_iH^0]} \quad (2.3)$$

where brackets represent the molal concentration of surface species and  $a_x$  represents the activity of the species in the associated subscript. Activity coefficients for aqueous ions are calculated using the Davies equation. Given the similarity between forward and reverse titrations, we only fit forward titrations curves from individual replicates. We note that from this point forward, sites are designated by number in order of increasing  $pK_a$  value.

We evaluate model fits both visually and through the FITEQL variance or goodness-of-fit parameter,  $V(Y)$ , defined as:

$$V(Y) = \frac{\sum \left( \frac{Y_{calc} - Y_{exp}}{S_{exp}} \right)^2}{n_p n_{II} - n_u} \quad (2.4)$$

where  $S_{exp}$  is the error associated with the model output,  $n_p$  is the number of modeled data points,  $n_{II}$  is the total number of components for which both free and total concentrations are known, and  $n_u$  is the total number of adjustable parameters in a system. The value of  $V(Y)$  depends not only on the residuals calculated from experimental ( $Y_{exp}$ ) and model-calculated ( $Y_{calc}$ ) values, but also the distribution of this error. Hence, the optimum  $V(Y)$

value is 1 (i.e., the variance is normally distributed), although experimental evidence suggests that values between 0.1 and 20 are common for reasonably good model fits (Westall, 1982).

For each assumed value of  $\text{Log } K_{\text{Na-ads}}$ , we calculated the  $\text{pK}_a$  values of Site 1 through Site 4 for each ionic strength treatment. The complete potentiometric titration modeling results are provided in Figure B.1, with a representative subset for Site 2 provided in Figure 2.6. These two figures illustrate several important trends. First, the  $\text{pK}_a$  values averaged across ionic strength for a given surface site significantly increase with increasing values of  $\text{Log } K_{\text{Na-ads}}$ . The  $\text{pK}_a$  values for each surface site averaged across ionic strength are depicted by the horizontal lines in Figure B.1 and Figure 2.6. These values are again depicted in Figure 2.7 and shown as a function of  $\text{Log } K_{\text{Na-ads}}$ . Average  $\text{pK}_a$  values for Site 1 through Site 4 each increase by 0.65 log units as we change the assumed extent of Na binding affinity for each site from no Na binding to values for the  $\text{Log } K_{\text{Na-ads}}$  of 2.0. For any given titration to attain the same buffering capacity despite the competition with Na at surface sites, the affinity for protons at the MLGO surface must increase.

In addition, from these figures, we observe that as  $\text{Log } K_{\text{Na-ads}}$  increases, the calculated site-specific  $\text{pK}_a$  values exhibit a larger variation as a function of ionic strength. For example, the ranges of  $\text{pK}_a$  values on Figure B.1 and Figure 2.6 increase with increasing  $\text{Log } K_{\text{Na-ads}}$  and begin to show a trend with respect to ionic strength. This trend also is present in Figure 2.7, as the error bars, which indicate the standard deviation of the four ionic strength-specific  $\text{pK}_a$  values for each surface site, become larger with increasing values of  $\text{Log } K_{\text{Na-ads}}$ .

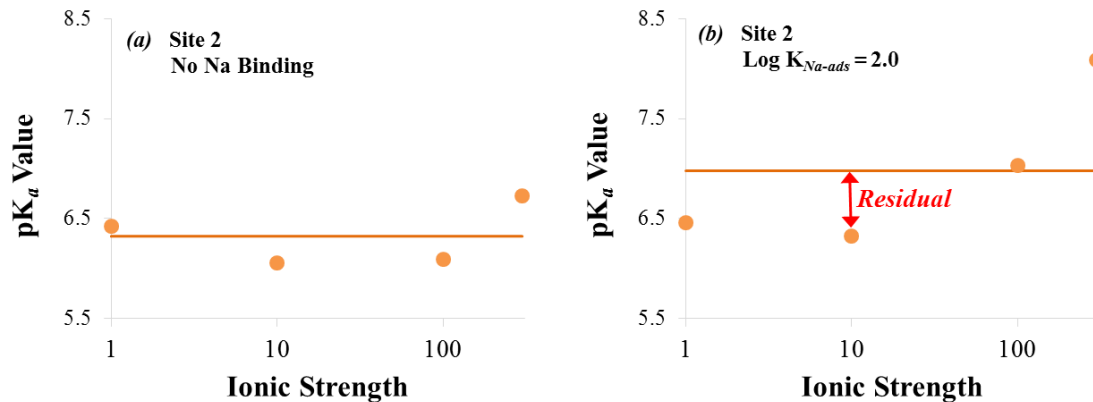


Figure 2.6: Calculated pK<sub>a</sub> values for Site 2 as a function of ionic strength assuming: (a) no Na competition at the surface site; or (b) a Log K<sub>Na-ads</sub> = 2.0. The horizontal line is the average of the four ionic strength-specific pK<sub>a</sub> values in each panel. Note that the range and average of the ionic strength-specific pK<sub>a</sub> values increases incorporating Na competition into the modeling of the titrations. Similar plots for each site and Log K<sub>Na-ads</sub> value are provided in Figure B.1. In addition, the results of these two plots are referenced in Figure 2.7. Each point on these figures represents the average pK<sub>a</sub> value calculated from between three and seven potentiometric titration replicates for each ionic strength.

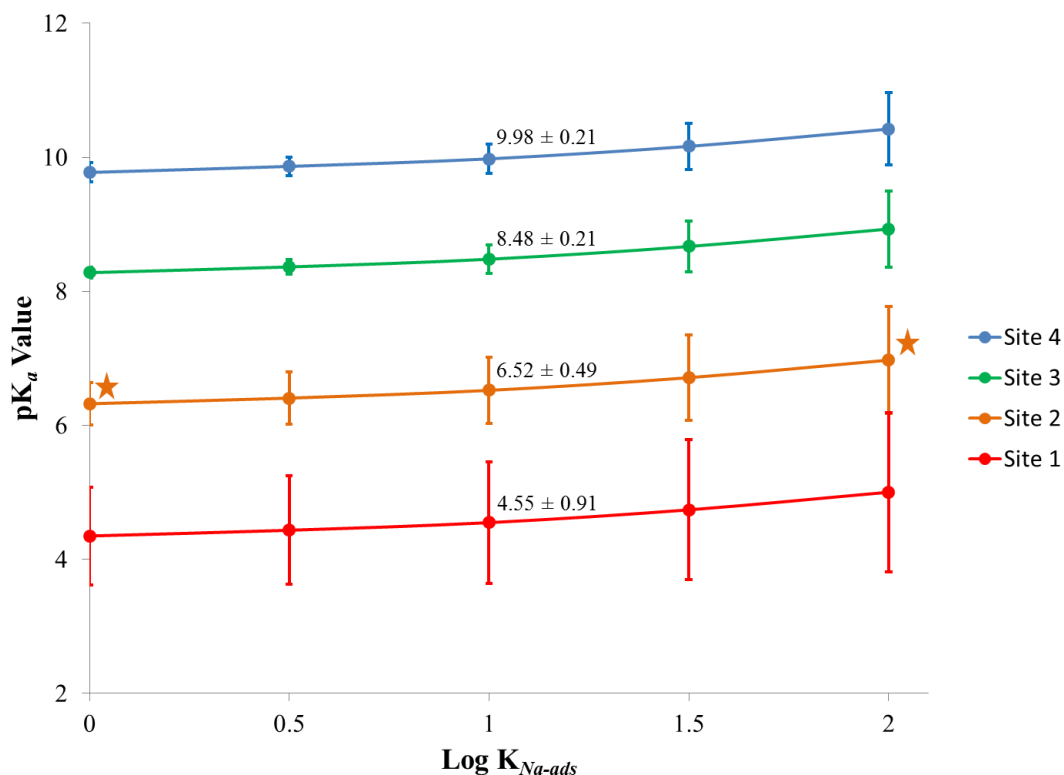


Figure 2.7:  $pK_a$  values averaged across all ionic strengths for each of the four surface sites as a function of  $\text{Log } K_{Na-ads}$ . Error bars indicate the standard deviation from the four ionic strength-specific  $pK_a$  value for each surface site and  $\text{Log } K_{Na-ads}$  combination. For example, the data used to calculate the two treatments marked with a star are shown in more detail in Figure 2.6. Note that the magnitude of the standard deviations increases with increasing  $\text{Log } K_{Na-ads}$  values, indicating that larger  $\text{Log } K_{Na-ads}$  values result in a greater range of  $pK_a$  values with respect to ionic strength. Numerical average  $pK_a$  values ( $\pm 1\sigma$ ) are shown for the selected model, which is fully described in Section 2.4.6.  $pK_a$  values plotted at  $\text{Log } K_{Na-ads} = 0$  are those calculated from models that do not include a binding affinity for Na at each site.

As previously discussed, one characteristic of a successful model is its ability to yield calculated site-specific  $pK_a$  values that do not show a trend with respect to ionic strength. The data presented above clearly indicate that as the assumed  $\text{Log } K_{Na-ads}$  value incorporated into our potentiometric titration modeling increases, our ability to achieve a suitable model becomes increasingly compromised. In order to quantify the effect of the  $\text{Log } K_{Na-ads}$  values on the trend in  $pK_a$  values with respect to ionic strength, we sum the differences between the site-specific  $pK_a$  values calculated for each ionic strength and the average  $pK_a$  value across all ionic strengths for each site. In other words, working from Figure B.1, we calculate a residual between the points provided in each panel and the horizontal line (i.e., the average  $pK_a$  across ionic strength) for each respective panel, and sum the square of these residuals (SSR) across all sites for a given  $\text{Log } K_{Na-ads}$  model. An example residual is illustrated in the top-right panel of Figure B.1 and also on Figure 2.6b. The SSR values for each  $\text{Log } K_{Na-ads}$  used in our modeling of the potentiometric titrations are provided on Figure B.1 and visually illustrated on Figure 2.8. These calculations indicate that the models with the smallest  $\text{Log } K_{Na-ads}$  values yield the least variation across the ionic strengths studied. However, for  $\text{Log } K_{Na-ads}$  up to 1.0, much of the variation in  $pK_a$  values that contributes to the increasing SSR is concentrated in the residuals for Site 1 and Site 2 (Figure B.1), and we discern only a moderate degree of overall trend in these  $pK_a$  values with respect to ionic strength.

In addition to  $pK_a$  values, the potentiometric titration modeling provides calculated sites concentrations and  $V(Y)$  values, which are provided in Table 2.2. Neither of these model parameters change in response to incorporation of the Na competition reaction (Reaction 2.1). Hence, the value of  $\text{Log } K_{Na-ads}$  does not affect the ability of the

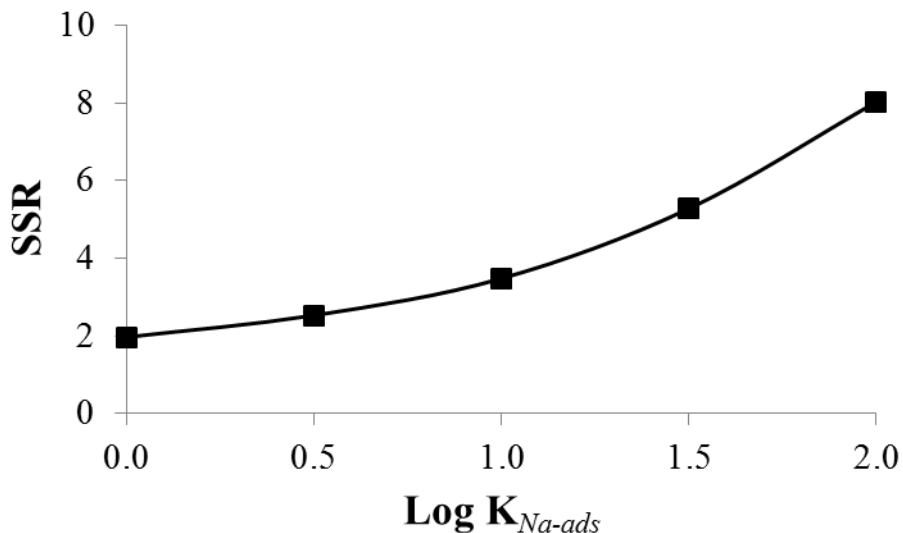


Figure 2.8: Sum of the squared residuals (SSR) between the site-specific  $pK_a$  values calculated for each ionic strength and the average  $pK_a$  value across all ionic strengths for each site. These values are plotted as a function of  $\text{Log } K_{Na-ads}$ . See Figure B.1 for the complete data set from which these values are calculated.

each model to fit an individual titration replicate, but to do so, the  $pK_a$  value has to increase as  $\text{Log } K_{Na-ads}$  increases.

Testing the same range of  $\text{Log } K_{Na-ads}$  values that were tested in the potentiometric titration modeling, we modeled the Cd and Pb sorption reactions using a 1:1 metal:site stoichiometry, expressing the formation of the generic metal-MLGO surface complex as:



where  $M^{2+}$  represents the divalent aqueous cation of interest. In contrast to the H concentrations during potentiometric titration modeling, the total concentration of the

metal in each system is known for the batch metal sorption modeling. We observed extensive sorption of each metal below pH 5, where we presume that only Site 1 is deprotonated, and consequently, each surface complexation model that we tested involved sorption onto the deprotonated form of Site 1. This was our only modeling restriction and we tested all possible combinations of sites as long as Site 1 was included. In our modeling of the Cd systems, we allowed only the Cd<sup>2+</sup> ion to sorb to the MLGO surface, as MLGO-free Cd speciation modeling indicated that CdOH<sup>+</sup> was only a minor (<15%) component of these systems below pH 9.5 (Figure B.2). However, due to the substantial presence of PbOH<sup>+</sup> above pH ~7.0 (Figure B.3), we evaluated the potential interactions between PbOH<sup>+</sup> and the MLGO surface at Sites 2 through 4.

FITEQL uses the measured extents of metal sorption to constrain stability constants ( $K_{ads}$ ) for the metal-MLGO surface interaction as:

$$K_{ads(i)} = \frac{[GO-L_iM^+]}{[GO-L_i^-] * a_{M^{2+}}} \quad (2.6)$$

We obtained the concentrations of each surface site for the  $K_{ads}$  calculation from modeling of the potentiometric titration data (Table 2.2). We also incorporated into the metal sorption models a protonation/deprotonation reaction for each site, with pK<sub>a</sub> values derived from the potentiometric titration model that used the same Log K<sub>Na-ads</sub> value that was being tested in each metal sorption model (Figure 2.7), again testing Log K<sub>Na-ads</sub> values between 0.5 and 2.0.

Surface site combinations that converged on stability constant values for either Cd- or Pb-MLGO surface complexation reactions are provided in Table B.2 and Table

B.3, respectively. For each site combination evaluated, increasing values of  $\text{Log } K_{Na-ads}$  caused an increase in the calculated stability constant for the Cd- or Pb-MLGO surface complexes, as a greater affinity between the metal and site is needed to counter the competition from Na-MLGO interactions. For each value of  $\text{Log } K_{Na-ads}$  that we tested, we calculated average stability constants across the ionic strengths considered for the Cd- or Pb-MLGO sorption reactions in each model. These average stability constants were then used to predict the metal sorption behaviors we observed for each ionic strength. We then calculated the residuals between these model predictions and the actual data, and summed the square of the residual (SSR) for each experimental point across all ionic strengths to yield an overall measure of the goodness-of-fit for a specific model to our metal sorption data across a range of pH and ionic strength conditions using a singular value for  $K_{ads}$ . We note that the calculation of the SSR for the metal sorption modeling is very different than the SSR calculation for the potentiometric titration modeling, as here the SSR measures the goodness-of-fit between the model and the actual data for each ionic strength, rather than measuring the variation in the equilibrium constant value with respect to ionic strength. In general, within a given site combination, the models with the largest  $\text{Log } K_{Na-ads}$  values best predicted the observed metal sorption behaviors across all ionic strengths (Table B.2; Table B.3).

#### 2.4.6 A Proposed Model for Proton and Metal Sorption to MLGO Particles

Our goal with this modeling effort was to converge on a set of equilibrium constant values that describe the interactions between MLGO surfaces and protons ( $K_a$ ), target metals ( $K_{ads}$ ) and Na ( $K_{Na-ads}$ ). We defined a successful model as one that would yield calculated equilibrium constants ( $\text{p}K_a$  and  $K_{ads}$ ) from the experimental data that do

not vary as a function of ionic strength and are simultaneously capable of predicting measured metal sorption behaviors across a range of pH and ionic strength conditions. However, our data define two conflicting trends. Models with the smallest Log  $K_{Na-ads}$  values yielded the least variation in calculated  $pK_a$  values across ionic strength at each site, but also yielded the poorest fits to the metal sorption data. Conversely, models with the highest Log  $K_{Na-ads}$  values yielded the most variation in calculated  $pK_a$  values across ionic strength at each site, but yielded the best fits to the metal sorption data.

Here we attempt to balance these two effects and select a model that exhibits a reasonable adherence to the criteria presented above. Because the SSR values from the titration and metal sorption modeling illustrate substantially different properties of the model outputs, we cannot simply combine these parameters to estimate an overall model fit. Instead, we use a two-step approach for selecting the model that best fits both the potentiometric titration data and the Cd and Pb sorption data. First we consider the potentiometric titration modeling, as this establishes the  $pK_a$  values that are used as a fundamental input for subsequent metal sorption models. Figure 2.8 indicates that SSR values for the titration modeling increase exponentially with increases in the value of Log  $K_{Na-ads}$ , which results in a marked change in the rate of increase for SSR values above Log  $K_{Na-ads} = 1.0$ . We previously observed that for Log  $K_{Na-ads}$  up to 1.0, we discern only a moderate degree of overall trend in the calculated  $pK_a$  values with respect to ionic strength, with much of the variation in  $pK_a$  values concentrated in Site 1 and Site 2 (Figure B.1). Knowing that we must maximize the value the Log  $K_{Na-ads}$  value to best fit the metal sorption data, we believe that a maximum value of Log  $K_{Na-ads}$  of 1.0 still provides reasonable adherence to the titration modeling criteria.

Selection of this model results in calculated  $pK_a$  values ( $\pm 1\sigma$ ) for Site 1 through Site 4 of 4.55 ( $\pm 0.91$ ), 6.52 ( $\pm 0.49$ ), 8.48 ( $\pm 0.21$ ), and 9.98 ( $\pm 0.21$ ), respectively (Figure 2.7). In order to assign an identity to each of the MLGO surface sites, spectroscopic studies are required. At the time of this writing, we have prepared and analyzed samples using X-ray absorption spectroscopy (XAS) at the Advanced Photon Source at Argonne National Laboratory (USA), and are anticipating the results of these studies. However, by comparing the  $pK_a$  values determined via titration to typical protonation constants for functional group types, we infer that the sites with  $pK_a$  values of between 4.0 and 6.0 are likely associated with short-chained carboxylic acids covalently-bonded to the hexagonal carbon lattice, while  $pK_a$  values of between 9.0 and 11.0 are likely hydroxyl/phenolic acids. Using this assumption, we postulate that our most abundant functional group (Site 4) is likely a hydroxyl group, which is consistent with GO structural models that indicate a dominant hydroxyl presence at the GO surface (Lerf et al., 1998; Szabó et al., 2006a; Gao et al., 2009). In addition, Konkana and Vasudevan (2012) combined titration experiments and infrared spectroscopy of GO samples to identify surface-associated functional groups, with  $pK_a$  values of 4.3 and 6.6 for carboxyl groups and 9.8 for the phenolic group. The exact value of the deprotonation constant for a given functional group is strongly influenced by the relative placement of proton-active sites on the nanosheet surface.

The total site concentrations for the selected model are presented in Table 2.2. We note that the total site concentrations were identical for all tested models, regardless of the  $\text{Log } K_{Na-ads}$  value. Upon averaging the total site concentrations across all of the ionic strength treatments, the average total proton-active site concentrations for MLGO

particles is calculated to be  $2.8 \times 10^{-3} \text{ mol g}^{-1}$ . This value is between the previously-reported total site concentrations calculated for few-layered GO of  $2.4 \times 10^{-3}$  and  $3.6 \times 10^{-3} \text{ mol g}^{-1}$  determined via diffuse-layer surface complexation modeling by Zhao et al. (2011a, 2011b, 2012). Assuming a total maximum surface area for GO of  $\sim 1800 \text{ m}^2 \text{ g}^{-1}$  [as calculated by Szabó et al. (2006b) based on the size and weight of the repeating unit cells], our MLGO particles exhibit a proton active site density of  $\sim 0.9 \text{ sites nm}^{-2}$ , which agrees well with other sites densities reported in the literature for graphite oxide [up to  $\sim 1$  to  $\sim 2 \text{ sites nm}^{-2}$ ; Cassagneau et al. (2000) and Szabó et al. (2006b)]. However, these site densities are significantly smaller than the  $18 \text{ sites nm}^{-2}$  calculated by Sun et al. (2012), who utilized a surface area measurement of  $127 \text{ m}^2 \text{ g}^{-1}$  determined from  $\text{N}_2$ -BET analyses in their calculations. BET measurements generally underestimate GO surface areas (Szabó et al., 2006b). The high reactivity of our MLGO surfaces is also demonstrated by comparing our calculated total site concentrations to those reported for 2- or 3-layered graphene ( $1.1 \times 10^{-3} \text{ mol g}^{-1}$ ; Zhao et al., 2011b) and oxidized multi-walled carbon nanotubes ( $4.2 \times 10^{-4} \text{ mol g}^{-1}$ ; Chen et al., 2008), which are 2.5 to 6.5 time lower on a per gram basis.

Next, because we previously defined a  $\text{Log } K_{\text{Na-ads}}$  value of 1.0 as the maximum value that can still adhere to the titration modeling criteria, and because we know we must maximize the value the  $\text{Log } K_{\text{Na-ads}}$  value to best fit the metal sorption data, we evaluate only the metal sorption models that incorporate a value of  $\text{Log } K_{\text{Na-ads}} = 1.0$ . Of these models, SSR values associated with the metal sorption data are minimized for the models that involve the binding of  $\text{Cd}^{2+}$  at Sites 1, 2, and 4 (Table B.2), and the binding of  $\text{Pb}^{2+}$  at Site 1 and  $\text{PbOH}^+$  at Site 2 (Table B.3). Table 2.3 provides calculated stability

TABLE 2.3

STABILITY CONSTANT VALUES FOR METAL-MLGO SURFACE SORPTION  
REACTIONS FOR THE SELECTED MODEL

Reaction	Log $K_{ads}$
<b><u>Pb: Site 1 &amp; Site 2OH*</u></b>	
$GO-L_1^- + Pb^{2+} \leftrightarrow GO-L_1-Pb^+$	6.01
$GO-L_2^- + PbOH^+ \leftrightarrow GO-L_2-PbOH$	8.42
<b><u>Cd: Site 1, Site 2, &amp; Site 4</u></b>	
$GO-L_1^- + Cd^{2+} \leftrightarrow GO-L_1-Cd^+$	5.03
$GO-L_2^- + Cd^{2+} \leftrightarrow GO-L_2-Cd^+$	4.44
$GO-L_4^- + Cd^{2+} \leftrightarrow GO-L_4-Cd^+$	6.81

\* *Site 2OH* refers to the site combination from Figure B.3 that includes  $PbOH^+$  binding to Site 2.  
NOTE: The selected model incorporates a  $\text{Log } K_{Na-ads} = 1.0$  for Na-MLGO interactions.

constants for these reactions. We note that the Cd models that involve sorption of  $Cd^{2+}$  to Sites 1, 2, and 3 did not converge, which may indicate that, relative to Site 3, the abundance or structural placement of Site 4 could contribute to its selective sorption of metals. In addition, the SSR value for the Pb model that involves  $Pb^{2+}$  sorbing to Site 1 and  $PbOH^+$  sorbing to Site 3 is nearly identical to the selected Pb model. In general, several models resulted in similar fits, which illustrates the need for complimentary spectroscopic studies.

Figure 2.9 and Figure 2.10 illustrate the predicted model fits applied to the actual metal sorption data for the selected models from Table 2.3. The proposed Pb model provides a reasonable fit to the experimental data through pH 8.0, with only small misfits for some pH values in each ionic strength treatment. Relative to the Pb model, the proposed Cd model exhibits a greater degree of misfit to the actual sorption data. In particular, the Cd model underestimates the extents of sorption in the 1 mM and 10 mM ionic strength treatments, while overestimating sorption extents between pH ~4 and pH ~7 in the 100 mM and 300 mM ionic strength treatments. However, after testing multiple models, we determined that the selected models best distribute the misfits between the potentiometric titration data and the various metal and ionic strength treatments.

## 2.5 Conclusions

The behavior of MLGO that we document here represents a challenge for sorption modeling. Titration data exhibit no significant consistent trend as a function of ionic strength, suggesting that electric field effects on the protonation behavior are minimal. Conversely, we observed a large effect of ionic strength on the extent of Cd and Pb sorption across a range of pH conditions, which suggests that electrolyte interactions with the binding sites are not negligible. We derived a Na-binding model that yields a reasonable fit to both the titration and metal sorption data sets. Using a surface complexation modeling approach, we calculated MLGO site concentrations and  $pK_a$  values, as well as  $\text{Log } K_{ads}$  values for the important metal-GO surface complexes. This approach suggests that MLGO can be a highly efficient environmental sorbent, but that both protons and metals may compete with Na from the background electrolyte for

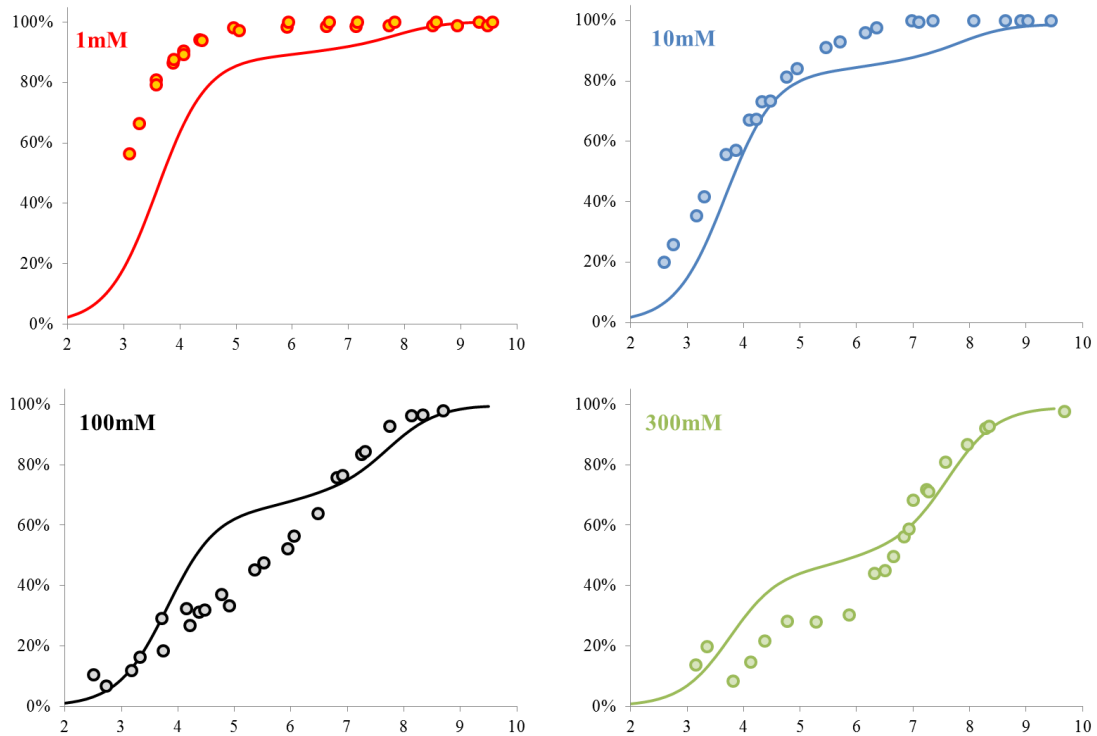


Figure 2.9: Predictions of  $\text{Cd}^{2+}$  sorption behaviors against pH for each ionic strength using the selected non-electrostatic model that incorporates a  $\text{Log } K_{\text{Na-ads}} = 1.0$  for Na-MLGO interactions and assumes the following site combination and equilibrium constants: Site 1 ( $\text{Log } K_{\text{ads}} = 5.03$ ;  $\text{p}K_a = 4.55$ ), Site 2 ( $\text{Log } K_{\text{ads}} = 4.44$ ;  $\text{p}K_a = 6.52$ ), and Site 4 ( $\text{Log } K_{\text{ads}} = 6.81$ ;  $\text{p}K_a = 9.98$ ). Prediction curves are shown in relation to actual measured Cd sorption extents for each ionic strength treatment. Axes are as follows: X (pH); Y (%Cd Sorbed).

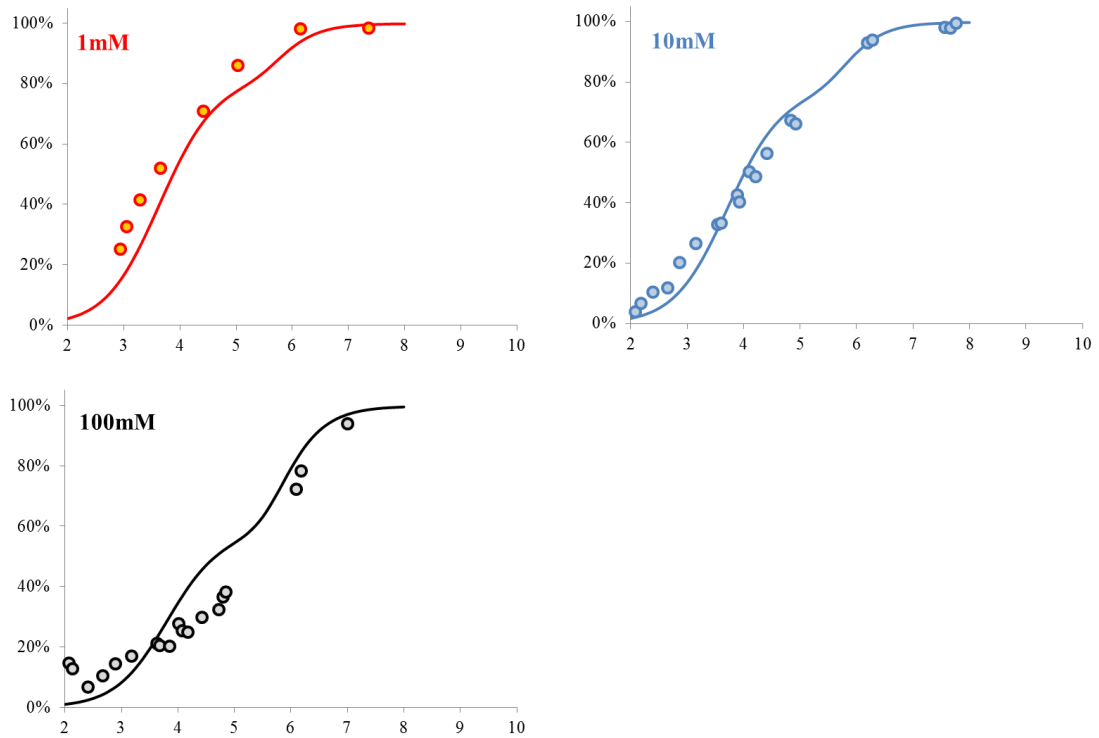


Figure 2.10: Predictions of Pb sorption behaviors against pH for each ionic strength using the selected non-electrostatic model that incorporates a  $\text{Log } K_{\text{Na-ads}} = 1.0$  for Na-MLGO interactions and assumes the following site combination and equilibrium constants: Site 1-Pb<sup>2+</sup> ( $\text{Log } K_{\text{ads}} = 6.01$ ;  $\text{p}K_a = 4.55$ ) and Site 2-PbOH<sup>+</sup> ( $\text{Log } K_{\text{ads}} = 8.42$ ;  $\text{p}K_a = 6.52$ ). Prediction curves are shown in relation to actual measured Pb sorption extents for each ionic strength treatment. See Table 2.3 for further details regarding reactions. Axes are as follows: X (pH); Y (%Pb Sorbed).

sorption sites. MLGO particles and SLGO nanosheets appear to exhibit strikingly similar proton buffering capacities and Cd sorption behavior, which suggests that the functional groups present within the interlayers of the MLGO particles are accessible to proton and metal sorption, or that proton- and metal-active functional groups are located predominantly on the edges of the material.

In addition, batch metal sorption experiments illustrate a significant capacity for MLGO particles to sorb metals over a wide range of pH conditions. For example, Log  $K_{ads}$  values describing the complexation between  $Pb^{2+}$  and  $Cd^{2+}$  and deprotonated Site 1 of MLGO, previously identified as a carboxyl group, are between two and three orders of magnitude larger than the corresponding stability constants for aqueous  $Pb^{2+}$ - and  $Cd^{2+}$ -acetate complexes (Shock and Koretsky, 1995). However, most stability constant values for important metal-GO surface complexes are generally comparable to those found in corresponding metal-bacteria and metal-mineral systems (Pagnanelli et al., 2006; Johnson et al., 2007; Ginn and Fein, 2008). Hence, the exceptional sorptive capacity of MLGO is most likely a function of its very high surface site concentration, relative to other environmental sorbents of similar size. In fact, the total MLGO site concentration of  $2.8 \times 10^{-3} \text{ mol g}^{-1}$  calculated in this study is approximately an order of magnitude higher than site densities found on bacterial cell walls or on quartz surfaces, and between 2.5 and 6 times higher than hematite, goethite, muscovite, and clinochlore surface site densities (Fein et al., 2005; Pagnanelli et al., 2006).

The data presented herein suggest that MLGO could dominate metal budgets in natural and engineered geochemical systems, and may offer higher removal efficiencies in contaminated environments than sorption approaches using other materials. The

surface complexation modeling parameters that we determine in this study enable extrapolation of our experimental measurements to quantitatively estimate metal budgets in GO-bearing systems throughout a range of environmentally-relevant conditions. However, although we utilized mechanistic methods to describe the interactions between MLGO surfaces and the protons, Na, and target metals in our systems, spectroscopic study must be conducted to confirm our findings. MLGO, which settles from suspension much faster than SLGO, may represent a practical and efficient sorbent for water treatment and remediation purposes.

## 2.6 Acknowledgments

This research was supported, in part, by a fellowship to T.D. from the Arthur J. Schmitt Foundation. In addition, we performed most experiments and analyses using instrumentation at the Center for Environmental Science and Technology (University of Notre Dame). I also acknowledge a substantial technical contribution by Jennifer Szymanowski.

CHAPTER 3:  
SORPTION OF AQUEOUS URANYL COMPLEXES TO MULTI-LAYERED  
GRAPHENE OXIDE

### 3.1 Abstract

For environmental systems in equilibrium atmospheric CO<sub>2</sub> and with low aqueous Ca concentrations, the aqueous speciation of U(VI) is dominated by uranyl ions ( $UO_2^{2+}$ ) at low pH (< ~5.2) and by uranyl-hydroxides and uranyl-carbonates at progressively higher pH values. As a result of their varying charges and structures, the extent to which these aqueous complexes sorb to various natural and engineered surfaces can vary dramatically. The objective of this study was to evaluate the ability of multi-layered graphene oxide (MLGO) to sorb aqueous uranyl complexes across a range of pH (2 to 9.5) and ionic strength conditions (1 mM, 10 mM, and 100 mM, using NaClO<sub>4</sub> as the background electrolyte). MLGO exhibited a remarkable ability to sorb U. We observed increasing extents of sorption with increasing pH, but sorption extents were only marginally influenced by ionic strength. In fact, using 210 mg MLGO L<sup>-1</sup> and 3 ppm (1.3 × 10<sup>-5</sup> M) U, our study illustrated that over 50% of the initial U concentration was sorbed by pH ~3, and 100% was sorbed by pH ~5 for all ionic strength treatments. The U sorption extents remained high (>80%), even at pH values up to 9.5. Using a 4-site non-electrostatic surface complexation model, we document that our measured extents of U binding by MLGO requires the sorption of at least two aqueous U complexes [ $UO_2^{2+}$  & a

uranyl hydroxide or carbonate] and we calculate the stability constant for the uranyl-MLGO sorption reaction. This stability constant can be used to predict U sorption behaviors in systems with varying water chemistries.

### 3.2 Introduction

As a result of the development of nuclear technologies, significant legacy concentrations of radionuclides are present in soil and groundwater at a variety of locations throughout the United States. For example, elevated U concentrations have been reported near former nuclear weapons research and testing facilities (Beasley et al., 1998; Catalano et al., 2006; Stubbs et al., 2006) and at abandoned U mine tailings sites (Abdelouas et al., 1998; Hyun et al., 2009; Kipp et al., 2009). In aerobic environments, U is present as the oxidized form U(VI), which exhibits a complex speciation based on pH and the composition of the associated solution. At low pH ( $< 5$ ), U(VI) generally exists as the positively-charged uranyl ion ( $UO_2^{2+}$ ). As pH increases in environments containing low Ca concentrations, the aqueous speciation of U(VI) transitions to complexes that exhibit weak positive charges at circumneutral pH through strong negative charges at high pH. In general terms, these aqueous U(VI) complexes include uranyl-hydroxides and uranyl-carbonates, respectively. Given that many surfaces present in soil and groundwater matrices are negatively-charged,  $UO_2^{2+}$  can form strong complexes with stationary-phase environmental constituents (Turner et al., 1996; Sylwester et al., 2000; Chisholm-Brause et al., 2001), but uranyl complexes are often more poorly sorbed at higher pH (Waite et al., 1994; Murphy et al., 1999). Therefore, the mobility of U in contaminated environments is generally dependent on the tendency for

these aqueous U complexes to sorb to the stationary-phases of the nearby soil and groundwater systems.

A widespread approach for the remediation of U contaminated environments involves inducing complexation reactions between the various aqueous uranyl complexes and either natural or engineered materials, thereby removing U from the aqueous phase (Morrison and Spangler, 1992; Barton et al., 2004; Gavrilesco et al., 2009; Ren et al., 2009; Dickinson and Scott, 2010). In fact, Zhao et al. (2012) recently reported that few-layered graphene oxide (GO) nanosheets produced from the chemical oxidation and exfoliation of graphite exhibit a higher maximum sorption capacity for U(VI) ( $97.5 \text{ mg g}^{-1}$ ; pH=5.0; T=293K) than any other currently-evaluated material. Zhao et al. (2012) demonstrated that GO nanosheets can sorb high concentrations of U through pH ~9.5, but they used non-mechanistic Langmuir-Freundlich isotherms to model the U-GO interactions. Their semi-empirical approach provides limited insights on the possible identities of the aqueous uranyl complexes involved and cannot be used to calculate the *intrinsic* stability constants for the associated U-GO surface complexes.

The chemical structure of GO consists of a lattice of six-member carbon rings that are interrupted and/or decorated with covalently-bonded oxygen-containing functional groups. The exact chemical identity of these functional groups is a topic of ongoing research, but likely includes epoxide, ketone, and hydroxyl groups on the basal planes, and carboxylic, lactol, and phenolic groups at the nanosheet edges (Lerf et al., 1998; Szabó et al., 2006a; Gao et al., 2009; Lee et al., 2010). The extremely high surface area to mass ratio and the presence of a variety of proton-active functional groups on the GO

surface contribute to the significant capacity of GO to sorb U and many other environmental contaminants.

In this study, we test whether surface complexation modeling can be used to account for U(VI)-GO binding to provide molecular-scale insights regarding the affinity between GO surfaces and aqueous uranyl complexes. We conducted bulk U sorption experiments in three ionic strengths as a function of pH. Using the  $pK_a$  values and site concentrations determined for GO surfaces in Chapter 2, we use the results of the U sorption experiments to constrain the number of surface sites involved in U binding, their pH ranges of influence, and the thermodynamic stability constants ( $K_{ads}$ ) for the uranyl-GO surface complex. This study focuses only on multi-layered GO (MLGO) particles, as they are more easily sedimented than single- or few-layered GO nanosheets in an engineered remediation system, and therefore more practical to separate from aqueous solutions during treatment operations.

### 3.3 Experimental Procedures

#### 3.3.1 MLGO Preparation and Characterization

MLGO particles were synthesized from natural flake graphite (Alfa Aesar, 99.9995%) using the Hummer's method (Hummers and Offeman, 1958). Briefly, graphite was mixed with  $\text{NaNO}_3$ ,  $\text{H}_2\text{SO}_4$ , and  $\text{KMnO}_4$  in an ice bath. The mixture was then transferred to a water bath at 35 °C and stirred for 30 minutes. Next, ultrapure water ( $R > 18 \text{ M}\Omega \text{ cm}$ ,  $\text{TOC} < 2 \mu\text{gC L}^{-1}$ ) was added and the mixture was stirred for approximately 20 minutes. Residual permanganate was then consumed by the addition of

hydrogen peroxide. Finally, GO was collected by centrifugation, washed repeatedly with ultrapure water, and freeze-dried under vacuum for 5 to 7 days before use.

The resulting dried mass was dispersed in ultrapure water using end-over-end rotation over a period of approximately 3 hours. Once fully suspended, MLGO particles were concentrated by repeatedly sedimenting the suspension under centrifugation ( $4000 \times g$  for 5 minutes), decanting the supernatant, and resuspending the pellet in fresh ultrapure water. After substantial removal of the single- or few layered nanosheets that remained suspended during the centrifugation process, the sedimented material was resuspended a final time and these solutions were retained for potentiometric titration and batch U sorption experiments. Final MLGO concentrations for individual batches were determined as the difference between the wet and dry ( $105\text{ }^{\circ}\text{C}$  for  $>24$  hours) masses of a 20 mL aliquot of the each final suspension. From this procedure we determined that the stock concentrations averaged  $\sim 2\text{ g MLGO L}^{-1}$  suspension, with an inherent pH of between 2.8 and 3.2.

We characterized the physical properties of the MLGO particles used in subsequent sorption experiments with atomic force microscopy (AFM; XE-70, Park Systems, Santa Clara, CA). An aliquot of the MLGO stock suspension was diluted 1:4 with ethanol and deposited on freshly cleaved mica. The instrument was operated in non-contact mode and images were flattened using the WSxM software package from Nanotec Electronica S.L. (Madrid, Spain). The AFM analyses resulted in determination of z-dimension, or height, which we used to infer the extent of exfoliation present in the nanosheet suspension.

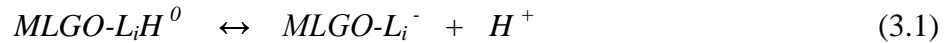
### 3.3.2 Batch U-MLGO Sorption Studies

Suspensions of MLGO particles were evaluated for their ability to sorb U from solution between approximately pH 2 and pH 9.5 in electrolyte buffers with initial ionic strengths (via addition of NaClO<sub>4</sub>) of 1 mM, 10 mM, and 100 mM. Starting with freshly-prepared parent solutions, we conducted two replicate batches for each ionic strength, with each batch consisting of multiple 5 mL samples with the same MLGO (210 mg L<sup>-1</sup>) and U (3 ppm; 1.26 × 10<sup>-5</sup> M) concentrations, adjusted to different pH values. Final U concentrations were achieved by adding appropriate quantities of a parent stock solution consisting of a pH-neutralized 4.20 × 10<sup>-3</sup> M (1000 ppm) standard [(UO<sub>2</sub>)(NO<sub>3</sub>)<sub>2</sub> in 5% HNO<sub>3</sub>]. Suspension pH was adjusted using 0.1 to 1.0 M HNO<sub>3</sub> or NaOH upon combination of MLGO and U stock solutions, which altered the ionic strength of the suspension (though addition of H<sup>+</sup> or Na<sup>+</sup> ions) by as much as 10 mM, particularly for the low pH systems.

Exposure of U to MLGO particles occurred for at least 4 hours, as kinetic studies associated with similar batch metal sorption studies indicated a sorption steady state occurs within this length of time. After the equilibration period, a final pH was measured, and the MLGO particles were removed from suspension by centrifugation (4000 × g for 5 minutes) followed by filtration (via 0.2 μm PTFE syringe filters) of the supernatant. The resulting solutions were acidified and analyzed via ICP-OES (Optima 2000DV, Perkin-Elmer, Waltham, MA) against aqueous U standards diluted into the same ionic strength matrix used during the sorption experiments.

### 3.3.3 Chemical Equilibrium Modeling

We utilized surface complexation modeling to describe the sorption of U to the functional groups present on the surface of MLGO particles. In our modeling, we assume complexation reactions between MLGO surface sites and both protons and aqueous uranyl complexes. We observed in Chapter 2 that the protonation behaviors of MLGO particles are only weakly influenced by ionic strength. We will provide evidence in this chapter that U-MLGO interactions are also not strongly affected by the ionic strength conditions of the suspending solution. Due to the lack of a significant electric field effect at the MLGO surface, we utilize the 4-site non-electrostatic model (NEM) presented in Chapter 2 (with no assumed Na binding). We represent the deprotonation of surface sites as follows:



where  $L_i$  is assumed to be a discrete surface functional group type responsible for proton sorption and  $MLGO-$  represents the remainder of the MLGO particle to which the functional group is attached. We assume that MLGO surface sites are not capable of being doubly-protonated. In Chapter 2, using Reaction 3.1 and the measured extents of proton sorption via potentiometric titration, we obtained site concentrations and acidity constant ( $pK_a$ ) values for each of the four MLGO surface sites (Table 3.1). The  $pK_a$  values calculated for Site 1 through Site 4 were 4.35, 6.32, 8.28, and 9.77, respectively. Herein, sites are designated by number in order of increasing  $pK_a$  value.

TABLE 3.1

MLGO SITE CONCENTRATIONS AND ACIDITY CONSTANTS FROM A 4-SITE  
NON-ELECTROSTATIC SURFACE COMPLEXATION MODEL

4-Site Non-Electrostatic Model								
Site 1		Site 2		Site 3		Site 4		Total
[Site <sub>1</sub> ] (mol/g)	pKa <sub>1</sub>	[Site <sub>2</sub> ] (mol/g)	pKa <sub>2</sub>	[Site <sub>3</sub> ] (mol/g)	pKa <sub>3</sub>	[Site <sub>4</sub> ] (mol/g)	pKa <sub>4</sub>	[Site <sub>T</sub> ] (mol/g)
4.6E-04	4.35	4.2E-04	6.32	6.6E-04	8.28	1.3E-03	9.77	2.8E-03

All chemical equilibrium modeling associated with the batch U sorption experiments was conducted using FITEQL 2.0 (Westall, 1982). Prior to modeling the U sorption data, we conducted MLGO-free speciation modeling for U that assumed identical pH, ionic strength, and background electrolyte conditions to those of the sorption experiments (the results are described in later sections). We assume that each of the aqueous species present in our systems could form a surface complex with the sites present at the MLGO surface, but that the most abundant species in a given pH range will dominate the complexation reactions. We assumed a 1:1 stoichiometry between the aqueous uranyl complex of interest and the sites at the MLGO surface. For example, at relatively low pH where the  $UO_2^{2+}$  ion dominates aqueous U speciation, we model the sorption of U by expressing the formation of the surface complex as:



Specific details for all assumed surface complexation reactions are further elaborated in subsequent sections.

For the U sorption experiments, the total concentration of U is known, as are the  $pK_a$  and site concentration for each MLGO sorption site (Table 3.1; as determined from the potentiometric titration modeling in Chapter 2). Hence, in conjunction with the equilibrium pH and the known equilibrium constants for the aqueous complexation reactions in each system (Table C.1), we use the measured extents of U sorption to constrain the value of the stability constants for a given U-MLGO surface complex. For example, the stability constant for Reaction 3.2 is given as follows:

$$K_{ads(i)} = \frac{[MLGO-L_i-(UO_2)^+]}{[MLGO-L_i^-] * a_{(UO_2)^{2+}}} \quad (3.3)$$

where  $a_x$  represents the activity of the species in the associated subscript, and brackets represent the molal concentration of surface species. FITEQL uses the Davies equation to calculate activity coefficients. Because different functional groups have distinct  $pK_a$  values, sorption measurements conducted as a function of pH place constraints on which sites are involved in the sorption reactions and these data can then be used to constrain the  $K_{ads}$  values for each important U-MLGO sorption reaction.

The goodness-of-fit for the U sorption modeling was quantified using the FITEQL variance parameter,  $V(Y)$ , defined as:

$$V(Y) = \frac{\sum \left( \frac{Y_{calc} - Y_{exp}}{S_{exp}} \right)^2}{n_p n_{II} - n_u} \quad (3.4)$$

where  $S_{exp}$  is the error associated with the model output,  $n_p$  is the number of modeled data points,  $n_H$  is the total number of components for which both free and total concentrations are known, and  $n_u$  is the total number of adjustable parameters in a system. The value of  $V(Y)$  depends not only on the residuals calculated from experimental ( $Y_{exp}$ ) and model-calculated ( $Y_{calc}$ ) values, but also the distribution of this error. Hence, the optimum  $V(Y)$  value is 1 (i.e., the variance is normally distributed), although experimental evidence suggests that values between 0.1 and 20 are common for reasonably good model fits (Westall, 1982).

### 3.4 Results and Discussion

#### 3.4.1 MLGO Nanosheet Characterization.

Figure 3.1 depicts a representative AFM image of MLGO particles from the stock suspensions used in this study. The intent of our AFM images was not to obtain a distribution of precise quantitative measurements of MLGO dimensions. However, these representative images indicate that MLGO suspensions mostly contained stacked particles ranging in height up to 10 nm. For comparison, the height of a single hydrated GO nanosheet is roughly 1 nm under AFM (Park and Ruoff, 2009; Zhang et al., 2010).

#### 3.4.2 MLGO-Free U Speciation Modeling

In order to determine which aqueous uranyl complexes form under our experimental conditions, we conducted chemical equilibrium modeling for MLGO-free systems with the same pH and background electrolyte conditions as our batch U sorption experiments. The most abundant aqueous complexes are presented in Figure 3.2 as a

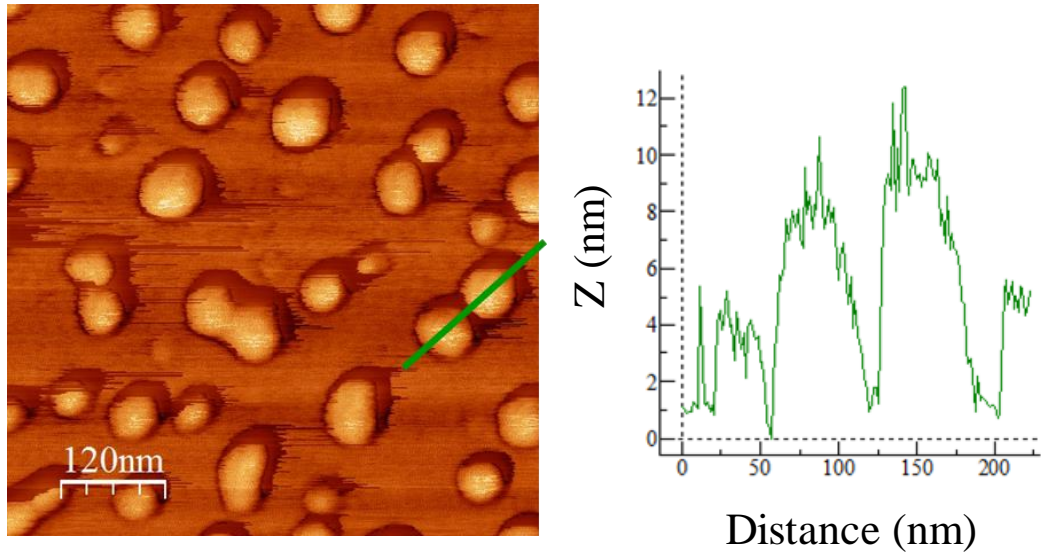


Figure 3.1: AFM image and height profile for the cross-section indicated in green for a representative MLGO particle. Note that the peak heights are ~10 nm.

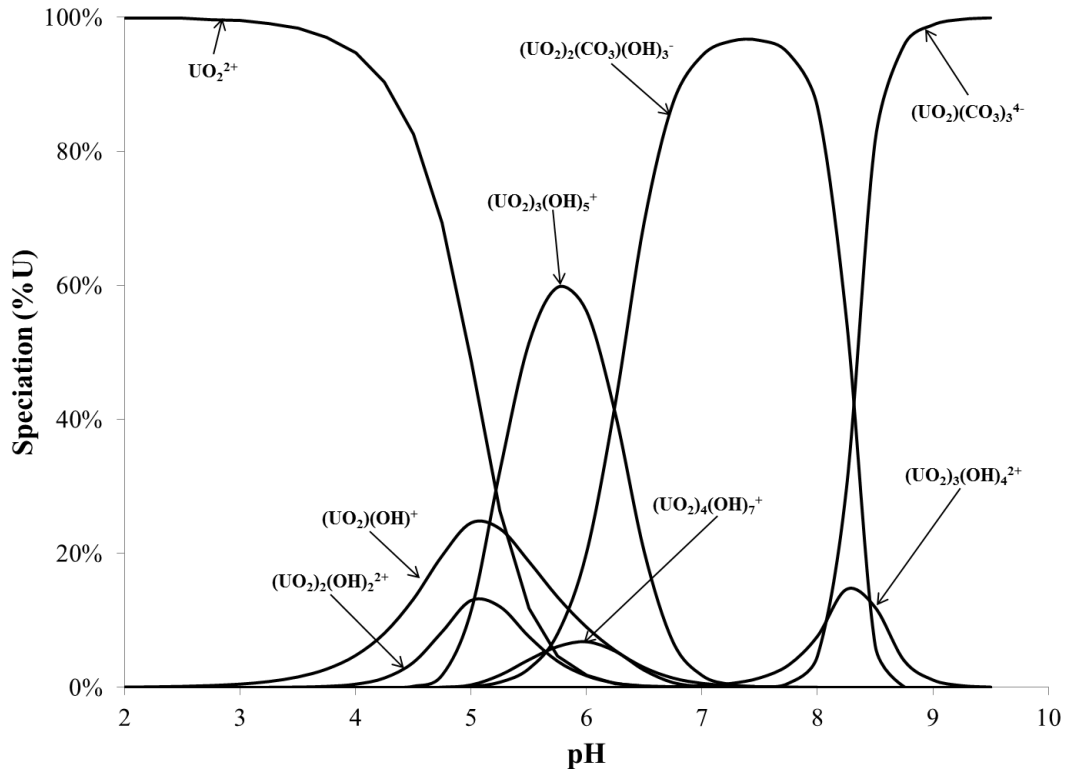


Figure 3.2: Aqueous U speciation modeling for MLGO-free systems in equilibrium with atmosphere. Only species that exceed 5% abundance are shown. The U concentration in this model is 3 ppm ( $1.3 \times 10^{-5}$  M) and the ionic strength is 1 mM with  $\text{NaClO}_4$  as the background electrolyte. The solution is in equilibrium with atmospheric  $\text{CO}_2$ . Species abundances are nearly identical for all ionic strengths below 100 mM.

function of pH. The uranyl ion ( $\text{UO}_2^{2+}$ ) dominates these systems below pH 5.2. While a number of aqueous uranyl hydroxides are present in relatively low abundances, the 3:5 uranyl:hydroxide complex  $[(\text{UO}_2)_3(\text{OH})_5^+]$  becomes the most abundant species between pH 5.2 and pH 6.3. At pH values above 6.3, the U speciation is dominated by negatively-charged aqueous uranyl complexes, including a 2:1:3 uranyl:carbonate:hydroxide  $[(\text{UO}_2)_2(\text{CO}_3)(\text{OH})_3^-]$  between pH 6.3 and pH 8.5, and a 1:3 uranyl carbonate

$[(UO_2)(CO_3)_3]^{4-}$  above pH 8.5. This speciation modeling informs our assumptions regarding surface complexes on MLGO particles.

### 3.4.3 Batch U Sorption Experiments

The cumulative results of the batch U sorption experiments are depicted in Figure 3.3. The U sorption edges for each ionic strength are comprised of two individual replicates, which largely overlap and are therefore not distinguished. As illustrated, MLGO particles exhibit a significant capacity to sorb U across a wide range of pH values. Sorption of U increases with increasing pH and is nearly independent of solution ionic strength, which is consistent with the findings of Zhao et al. (2012) for U binding onto few-layered GO nanosheets and suggests inner-sphere complexation at the MLGO surface (Bradbury and Baeyens, 2002; Yang et al., 2011). At very low pH (< 3.5),  $pK_a$  values for MLGO particles (Table 3.1) suggest that most surface sites are protonated, and consequently we measured relatively low extents of U sorption. As pH increases, MLGO surface functional groups are increasingly deprotonated to become negatively-charged and we attribute the dramatic increase in sorption from pH 2 to pH 5 to the binding of the positively-charged  $UO_2^{2+}$  complex that dominates U speciation in this pH range. At the MLGO surface site:U molar concentration ratio utilized in this study (~45), we measured complete sorption of U between pH 5 and pH 7.5, where sorption gradually diminishes but remains at values above 80% through pH 9.5. The measured extent of U sorption at high pH for MLGO is significantly higher than that measured in sorption studies using hematite (Murphy et al., 1999; [Site]:[U] = 600) or ferrihydrite (Waite et al., 1994; [Site]:[U] = 205), despite having significantly higher site:U molar ratios than those of our

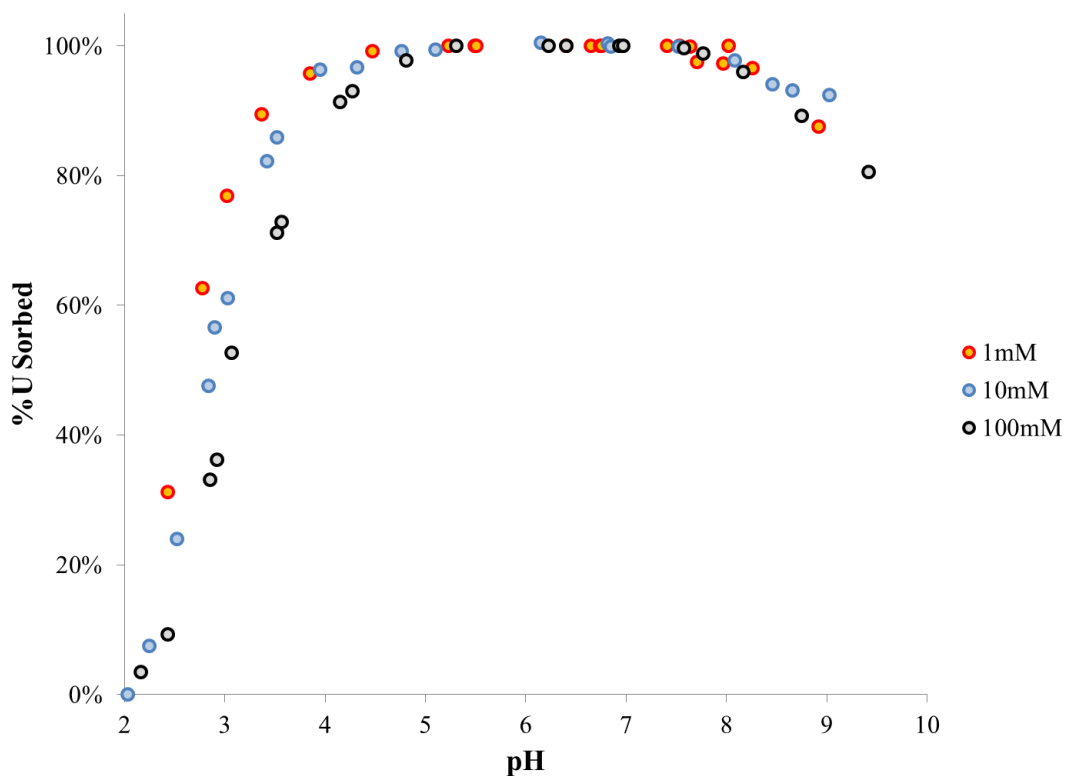


Figure 3.3: Sorption of U ( $1.26 \times 10^{-5}$  M) by MLGO particles ( $210 \text{ mg L}^{-1}$ ) as a function of both pH and ionic strength. Red, blue, and black circles indicate the sorption edges for 1 mM, 10 mM, and 100 mM ionic strength treatments, respectively.

study. Each of these iron oxide bearing studies illustrates precipitous declines in U sorption above pH  $\sim 8.7$ .

We tested the ability of surface complexation modeling to account for the observed U sorption behaviors. The aqueous  $UO_2^{2+}$  complex dominates U speciation through pH 5.2 (Figure 3.2), and thus, we began by using the experimental data collected below pH 5.2 for each ionic strength to characterize the sorption of  $UO_2^{2+}$  onto deprotonated Site 1, as in Reaction 3.2. Using only the  $\text{pH} \leq 5.2$  data, the Log  $K_{ads}$  values for the 1 mM, 10 mM, and 100 mM ionic strength treatments are calculated as 5.87, 5.70,

and 5.72, respectively (Table 3.2). The similarity in the calculated stability constants from the different treatments is a strong indication that the measured extents of sorption through pH 5.2 are virtually independent of ionic strength. Furthermore, the slight difference in sorption behaviors between ionic strength treatments that do exist can successfully be described by changes to activity coefficients within FITEQL. Hence, we average these values ( $\text{Log } K_{ads} = 5.76$ ) and use this singular  $\text{Log } K_{ads}$  to predict the sorption behavior for each ionic strength treatment across the entire pH range studied (Figure 3.4). This model provides a very good fit to the measured sorption extents below approximately pH 5.5, while significantly underestimating the extent of U sorption at higher pH values. This underestimation is due to the dramatic decrease in the concentration of the  $UO_2^{2+}$  species with increasing pH above pH 5.2, and represents clear and compelling evidence for the importance of at least one additional U surface complex at pH values above 5.5.

The significant sorption ( $\geq 80\%$ ) of U by MLGO particles through pH 9.5 strongly suggests that aqueous uranyl hydroxides [e.g.,  $(UO_2)_3(OH)_5^+$ ], and perhaps aqueous uranyl (hydroxy-) carbonates [e.g.,  $(UO_2)_2(CO_3)(OH)_3^-$  or  $(UO_2)(CO_3)_3^{4-}$ ] can sorb to the functional groups associated with MLGO surfaces, as MLGO-free U speciation modeling indicates that these aqueous complexes dominate at mid- to high-pH values. However, for each of our ionic strength treatments, we observed  $\sim 100\%$  sorption of U by MLGO particles prior to pH 5.2, where these aqueous uranyl complexes become dominant. Hence, our data do not allow us to utilize surface complexation modeling to constrain the values of the stability constants associated with these potential reactions. In addition, as

TABLE 3.2  
 STABILITY CONSTANT VALUES FOR THE URANYL-MLGO SORPTION  
 REACTION CALCULATED USING A NON-ELECTROSTATIC SURFACE  
 COMPLEXATION MODEL

Uranium Sorption Reaction	Log $K_{ads}$ values			
	1 mM Ionic Strength	10 mM Ionic Strength	100 mM Ionic Strength	AVERAGE
$GO-L_1^- + UO_2^{2+} \leftrightarrow GO-L_1-UO_2^+$	5.87	5.70	5.72	<b>5.76</b>
Goodness-of-fit Estimate, $V(Y)$	0.37	0.58	0.30	<b>0.42</b>

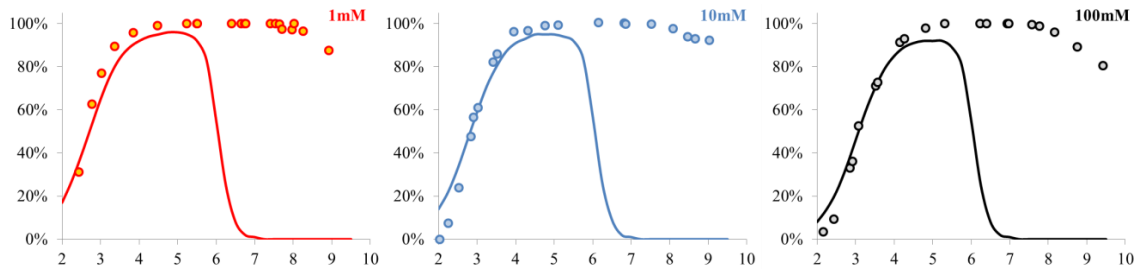


Figure 3.4: Prediction of U sorption behavior using a non-electrostatic model that assumes sorption of  $UO_2^{2+}$  to Site 1 only, with a  $\text{Log } K_{ads} = 5.76$  for this reaction. Prediction curves are shown in relation to actual measured U sorption extents for three ionic strength treatments. Axes are as follows: X (pH); Y (%U Sorbed).

these systems move toward higher pH values, significant uncertainties exist regarding the concentration of dissolved CO<sub>2</sub>, which could lead to unacceptably large uncertainties for the calculated stability constant values. Still, given that the measured U sorption extents remain high for all ionic strengths at pH values beyond the existing model fits, we conclude that the binding of at least one other aqueous uranyl complex onto MLGO surface sites contributes to the overall U sorption behavior.

The lack of an ionic strength effect in the sorption of U by MLGO is not necessarily inconsistent with the finding of Chapter 2, which found a strong influence of ionic strength on Cd and Pb binding. To illustrate this point, we incorporate into the model presented in Table 3.2 and Figure 3.4 the following reaction at each surface site:



We determined in Chapter 2 that by setting the Log  $K_{Na-ads}$  of this reaction equal to 1.0, we can achieved a reasonable fit to the measured Cd and Pb sorption extents for each of the ionic strengths evaluated. If we set the Log  $K_{Na-ads}$  value for Reaction 3.5 at 1.0 in our model of U sorption, we discern very little change in the model fit (Figure C.1). It is quite likely that the aqueous uranyl complexes that dominate U speciation at each pH value compete more effectively with the background electrolyte for MLGO surface sites, relative to Cd or Pb species.

### 3.5 Conclusions

MLGO exhibits an extraordinary ability to sorb U across a range of environmental conditions. Measured extents of sorption increased with increasing pH, but were virtually independent of ionic strength. These data suggest the formation of inner-sphere complexes at the MLGO surface sites. We used a 4-site non-electrostatic surface complexation model to calculate the stability constant for the uranyl-MLGO surface complex, which accounts for the U sorption behavior through pH 5.5. However, we observed that MLGO retains its capacity to sorb U at very high pH values, unlike many other natural and engineered materials, which provides unequivocal evidence for the formation of other U-MLGO surface complexes involving aqueous uranyl hydroxides and/or (hydroxy-) carbonates. We need complementary spectroscopic data to identify the U species and MLGO surface sites associated with these complexation reactions. Our findings, when considered in relation to the findings of Chapter 2, indicate that U may better compete with other environmental constituents, such as high electrolyte concentrations, for MLGO sorption sites. Our results demonstrate that MLGO could be particularly useful for the remediation in high-ionic strength, high-pH environments where U is typically poorly sorbed by other materials.

### 3.6 Acknowledgments

This research was supported, in part, by a fellowship to T.D. from the Arthur J. Schmitt Foundation. In addition, we performed most experiments and analyses using instrumentation at the Center for Environmental Science and Technology (University of

Notre Dame). I also acknowledge a substantial technical contribution by Jennifer Szymanowski.

CHAPTER 4:  
INFLUENCE OF PH AND IONIC STRENGTH ON THE DEPOSITION RATES OF  
SINGLE-LAYERED GRAPHENE OXIDE NANOSHEETS IN QUARTZ AND IRON  
OXIDE COATED SAND COLUMNS

#### 4.1 Abstract

The fate and transport of nanomaterials in natural environments and engineered remediation systems is partially determined by their deposition onto the surfaces that comprise soil and groundwater matrices. One such nanomaterial, called single-layered graphene oxide (SLGO), exhibits unique dimensions and a large, highly-reactive surface area, and we hypothesize that these properties strongly influence their interactions with stationary-phase environmental constituents. Hence, in this study, we investigated the influence of environmentally-relevant pH values (5.6 to 8.3) and ionic strengths (10 mM and 50 mM) on the transport of SLGO through laboratory columns filled with either quartz or iron oxide coated sands. We observed very little deposition in systems containing quartz sands, particularly for low ionic strength and high pH systems. Electrophoretic mobility measurements for SLGO nanosheets and quartz sand indicated that both of these surfaces are negatively-charged throughout the conditions of this study. However, increasing ionic strength and decreasing pH served to diminish the magnitude of the negative charge near these surfaces, thereby limiting repulsion and increasing deposition. SLGO nanosheets were deposited in the columns packed with iron oxide

coated sands to a much greater extent than in columns packed with quartz sands. The iron oxide coated sands exhibit a  $\text{pH}_{pzc} > 8.3$ , and thus, SLGO nanosheets and the iron oxide coated sands were oppositely-charged throughout the experimental range, which served to increase deposition. The deposition rates of the high ionic strength iron oxide coated sand treatments, relative to those of the other experimental treatments, could not be explained by electrostatic interactions alone, and instead may be influenced by nanosheet aggregation.

## 4.2 Introduction

At the nanoscale, natural flake graphite is comprised of atomically-thin graphene laminations, with each layer consisting of a hexagonal network of  $\text{sp}^2$  bonded carbon atoms (Novoselov et al., 2004; Allen et al., 2010). Exposure of graphite to a strong mix of acids and chemical oxidants results in oxidized particles called graphene oxide (GO), and subsequent sonication exfoliates the individual laminations from the bulk material to form a stable suspension of single-layered GO (SLGO) nanosheets (Stankovich et al., 2007). The resulting SLGO nanosheets exhibit a high degree of anisotropy, measuring only a single atom in thickness and up to several micrometers in diameter when completely exfoliated.

The exact chemical structure of GO is a matter of significant debate in the literature and likely varies based on the quality of the graphite used and its level of oxidation (Szabó et al., 2006a; Dreyer et al., 2010). However, it is generally agreed that the oxidation of graphene laminations serves to interrupt and decorate the regular lattice of six-membered carbon rings with various oxygen-containing functional groups, which

may include covalently-bonded epoxide, ketone, and hydroxyl groups on the basal planes, and carboxylic, lactol, and phenolic groups at the edges (Lerf et al., 1998; Szabó et al., 2006a; Gao et al., 2009; Lee et al., 2010). Collectively, these proton active functional groups populate the surface at an average density of approximately 1 site/nm<sup>2</sup>, with nanosheet surface areas exceeding 1800 m<sup>2</sup>/g (Szabó et al., 2006b).

Hence, GO nanosheets are characterized by an extremely large and reactive surface area for interactions with mobile- and stationary-phase environmental constituents. In fact, GO-bearing systems exhibit extraordinarily high sorption capacities for compounds ranging from metal ions (Zhao et al., 2011a, 2011b, 2012) to the complex molecules present in antibiotics (Gao et al., 2012), organic contaminants (Ion et al., 2011), cationic dyes (Zhang et al., 2011), and natural organic matter (Hartono et al., 2009), and consequently, GO nanosheets hold significant potential for *in situ* and *ex situ* remediation applications. Additional uses of GO nanosheets are proposed in the fields of advanced materials, electronics, and biomedical engineering (Zhu et al., 2010; Wang et al., 2011). The burgeoning utility of GO nanosheets in these remediation and consumer applications increases the likelihood of both controlled and uncontrolled environmental releases, making it increasingly important to identify factors that influence the mobility and transport of GO nanosheets in soils and groundwater systems.

While the literature is replete with transport studies associated with other colloidal materials, the distinctive dimensions, extreme anisotropy, and large reactive surface area of SLGO nanosheets represent a unique combination of attributes from which to explore existing transport models. For example, relative to SLGO nanosheets, clay particles are characterized by a similar plate-like morphology, but exhibit dramatically lower surface

areas per mass unit (generally  $< 300 \text{ m}^2/\text{g}$ ; Dogan et al., 2006, 2007) for interactions with stationary collectors. Conversely, the chemical composition and surface area per unit mass (up to  $\sim 1300 \text{ m}^2/\text{g}$ , depending on the number of outer walls; Peigney et al., 2001) of carbon nanotubes are comparable to that of SLGO nanosheets, but their distinctive long, slender aspect strongly influences their transport behavior (Jaisi et al., 2008; Jaisi and Elimelech, 2009). Hence, we anticipate that the novel blend of chemical and physical characteristics exhibited by SLGO nanosheets can provide a unique prospective on factors that influence the transport of colloidal material through environmental systems.

Hence, in this study, we investigated the influence of environmentally-relevant pH (5.6 to 8.3) and ionic strength (10 mM and 50 mM), as well as sand grain surface coatings (quartz and iron oxide), on the transport of SLGO nanosheets through laboratory column-based saturated porous media. We establish herein that the relative electrochemical properties of the nanosheet and collector surfaces, as determined by the pH and ionic strength of a given treatment, are the primary factors influencing the transport of SLGO through saturated porous media.

## 4.3 Experimental Procedures

### 4.3.1 SLGO Preparation and Characterization

SLGO nanosheets were synthesized from natural flake graphite (Alfa Aesar, 99.9995%) using the Hummer's method (Hummers and Offeman, 1958). Briefly, graphite was mixed with  $\text{NaNO}_3$ ,  $\text{H}_2\text{SO}_4$ , and  $\text{KMnO}_4$  in an ice bath. The mixture was then transferred to a water bath at  $35 \text{ }^\circ\text{C}$  and stirred for 30 minutes. Next, ultrapure water ( $R > 18 \text{ M}\Omega \text{ cm}$ ,  $\text{TOC} < 2 \text{ }\mu\text{gC L}^{-1}$ ) was added and the mixture was stirred for

approximately 20 minutes. Residual permanganate was then consumed by the addition of hydrogen peroxide. Finally, GO was collected by centrifugation, washed repeatedly with ultrapure water, and freeze-dried under vacuum for 5 to 7 days before use. The resulting dried mass was then dispersed in ultrapure water using end-over-end rotation. The suspension was sonicated (40kHz; Fisher Scientific 140) in a water bath for one hour and subsequently centrifuged in multiple 15 mL aliquots for 10 minutes at  $3000 \times g$ , which served to sediment the multi-layered GO aggregates and concentrated the SLGO nanosheets in the supernatant. All supernatants were decanted and combined into a single stock suspension with a final concentration of  $2.1 \text{ g SLGO L}^{-1}$ , as determined from the average difference between the wet and dried ( $105 \text{ }^\circ\text{C}$  for  $>24$  hours) masses of multiple 20 mL aliquots of the final suspension. We conducted all subsequent characterization and transport experiments using this stock SLGO suspension or its dilution.

We characterized the physical and electrochemical properties of the SLGO nanosheets that were used in subsequent transport experiments using atomic force microscopy (AFM), UV-visible (UV-vis) spectrophotometry, and electrophoretic mobility (EPM) measurements. Prior to examination by AFM (XE-70, Park Systems, Santa Clara, CA), an aliquot of the SLGO stock suspension was diluted 1:4 with ethanol and deposited on freshly cleaved mica. The instrument was operated in non-contact mode and images were flattened using the WSxM software package from Nanotec Electronica S.L. (Madrid, Spain). The AFM analyses resulted in determination of z-dimension, or height, which we used to infer the extent of exfoliation present in the SLGO nanosheet suspension. In addition, we obtained the UV-vis absorption spectrum

( $\lambda = 200$  and  $800$  nm) of a  $25$  mg SLGO  $L^{-1}$  suspension using a 6Q quartz cuvette. As will be seen, the results from this survey indicated a peak UV-vis absorbance at approximately  $\lambda = 230$  nm, which we utilized to illustrate the breakthrough of SLGO nanosheets during the column transport studies. Finally, for each ionic strength evaluated during the transport studies ( $10$  mM and  $50$  mM), we measured EPM (Zetasizer Nano-ZS, Malvern Instruments, Worcestershire, United Kingdom) along a gradient of pH values ( $\sim 0.4$  s.u. resolution) between approximately pH  $5.5$  and pH  $8.5$ . Ionic strength was buffered by adding the appropriate mass of  $NaClO_4 \cdot H_2O$  powder to a  $25$  mg SLGO  $L^{-1}$  suspension, while pH was titrated upwards with serial NaOH additions. Aliquots from the titrated suspension were removed and measured after  $\sim 5$  minutes of exposure time at the target pH.

#### 4.3.2 Porous Media Preparation and Characterization

Quartz sand (Accusand, Unimin Corporation, LeSueur, MN) was utilized as the solid phase medium for all uncoated sand column experiments and as the base grain for all iron oxide coated sand column experiments. Supplier specifications indicate that the quartz sand passed through the openings of a 40 mesh sieve ( $0.42$  mm) while being retained on a 50 mesh sieve ( $0.29$  mm), which defines the range of potential grain sizes. The quartz sand was sonicated and rinsed with ultrapure water approximately ten times to remove loosely-associated colloidal debris and soaked overnight in 10% HCl on two occasions to remove metal contaminants. After each overnight acid wash, the quartz sand was rinsed thoroughly with ultrapure water until the rinsate returned to circumneutral pH.

Iron oxide coated sand grains were produced by adding 150 g of the acid-washed quartz sand to each of two 600 mL beakers containing 400 mL of 0.05 M  $\text{Fe}(\text{NO}_3)_3$ . While stirring vigorously, the suspension was slowly titrated using 6 M NaOH until the pH exceeded 6.0. At this point, precipitation of an iron oxyhydroxide was observed on the quartz grains and after 3 hours of vigorous stirring, the entire suspension was transferred to capped polypropylene bottles and rotated end-over-end overnight. After settling the sand in these containers and decanting the supernatant, the sand was rinsed with ultrapure water, which liberated iron oxide precipitates that were not adhered to a sand grain. We repeated this rinse step over 20 times, at which time the UV-Vis absorbance of the rinsate was less than 0.05 at all points between  $\lambda = 200$  and 800 nm. The iron oxide coated sand was oven-dried at 60 °C for approximately 12 hours. The rinsed and dried iron oxide coated sand was distinctly reddish-brown and measurements (described in subsequent sections) indicated a significant amount of iron oxide precipitate was present at the quartz sand surface after only one coating. In order to facilitate direct comparison between the quartz and iron oxide coated sand experiments, we opted against conducting additional coatings that could increase the grain size and hence change the pore geometries of the solid phase matrix, relative to the pure quartz sand.

Morphological and chemical characteristics of individual grains from the quartz and iron oxide coated sands were established via scanning electron microscopy (SEM; Leo-EVO 50, Carl Zeiss, Oberkochen, Germany) coupled to an energy dispersive X-ray spectrometer (EDX; Oxford Instruments, Oxfordshire, United Kingdom). In addition, surface associated colloidal material was removed from the quartz and iron oxide coated sand grains via probe sonication (using a total cycle time of 20 minutes at 39 W) and

vigorous vortexing (3200 rpm), respectively, and this material was subjected to an EPM titration, as described earlier for the SLGO suspensions. We assume that the near-surface charge of a sand grain is largely determined by the surface associated colloidal material, similar to Smith et al. (2008). The relatively mild procedure for collecting colloidal material from the iron oxide coated sands protected the resulting suspension from contamination with colloidal silica from the underlying sand grain.

#### 4.3.3 Column Transport Studies

All SLGO transport studies were conducted using borosilicate glass columns (FlexColumn, Kimble-Kontes Scientific) measuring 10.0 cm long by 1.0 cm in diameter. For both quartz sand and iron oxide coated sand experiments, 8.0 g of material was rinsed twice with ionic strength buffer and ultrapure water to remove loosely-associated colloidal material, and then slowly added to a column prefilled with ultrapure water. The sand was settled by vigorously vibrating and tapping the filled columns, and excess water was removed using a pipette. Fresh quartz sand and iron oxide coated sand was packed into each column prior to the start of an experimental run. By carefully tracking the mass of the empty and the packed column, we established that the columns packed with either the quartz sand or iron oxide coated sands exhibited an average pore volume of 1.61 mL ( $\sigma = 0.03$  mL). The height of sand within each column was a constant at 6.0 cm throughout all experimental treatments. Combined, these values result in an average calculated porosity of 0.34 for each experimental system. All phases of the column transport studies described below were conducted using an influent flow rate of 1 mL/min, which resulted in an approach (superficial) velocity of  $0.0212 \text{ cm sec}^{-1}$ .

Prior to the start of an experiment, each packed column was initially rinsed with 12.5 pore volumes (i.e., 20 minutes) of ultrapure water (which is not accounted for on subsequent figures). Columns were then conditioned to the target pH and ionic strength conditions for each respective experimental treatment. An ionic strength of either 10 mM or 50 mM was achieved using appropriate additions of  $\text{NaClO}_4 \cdot \text{H}_2\text{O}$ , while influent pH was adjusted to and maintained at ( $\pm 0.1$  s.u. for each pH) the environmentally-relevant values of pH 5.6, 7.0, and 8.3 using repeated additions of NaOH, as needed. After 12.5 pore volumes of conditioning, flow to the column was switched to a solution containing 25 mg SLGO  $\text{L}^{-1}$  suspended in the identical background electrolyte used to condition the column. The SLGO suspension flowed continuously through the column for 50 pore volumes, at which time, the flow was again switched back to the SLGO-free background electrolyte solution for an additional 12.5 pore volumes.

To measure the effluent SLGO concentration during SLGO breakthrough from the columns, we monitored absorbance of the column effluent at  $\lambda = 230$  nm ( $C_t$ ) at 6 second intervals using a spectrophotometer equipped with a 1-cm flow-through quartz cuvette. At this wavelength,  $C_t$  is linearly correlated with SLGO concentration (Figure D.1) and decreases in peak height were the only change observed in the UV-vis spectra of the SLGO suspension after transport through the column (see discussion in later sections). Hence, normalizing the  $C_t$  values to the initial absorbance of the influent SLGO suspension ( $C_0$ ) results in breakthrough curves that relate the normalized concentration ratio ( $C_t/C_0$ ) to the numbers of pore volumes that have passed through the column. Column transport studies for each pH and ionic strength treatment condition were conducted at least in duplicate. Replicate runs largely overlap, and thus, an average

breakthrough curve is presented for each treatment in subsequent figures and analyses, with the actual replicate data presented in Appendix E.

In addition to the above experiments, in order to account for the internal volume of our overall flow system and specific column dispersion characteristics, we separately monitored ( $\lambda = 218$  nm) the breakthrough of a 5 mM NaBr conservative tracer solution using the identical flow-through UV-vis spectrophotometer setup we previously described. We conducted NaBr tracer experiments at each of the six treatment conditions utilized in the SLGO-bearing quartz sand experiments. The breakthrough curves for all NaBr tracer experiments largely overlapped (Figure D.2), indicating that the ionic strength and pH conditions in the associated electrolyte do not impact the conservative nature of the NaBr tracer within quartz sand columns. Hence, we averaged the NaBr tracer breakthrough curves from the quartz sand experiments and used this single curve as our basis of comparison for all treatment conditions, including the iron oxide coated sand experiments. We deemed the use of a single NaBr breakthrough curve appropriate, regardless of the surface coating, because the overall volume of the flow system did not change with addition of the iron oxide coated sands, as the average pore volume existing within each type of column remained constant. In addition, we note that, in contrast to the quartz sand tracer experiments, NaBr transport is significantly retarded by the positively-charged surfaces within the iron oxide coated sand columns (data not shown) indicating that NaBr is not a conservative tracer for these treatments.

#### 4.3.4 Quantitative Characterization of Transport Parameters

When colloid release rates are small (e.g., irreversible sorption), the transport of colloidal particles through porous media under steady-state saturated flow conditions is

traditionally described using a modified mobile-immobile advection-dispersion equation (Kretzschmar et al., 1999) as follows:

$$\frac{\partial C}{\partial t} = D_p \frac{\partial^2 C}{\partial x^2} - v_p \frac{\partial C}{\partial x} - k_d C \quad (4.1)$$

where  $C$  is the concentration of suspended particles,  $D_p$  is the dispersion coefficient,  $v_p$  is the average linear water velocity,  $x$  is the travel distance in the direction of water flow, and  $k_d$  is the colloid deposition rate coefficient. The first two terms on the right side of Equation 4.1 represent dispersive and advective transport, respectively. For systems exhibiting high Peclet numbers ( $Pe > 30$ ; i.e., where dispersive transport is negligible, relative to advective transport), Equation 4.1 reduces to the following estimate for the colloid deposition rate coefficient,  $k_d$ :

$$k_d = -\frac{U}{fL} \ln\left(\frac{C}{C_0}\right) \quad (4.2)$$

where  $f$  is the packed bed porosity,  $U$  is the approach velocity,  $L$  is the length of the packed bed, and  $C / C_0$  is the breakthrough concentration or the fraction of colloids observed in the column effluent after the breakthrough curve reaches a plateau (Kretzschmar et al., 1997, 1999). The first term in Equation 4.2 equates to the average travel time of colloidal particles through the column, making  $k_d$  a time- and distance-averaged parameter. In addition, for clarity and consistency with filtration theory (Yao et

al., 1971), we note that the deposition rate coefficient is proportional to the single collector efficiency ( $\eta$ ) using the following:

$$k_d = \frac{3(1-f)U}{2fd_c} \eta \quad (4.3)$$

where  $d_c$  is the grain diameter for the collector grains.

Particularly in step-input column experiments, where the constant flow of a colloidal suspension delivers significant particle quantities to a column over time, colloid attachment rates may be strongly influenced by previously-sorbed colloids that are filling or otherwise blocking sorption sites. In order to apply the modeling approach above, we must define the  $C / C_0$  term of Equation 4.2 as the normalized *clean-bed* breakthrough concentration at a point where attachment sites are not limiting. While previous studies identify the clean-bed breakthrough concentration at between 1.8 and 2.0 pore volumes beyond sample introduction (Redman et al., 2004; Jaisi et al., 2008), our definition requires consideration of a slightly larger internal system volume (e.g., a larger volume cuvette). Hence, for our determination of  $k_d$ , we obtain the normalized clean-bed breakthrough concentrations at ~5.5 pore volumes after beginning the constant injection of the SLGO suspension to the column, which equates to 18 total pore volumes from the start of the experiments (when considering the 12.5 pore volumes of conditioning), as indicated on subsequent figures. This estimation of the clean-bed breakthrough concentration is read from a point on the breakthrough curve where the  $C_t / C_0$  value of the conservative NaBr tracer exceeds 0.99, making it approximately equivalent to the measurements from other studies.

Finally, we also compare the calculated  $k_d$  values for each of our experimental treatments to the  $k_d$  value from an electrostatically-favorable deposition condition to establish an attachment efficiency ( $\alpha$ ). As will be seen in subsequent sections, SLGO nanosheets are negatively-charged throughout the range of experimental conditions in this study, while our iron oxide coated sand grains exhibit a positive charge at the pH values studied, particularly at our lowest pH. Hence, we designate the  $k_d$  value from the 50 mM ionic strength, low pH, iron oxide coated sand treatment as  $k_{d,fav}$ , and calculate the attachment efficiency ( $\alpha$ ) as:

$$\alpha = \frac{k_d}{k_{d,fav}} \quad (4.4)$$

The  $k_d$  and  $\alpha$  values for each experimental treatment condition were the metrics used to compare and evaluate the transport of SLGO nanosheets through systems that vary in pH, ionic strength, and collector grain coatings.

## 4.4 Results and Discussion

### 4.4.1 SLGO Nanosheet Characterization

We characterized the physical and electrochemical properties of the SLGO nanosheets utilized in this study via AFM, UV-vis spectrophotometry, and EPM. Figure 4.1 depicts a representative non-contact AFM image from a dilution of the SLGO nanosheet suspension utilized for subsequent transport experiments. The image indicates that the particles exhibit relatively flat and irregular morphology, consistent with the

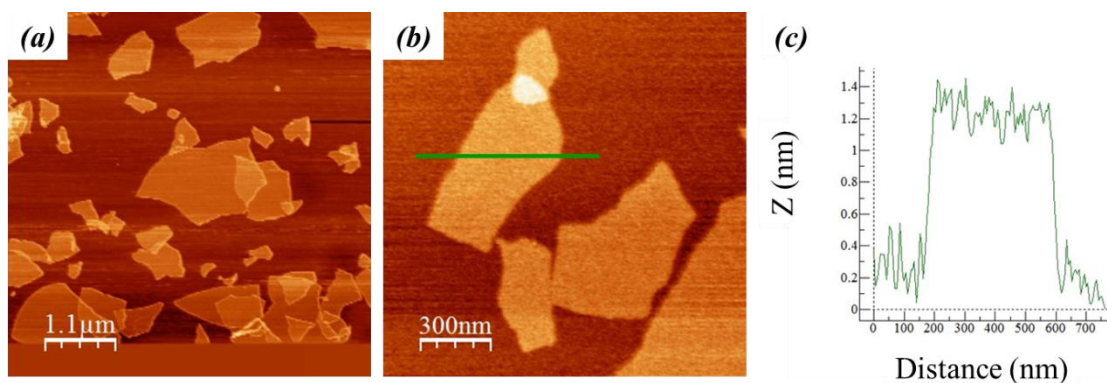


Figure 4.1: Two characteristic non-contact AFM images of SLGO nanosheets deposited on freshly-cleaved mica. Note the change in scale between images (a) and (b). Panel (c) illustrates the height or z-dimension profile from the cross-section depicted in green on Panel (b). Collectively, these panels indicate the dominant presence of SLGO nanosheets that have been completely exfoliated.

character of other SLGO nanosheets in the literature (Chen et al., 2009; Gao et al., 2009). Nanosheets in this study exhibited a heterogeneous size distribution in terms of particle length and width, measuring from several hundred nanometers to approximately 1.5 μm in diameter (Figure 4.1a,b). However, SLGO heights generally ranged between 1.0 and 1.5 nm (Figure 4.1c), which is indicative of single-layered nanosheets (Park and Ruoff, 2009; Zhang et al., 2010). Hence, the SLGO nanosheets utilized in this study exhibited extraordinary anisotropy, which is expected to play a significant role in their transport through porous media.

Prior to each transport study, we obtained a UV-vis absorption spectrum from the initial 25 mg SLGO L<sup>-1</sup> suspension that was delivered to the packed column and obtained several additional spectra from the column effluent during the study (Figure 4.2).

Regardless of the ionic strength and pH conditions of the background electrolyte, all UV-

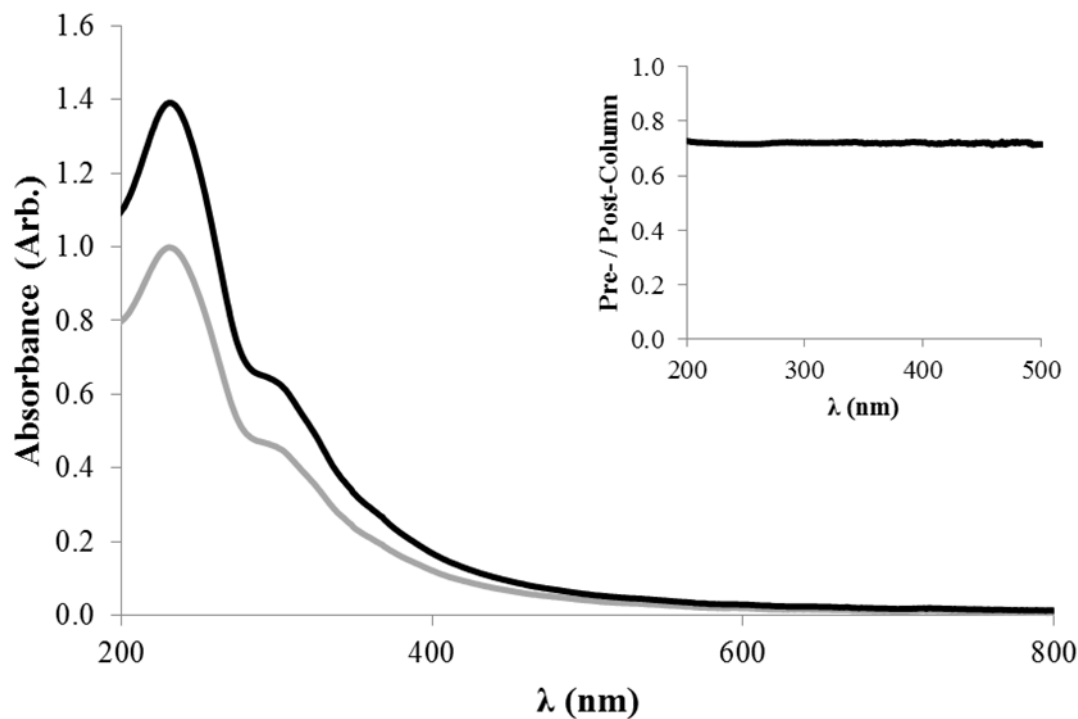


Figure 4.2: Typical UV-vis absorption spectra for a 25 mg SLGO L<sup>-1</sup> suspension before (black) and after (grey) passing through a column packed with a porous media. This particular example is from a quartz sand experimental treatment exhibiting an ionic strength of 50 mM and an effluent pH ~5.6. The inset figure illustrates the relationship between the pre- and post-column absorbance values, which remains constant throughout the wavelength range depicted.

vis spectra from the initial stock suspensions were in general agreement with each other and exhibited a peak absorbance between  $\lambda = 230$  and 232 nm and a distinctive shoulder feature around 300 nm, which is characteristic of GO nanosheets and consistent with similar analyses in the literature (Li et al., 2008; Zhang et al., 2010; Gao et al., 2012). UV-vis spectra from effluent suspensions exhibited lower peak heights, as expected to indicate a change in SLGO concentration, but were otherwise identical to the spectra

from the pre-column stock suspension. The consistency between pre- and post-column UV-visible spectra (Figure 4.2, inset) indicates the absence of chemical transformations (e.g., reduction; Li et al., 2008) or contamination of SLGO nanosheets within the column. This observation, combined with the linearly-proportional relationship between SLGO concentration and the absorbance of an SLGO suspension at  $\lambda = 230$  nm (Figure D.1), indicate that tracking UV-vis absorbance in the column effluent is a robust measure of SLGO transport through quartz and iron oxide coated sands.

#### 4.4.2 Porous Media Characterization

Figure 4.3 presents SEM images for representative quartz sand and iron oxide coated sand grains. Both grain types appear to be heavily coated with colloidal material. EDX spectroscopy measurements confirm the presence of an iron-bearing coating on the iron oxide coated sands, whereas quartz sands are only comprised of the elements silicon and oxygen.

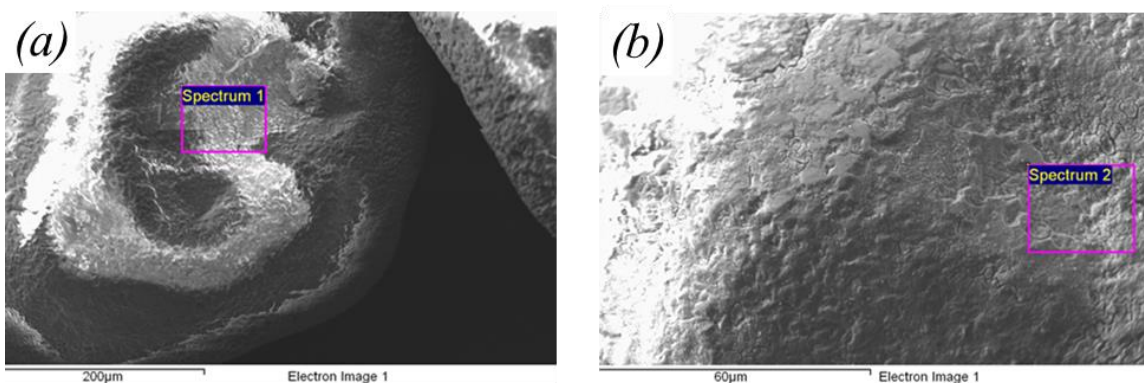


Figure 4.3: Representative SEM images of (a) an uncoated quartz sand grain, and (b) an iron oxide coated sand grain. Note the change in scale between the two images. EDX spectra from the indicated boxes illustrate an extensive presence of iron in (b).

#### 4.4.3 Electrokinetic Characterization of SLGO and Collector Grains.

Figure 4.4 illustrates the EPM measurements for SLGO nanosheets, quartz sand grains, and iron oxide coated sand grains exposed to the pH range (~5.5 to ~8.5) and ionic strengths (10 mM and 50 mM) of interest. EPM from the collector sand grains were obtained by removing some surface-associated colloidal material from the quartz and iron oxide coated sand grains via probe sonication and vigorous vortexing, respectively. The near-surface charge of the surface-associated colloidal material can be used as a proxy for the surface charge of an individual grain (Smith et al., 2008).

The SLGO nanosheets and quartz sand colloids are negatively charged throughout the range of pH and ionic strengths utilized in this study. EPM values ranged from -1.5 to  $-3.3 \mu\text{m cm V}^{-1} \text{s}^{-1}$  for quartz sand colloids and -2.0 to  $-3.5 \mu\text{m cm V}^{-1} \text{s}^{-1}$  for SLGO nanosheets, depending on pH and ionic strength conditions. Increases in ionic strength caused a decrease in the magnitude of these negative charges, as a concentration-dependent build-up of counter ions from the background electrolyte near the particle surfaces compresses the size of the electric double layer and screens some of the surface charge. In addition, increasing pH favors the deprotonation of surface-associated functional groups, thereby leading to more negatively-charged surfaces at high pH. Functional groups associated with the surfaces of SLGO nanosheets include carboxyl, epoxide, and hydroxyl groups (Lerf et al., 1998; Szabó et al., 2006a; Gao et al., 2009), whereas proton-active groups on the quartz sand surface are likely hydroxyl edge sites (Pagnanelli et al., 2006).

Iron oxide coated sand colloids are positively charged at all but the highest pH values evaluated and, relative to quartz sand colloids, are not as sensitive to changes in

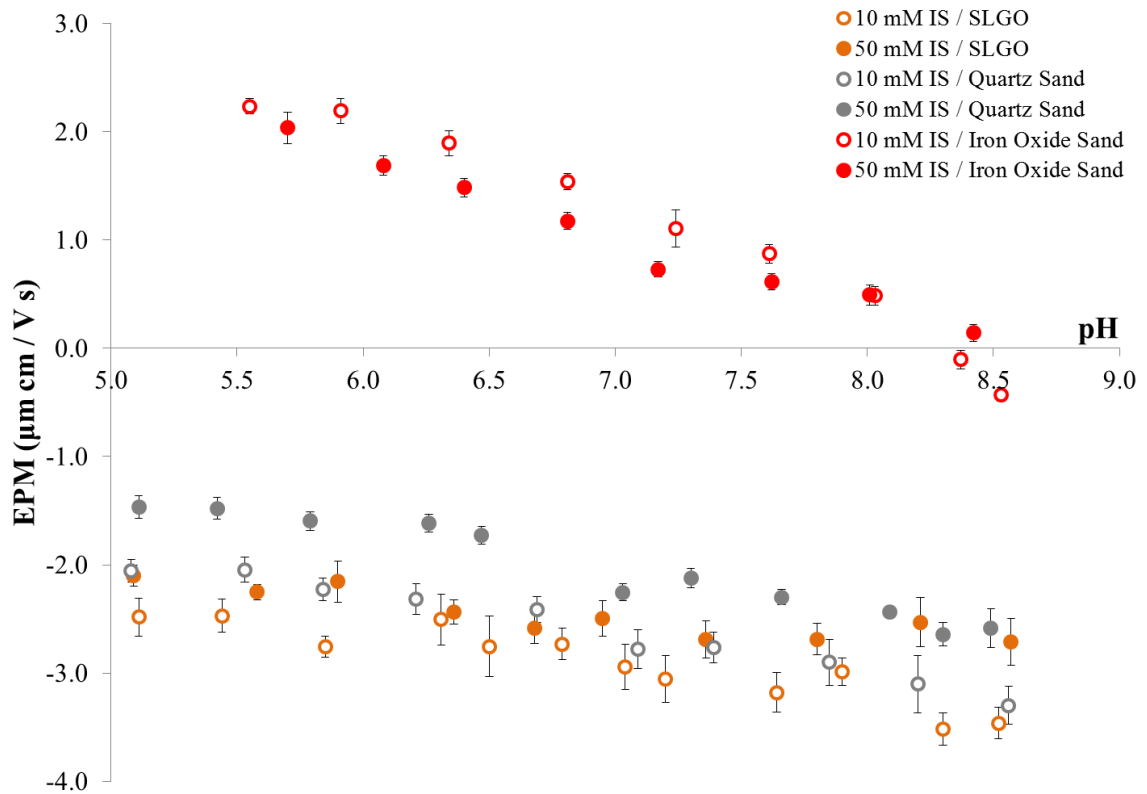


Figure 4.4: Electrophoretic mobility (EPM) measurements titrated against pH for SLGO, quartz sand grains (surface-associated colloidal material), and iron oxide coated sand grains (surface-associated colloidal material) suspended in an electrolyte solution exhibiting an ionic strength of 10 mM and 50 mM.

ionic strength. For example, the iron oxide coated sand colloids exposed to electrolyte solutions of 10 mM and 50 mM ionic strength exhibited an EPM of greater than  $+2.0 \mu\text{m cm V}^{-1} \text{s}^{-1}$  between pH 5.6 and pH 5.7, respectively, with each reaching their point-of-zero-charge ( $\text{pH}_{\text{zpc}}$ ) above approximately 8.3. Similar to colloidal quartz sand, increases in pH lead to deprotonation of the hydroxyl edge site functional groups at the iron oxide surface (Davis and Leckie, 1978), thereby resulting in fewer positively charged sites.

#### 4.4.4 Column Transport Studies

We conducted a series of column transport experiments that investigated the mobility of SLGO nanosheets through porous quartz sand iron oxide coated sand media in systems exhibiting environmentally-relevant pH and ionic strength conditions. The breakthrough curves representing the results of these experiments, in relation to breakthrough of the conservative NaBr tracer controls, are illustrated in Figure 4.5. On each panel of Figure 4.5, we indicate several important features of the transport experiments, including the timing of continuous flow from the SLGO suspension and the breakthrough concentration used in Equation 4.2. In addition, at 62.5 pore volumes, we switch the flow entering each column from the SLGO nanosheet suspension to a solution exhibiting the same pH and ionic strength conditions and we see a precipitous decline in effluent SLGO concentrations with little tailing. This observation supports our assumption of irreversible sorption of SLGO nanosheets to the collector grains throughout our experimental conditions, allowing us to utilize the initial deposition rate coefficient as our primary metric.

While the pH of the SLGO-bearing solutions was controlled ( $\pm 0.1$  s.u.) at pH = 5.6, 7.0, and 8.3 prior to entering the column, these systems were largely unbuffered against changes in pH caused by the solutions moving toward equilibrium with the respective mineral coating. As a result, we consistently monitored the pH in the effluent of the column and observed the largest change in pre- and post-column pH occurred in high pH systems, particularly those exposed to the iron oxide coated sands. Hence, the pH environment within a given column is likely characterized by a gradient from the recorded influent pH to the recorded effluent pH as a function of travel distance. In order

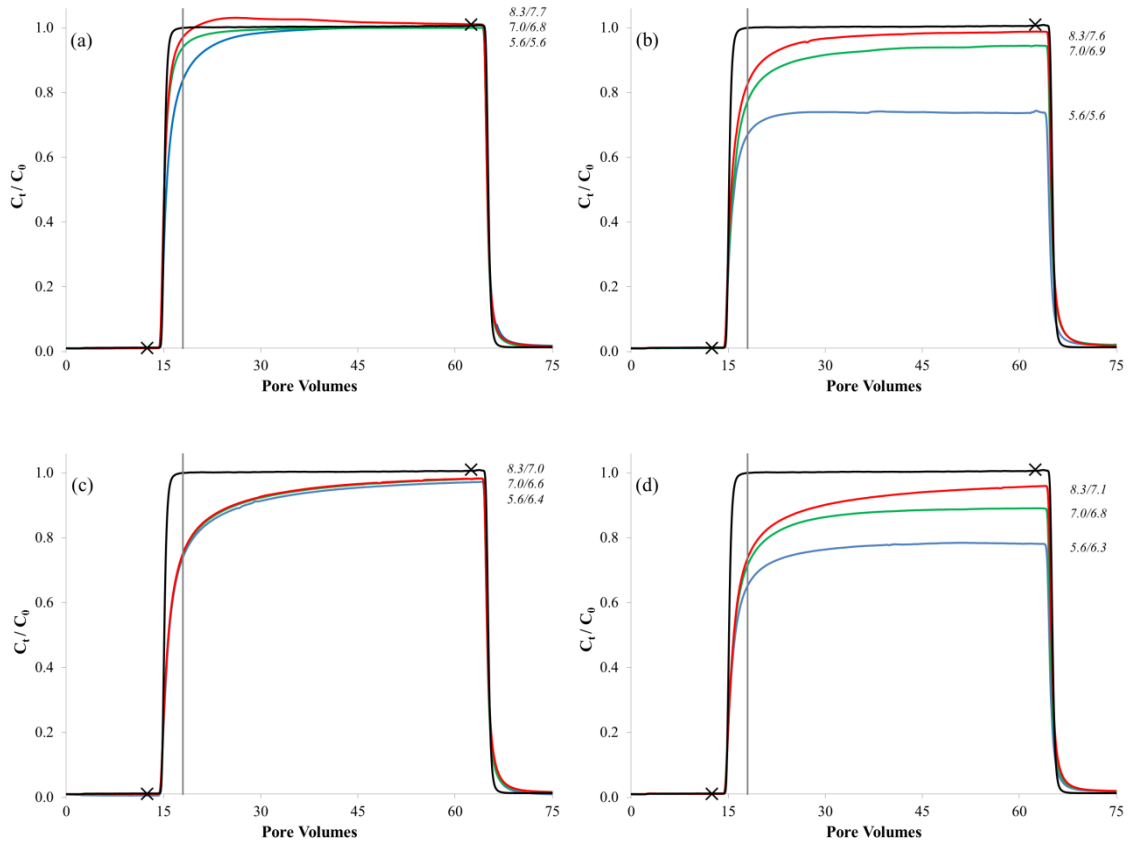


Figure 4.5: Breakthrough curves for (a) quartz sand columns, 10 mM ionic strength; (b) quartz sand columns, 50 mM ionic strength; (c) iron oxide coated sand columns, 10 mM, ionic strength; (d) iron oxide coated sand columns, 50 mM ionic strength. On all figures, red, green, and blue curves represent the average breakthrough curves for treatments with an influent pH of 8.3, 7.0, and 5.6, respectively. The black curve in each figure is the average breakthrough curve for the conservative NaBr tracer solution transported through quartz sand. pH values to the right of the breakthrough curves follow the convention *Influent pH/Effluent pH*. Continuous flow of the SLGO suspension occurred between 12.5 and 62.5 pore volumes (marked with black 'x's), with a pH-matched SLGO-free ionic strength buffer solution flowing through the column at all other times. Not shown on these figures is a 12.5 pore volume rinse with ultrapure water, which preceded each transport experiment. A horizontal grey line is placed at 18 pore volumes, where we measured the clean-bed breakthrough concentrations.

to accurately represent this potential range of pH conditions within a column, Figure 4.5 presents both the average influent and effluent pH values recorded for replicates from each treatment.

For most of our experimental treatments, the normalized concentrations illustrated by these breakthrough curves never plateau at a steady state value following the initial dispersive region of the curve, but rather slowly increase with time throughout the experiment. The shapes of these breakthrough curves are characteristic of systems where the initial retention of SLGO nanosheets within the column serves to block subsequent nanosheets from interacting with the collector (Ryan and Elimelech, 1996). The resulting magnitude of this effect on deposition rates is not necessarily proportional to the number of sites blocked, as each adsorbed nanosheet will effectively extend the influence of the collector (Song and Elimelech, 1993), based on its size, shape, and electric double layer properties. Overall, adsorbed nanosheets reduce the rate of subsequent nanosheet deposition and contribute to the eluting of more nanosheets over the course of the experiment. This phenomenon requires that we designate a clean-bed breakthrough concentration for the calculation of an *initial* deposition rate  $k_d$ . Here, we define the clean-bed breakthrough concentration as the  $C_t / C_0$  value observed at 5.5 pore volumes after turning on flow to the nanosheet suspension (or 18 total pore volumes from the start of the experiment), as indicated on Figure 4.5. The calculated  $k_d$  values are presented on Figure 4.6 against the pH observed in the effluent of the treatment columns.

SLGO nanosheets in quartz sand treatments at high ionic strength (50 mM) were deposited to a much greater extent than those at low ionic strength, with pH playing a

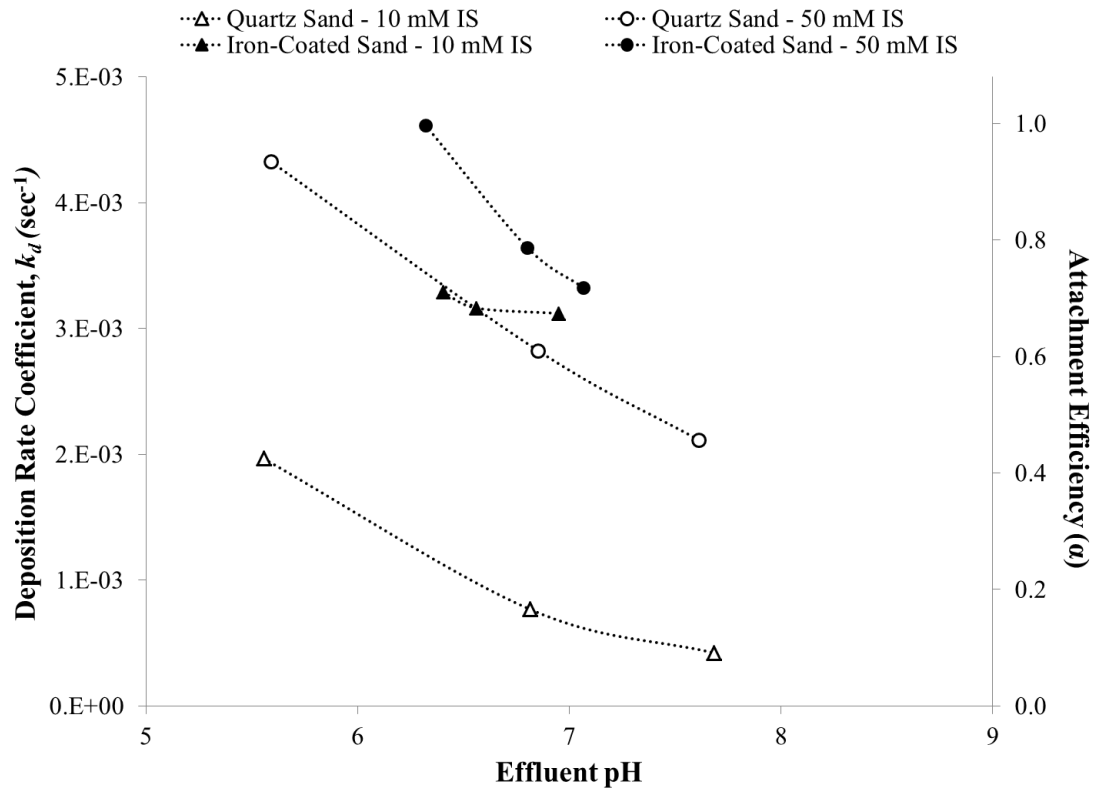


Figure 4.6: Deposition rate coefficients ( $k_d$ ) and attachment efficiencies ( $\alpha$ ) for SLGO nanosheets transported through columns packed with quartz sand and iron oxide coated sand in the pH and ionic strength conditions noted. All  $k_d$  values were calculated from the breakthrough concentrations presented in Figure 4.5 and are plotted against the average effluent pH values recorded for replicates from each treatment.

pronounced role in these systems. For example,  $k_d$  values for the high, middle, and low pH systems at high ionic strength were  $2.1 \times 10^{-3}$ ,  $2.8 \times 10^{-3}$ , and  $4.3 \times 10^{-3} \text{ s}^{-1}$ , respectively, with attachment efficiencies of up to 90% at the lowest pH (Figure 4.6). Given the similarity between the SLGO and the NaBr breakthrough curves in the low ionic strength systems containing quartz sand (Figure 4.5a), we conclude that relatively few SLGO nanosheets were deposited under these treatment conditions. However,

similar to the high ionic strength systems, the SLGO transport behavior at low ionic strength was measureable influenced by pH, with  $k_d$  values of  $0.4 \times 10^{-3}$ ,  $0.8 \times 10^{-3}$ , and  $2.0 \times 10^{-3} \text{ s}^{-1}$  for the high, middle, and low pH systems, respectively. Previous research using a similar methodology and quartz sand collectors has indicated  $k_d$  values that are three to four times lower for fullerenes (Tong et al., 2010) and approximately ten times higher for carboxyl functionalized single-walled carbon nanotubes (Jaisi et al., 2008) in 10 mM ionic strength systems at pH values of 6.8 to 7.0. Hence, the transport of graphitic materials could follow a gradient based on physical dimension, where fullerenes are deposited very little due to their spherical shape and carbon nanotubes are deposited to a much greater extent due to their very long and/or bundled morphology, which could promote physical straining (Jaisi et al., 2008). In this gradient, SLGO nanosheet transport represents an intermediate condition, as they are generally much shorter than carbon nanotubes, which may limit their deposition due to straining or other physical phenomenon, but their plate-like morphology encourages enhanced deposition, relative to spherical fullerenes. However, it is important to note that differences in experimental conditions, such as flow rates and surfaces properties, can strongly influence transport parameters and limit direct comparison of individual studies. Internally consistent studies for graphitic material transport are needed to validate this proposed relationship between fullerene, SLGO, and carbon nanotube deposition rates.

In the low ionic strength quartz treatments, the breakthrough curve for SLGO nanosheets exposed to the highest pH illustrates a small increase in SLGO concentration arriving at the detector, relative to the influent SLGO concentration [i.e.,  $C_t / C_0 > 1.0$  (up to  $\sim 1.02$ ) from  $\sim 8$  pore volumes through the end of the SLGO transport period]. While

this observation could have resulted from minor instrumental/analytical errors, it is reproducible (Appendix E) and may suggest that a phenomenon analogous to anion exclusion is present in these systems. Under this scenario, due to the highly negative charges on both the mobile SLGO nanosheets and the stationary quartz sand mineral grains, electrostatic repulsion drives the SLGO through the column at a rate faster than advective transport would suggest. However, this increase in transport rate should be accompanied by an earlier arrival at the detector, relative to the conservative tracer, which we do not observe in this treatment. Hence, we propose that the deviation from a typical anion exclusion behavior that we see in this treatment may be caused by the gradient in pH in our columns from the influent to the effluent pH (Figure 4.5), where exclusion occurs at the front of the column and some small degree of deposition occurs at the end of the column (due to the decreasing pH). This scenario would result in a build-up of nanosheets downstream in the column but not earlier arrival at the detector. Additional elucidation of this phenomenon will require further experimentation.

Due to the strong influence of surface mineralogy on the pH of the unbuffered SLGO nanosheet suspensions passed through columns packed with iron oxide coated sands, we were only capable of evaluating the transport behavior of SLGO nanosheets through a restricted pH range (effluent pH values of 6.4 to 7.0 and 6.3 to 7.1 for the 10 mM and 50 mM ionic strength treatments, respectively). Breakthrough curves for each of the low ionic strength iron oxide coated sand treatments approximately overlapped (Figure 4.5c), translating to a small range of  $k_d$  values of between  $3.1 \times 10^{-3}$  and  $3.3 \times 10^{-3} \text{ sec}^{-1}$ , which is due in part to the limited effluent pH range evaluated. However, at higher ionic strength, SLGO nanosheets in the iron oxide coated sand treatments

exhibited decreased deposition and increased breakthrough concentrations with increasing pH. In fact, this treatment resulted in the highest  $k_d$  values for a given effluent pH ( $3.3 \times 10^{-3}$ ,  $3.7 \times 10^{-3}$ , and  $4.6 \times 10^{-3} \text{ sec}^{-1}$  for the effluent pH values of 7.1, 6.8, and 6.3, respectively).

#### 4.4.5 Physical and Electrochemical Mechanisms Associated with Transport Behaviors

Figure 4.5 and Figure 4.6 illustrate several important trends in the transport behavior of SLGO nanosheets with respect to pH, ionic strength, and mineral coating. First, the larger deposition rates for SLGO nanosheets in columns containing quartz sand at high ionic strength, relative to those in low ionic strength treatments, is in qualitative agreement with the interactions predicted by Derjaguin-Landau-Verwey-Overbeek (DLVO) theory. The increase in ionic strength results in an increase in the concentration of counter-ions at the surface, a consequent compression of the electric double layer for both the SLGO nanosheets and quartz sand collector, and a reduction in the repulsive energy barrier that would otherwise limit nanosheet deposition. In addition, systems at relatively low pH are characterized by higher deposition rates because more surface-associated functional groups on the nanosheet and quartz sand collector surfaces are protonated causing each surface to be less negatively-charged, thereby reducing their repulsive forces. Evidence for these trends is also illustrated by the EPM values depicted in Figure 4.4, which indicates that both the SLGO nanosheets and quartz sand collector are more negatively-charged at high pH and low ionic strengths, which favors lower  $k_d$  values.

The transport behavior of SLGO nanosheets in iron oxide coated sand columns at low ionic strength can also be explained by the relative electrokinetic properties of the

nanosheets and collector grains. In this case, the iron oxide coated sand is positively charged throughout the effluent pH range, which favors significant deposition of the negatively-charged SLGO nanosheets. Indeed, over a similar pH range,  $k_d$  values for the low ionic strength iron oxide coated sand treatment are over 4 times higher than those of the low ionic strength quartz sand treatments. Without electrostatic repulsion to overcome, pH has only a minor influence on deposition in these systems, as the surfaces remain oppositely-charged throughout the pH range evaluated. In addition, Figure 4.4 indicates that the relatively small decrease in the positive charge associated with the iron oxide coating resulting from increases in pH are approximately compensated by the increasing negative charge on the SLGO nanosheets with increasing pH.

Unlike the experimental treatments discussed above, the transport behavior of the high ionic strength iron oxide coated sand treatments cannot be explained by electrochemical interactions alone. Oppositely-charged surfaces typically respond to increases in ionic strength by decreasing their interaction, because their respective surface charges are effectively shielded by the presence of increasing concentrations of counter-ions. An alternative perspective on this phenomenon would suggest that the electric double layer of a surface in a low ionic strength system is thicker and extends to a greater distance into the surrounding solution, increasing the likelihood of attracting an oppositely charged particle. However, in our systems containing iron oxide coated sands we observe that an increase in ionic strength from 10 mM to 50 mM increases the interaction between the oppositely charged SLGO nanosheets and iron oxide sand collector, leading to an increase in deposition rates. The increase in deposition with increasing ionic strength occurs despite the small decreases in positive and negative

charges for the collector and SLGO nanosheets, respectively, relative to the low ionic strength treatments (Figure 4.4).

We propose that the unanticipated behavior observed in the 50 mM ionic strength iron oxide coated sand treatment can be explained by aggregation of the SLGO nanosheets. For the same reason that SLGO-quartz sand interactions increase with increasing ionic strength, compression of the electric double layer also can induce nanosheet-nanosheet aggregation. In fact, Chowdhury et al. (2013) determined that the critical coagulation concentration of SLGO nanosheets is approximately 44 mM NaCl at pH 5.5, but observed no aggregation of SLGO nanosheets at NaCl concentrations lower than 20 mM. Aggregation could result in enhanced deposition of SLGO nanosheets in the 50 mM ionic strength treatments in two ways. First, in systems containing aggregated nanosheets, each successful nanosheet-collector attachment would remove a greater number of individual nanosheets from solution, relative to unaggregated systems. Second, depending on their size, nanosheet aggregates would likely be more prone to physical filtration mechanisms, whereby the larger particles become lodged in confined pore spaces. While Chowdhury et al. (2013) only evaluated nanosheet stability at pH 5.5, we would anticipate that the extent of aggregation in a solution at constant ionic strength would decrease with increasing pH, as nanosheets become more negatively charged and repulsive. Hence, the anticipated impact of aggregation on SLGO deposition rates would also decrease with increasing pH, as observed in our systems (Figure 4.6).

Although the transport behavior in high ionic strength treatments containing quartz sand collectors can be explained by electrochemical interactions alone, the aggregation of SLGO nanosheets may influence deposition in these systems as well. It is

important to point out that we saw no impact of ionic strength or pH on the initial UV-vis absorbance of the pre-column SLGO nanosheet suspension utilized for the transport studies. Hence, if nanosheet systems were aggregating in response to increases in ionic strength, we do not anticipate that this compromised our experimental methodology. However, we do note that the low pH, high ionic strength iron oxide coated sand treatment did serve as the  $k_{d, fav}$  parameter for our calculation of attachment efficiencies (Equation 4.4), and the presence of physical filtration mechanisms due to aggregation in this system may influence all associated  $\alpha$  values. Still, the calculated  $k_d$  values for each experimental treatment are based on discrete measurements of SLGO nanosheet transport and not subject to the same analytical limitation as the  $\alpha$  values, and are therefore a preferable metric.

#### 4.5 Conclusions

This study evaluated the mobility of SLGO nanosheets through two types of saturated porous media (quartz and iron oxide coated sand) and a variety of environmentally-relevant pH (5.6 to 8.3) and ionic strengths (10 mM and 50 mM) conditions. We observed that calculated initial deposition rate coefficients increased in systems containing iron oxide coated sand, relative to those containing quartz sand. Within each mineral-bearing system, deposition rate coefficients increased with decreases in pH and with increases in ionic strength. In general, solution pH and ionic strength controlled the near-surface charge (which we measured using electrophoretic mobility) on both the SLGO nanosheets and collector grains, which in turn, determined the extent to which SLGO nanosheets were deposited in the matrix. However, in our high ionic

strength systems, which exhibit ionic strength values that are higher than the critical coagulation concentration for SLGO nanosheets, aggregation may also influence SLGO deposition. The deposition rate coefficients for SLGO nanosheets calculated in this study are higher than those from similar studies of spherical fullerenes, but much lower than those for carboxyl-functionalized single-walled carbon nanotubes, which may indicate that physical dimension may influence the deposition of graphitic materials in environmental systems. In addition, because our porous sand systems are relatively homogenous, when compared to real environmental systems, with respect to collector grain sizes, pore geometries, and soil mineralogy, we suggest that the deposition rates presented herein likely overestimate the expected mobility of SLGO nanosheets in actual subsurface environments. Collectively, our results illustrate the importance of understanding the influence of electrochemical parameters and mineralogy on mobility of engineered nanomaterials through the subsurface.

#### 4.6 Acknowledgments

This research was supported, in part, by a fellowship to T.D. from the Arthur J. Schmitt Foundation. In addition, we performed most experiments and analyses using instrumentation at the Center for Environmental Science and Technology (University of Notre Dame). I also acknowledge a substantial technical contribution by Jennifer Szymanowski.

## CHAPTER 5: CONCLUSIONS

The demand for materials that can aid in the remediation of contaminated lands is likely to increase dramatically over the coming decades. The combination of enhanced regulatory structures, public sentiments, and urban expansion into former industrial zones will require that areas once labeled as *toxic* become useable again. However, prudence will dictate that we carefully verify that remediated lands are indeed safe for human habitation, not simply in the short-term, but for future generations as well. Hence, as geochemists, environmental engineers, and hydrologists, we must strive to learn as much as possible about the physical and chemical properties of the materials we deploy in remediation applications. Important characteristics, particularly for material sorbents, may include their capacity to sequester a contaminant from the aqueous phase, the environmental conditions that may promote the re-release of a sorbed contaminant, the competitive interactions between a contaminant and other environmental components at the surface of a material, and mobility of the sorbent through the subsurface.

In recent years, numerous studies have highlighted the remarkable capacity of graphene oxide (GO) to sorb a variety of chemical contaminants from aqueous solutions. In fact, for many contaminants, including several metals, GO exhibits a larger maximum sorption capacity than any other known material. As a result, the potential applications for GO in remediation systems may be unparalleled. Yet, although researchers have been

examining oxidized graphitic materials for over 150 years, much remains unknown about GO, including many of the important properties discussed above.

Hence, the goal of this dissertation was to characterize the extraordinary properties of GO and to conduct tailored experiments that address its capacity to sorb metals and measure its transport properties in order to better inform remediation strategies that employ GO as a sorbent. In Chapter 2 and Chapter 3, we explored the capacity of multi-layered GO (MLGO) particles to sorb Cd, Pb, and U, which are important components of many contaminated environments. For each metal, potentiometric titrations and batch metal sorption experiments were utilized to constrain MLGO site concentrations, the acidity constants for each of four MLGO surface sites, and stability constants for important metal-MLGO surface complexes. By using a surface complexation modeling approach, rather than the more common Langmuir/Freundlich isotherms, the resulting *intrinsic* parameters can be utilized to model the sorption behavior of MLGO in a wide variety of environmentally-relevant water chemistries.

Through these studies, we determined that MLGO particles exhibit a strong solution buffering capacity across a wide range of pH values, and that the capacity to sorb protons was not strongly influenced by ionic strength. However, our sorption measurements in Chapter 2 indicated that the ionic strength of the solution dramatically impacts Cd- and Pb-MLGO interactions. After two electrostatic surface complexation models failed to properly represent this difference in sorption behaviors, we instead developed a 4-site non-electrostatic model that accounts for ionic strength effects as a competition between Na and Cd or Pb for available MLGO sorption sites. This model

provides a reasonable fit to the potentiometric titration and metal sorption data and illustrates that the remediation of Cd and Pb using MLGO in environments exhibiting high electrolyte concentrations may be challenging. In marked contrast to these other metals, the U sorption measurements in Chapter 3 indicate that U-MLGO interactions are independent of ionic strength. In addition, MLGO particles can sorb multiple aqueous uranyl complexes, maintaining a very high level of sorption through pH 9.5. Both of these characteristics are likely due to the very high affinity demonstrated by MLGO particles for aqueous uranyl complexes, and demonstrate that MLGO could be particularly useful for the remediation in high-ionic strength, high-pH environments where U is typically poorly sorbed by other materials.

Having documented the extensive ability of GO materials to sorb metals, we then investigated the mobility of single-layered GO (SLGO) nanosheets through two different types of porous media (Chapter 4). The significant mobility of a sorbent through a soil or groundwater matrix can be harnessed to capture and remove contaminants in carefully-controlled engineered systems, but can also facilitate uncontrolled or detrimental movement of contaminants through environmental systems. Conversely, sorbents that strongly bind contaminants and exhibit limited mobility serve to fix contaminants *in situ*. Hence, the mobility of an engineered sorbent is an important factor in determine how best to deploy it in a remediation system.

Our measurements of deposition rate coefficients from Chapter 4 illustrate that pH, ionic strength, and soil mineralogy will all play critical roles in determining the mobility of SLGO nanosheets through the subsurface. The transport behaviors of SLGO nanosheets through quartz and iron oxide coated sand matrices could generally be

explained by the relative near-surface charges exhibited by the nanosheet and the sand grains, which we determined through electrophoretic mobility measurements. We observed high degrees of SLGO mobility in treatments containing quartz sand, particularly in high pH and low ionic strength environments, where both the SLGO nanosheets and quartz sand grains are negatively-charged. SLGO nanosheets were deposited in the columns packed with iron oxide coated sands to a much greater extent due to the attraction between the negatively-charged nanosheets and the positively-charged iron oxide coating. However, we did measure some deposition rate coefficients that could not be explained by the electrochemical surface properties alone and likely indicate that aggregation of SLGO nanosheets in high ionic strength environments may increase SLGO deposition. Collectively, these findings illustrate the importance of characterizing the environmental characteristics and mineralogy at a contaminated site, as these properties can significantly influence the mobility of a sorbent.

In most cases, a successful experiment will raise more questions than it answers, which is certainly true for the experiments described in this dissertation. Perhaps better than most other studies, the sorption experiments in Chapter 2 and Chapter 3 illustrate the importance of supporting surface complexation modeling with spectroscopic studies. Surface complexation models are fraught with assumptions, such as metal-to-surface site stoichiometries and the identities of sorbing metal species. For example, we assumed in our models a 1:1 stoichiometry for Cd-, Pb-, and U-MLGO interactions and incorporated only sorption reactions with the abundant metal species present in MLGO-free speciation modeling for a given pH range. We validated as many assumptions as possible by trying to ensure that the model we were proposing provided us with the best fit to the

experimental data. However, we often observed similar model fits using different assumptions, such as the nearly identical SSR values related to the metal sorption modeling in Chapter 2 using different surface site combinations. At the time of this writing, we have prepared and partially analyzed samples using X-ray absorption spectroscopy (XAS) at the Advanced Photon Source in Argonne National Laboratory (USA). We anticipate that the results of the studies will provide insights regarding reaction stoichiometries, local binding environments, the predominance of inner and outer sphere surface complexes for various pH and ionic strength conditions, and perhaps, the chemical identities for MLGO surface functional groups and the aqueous complexes being sorbed (especially for Pb and U systems). This information will then allow us to build more robust models that provide increasingly-accurate predictions of MLGO sorption behaviors.

In addition, the model for Cd and Pb sorption presented in Chapter 2 is a relatively novel approach that accounts for ionic strength effects by invoking an interaction between MLGO surface sites and Na from the background electrolyte. We currently do not have any independent validation regarding the extent to which these reactions occur, and only limited insights (based on the model fitting) regarding the potential affinity of MLGO surface sites for Na. In addition, although we applied the presumed Na-MLGO interaction uniformly amongst all surface sites, there is a possibility that each discrete site type on the MLGO surface exhibits a different affinity for Na. Our experimental design did not allow us to constrain the  $\text{Log } K_{ads}$  for any of these potential reactions. Thus, in order to validate our proposed model, we would need well-constrained Na sorption experiments conducted in an indifferent background electrolyte

or as a function of background electrolyte concentration. Then using surface complexation modeling, we could establish a value for the stability constant that describes the Na-MLGO interaction.

Finally, in Chapter 4, we characterized the transport of SLGO nanosheets through quartz and iron oxide coated sands. While these two different collectors resulted in very different transport behaviors, these laboratory-based column studies do not replicate the complexity of natural soil and groundwater environments. Most real subsurface environments are significantly heterogeneous with respect to soil mineralogy, grain size, pore geometry, and pore interconnectivity, and contain significant concentrations of dissolved organic material. Hence, our simplified systems are only the first step in establishing the mobility of SLGO nanosheets in more complex environments. Additional, progressively-complex studies could include transport experiments using SLGO nanosheets exposed to fulvic or humic acids and/or columns packed with varying sand grain sizes or actual soil cores. In addition, investigating the transport of MLGO particles could provide insights regarding the influence of GO dimensions on overall transport behaviors.

The experimental results reported in this dissertation provided the necessary input to develop models that constrained important sorption and transport parameters. These parameters will be of significant value to those engaged in applying GO in remediation designs. However, as GO becomes more prevalent in consumer and industrial productions, there is a strong likelihood for undesirable and/or uncontrolled environmental release, and our research can assist in determining the potential environmental impacts associated with these releases as well. Collectively, our studies

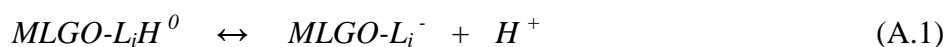
show that GO nanosheets have the potential to dramatically influence their surrounding environments and enriching our understanding of these material will allow us to harnessing their amazing properties to benefit human and environmental health.

APPENDIX A:  
ADDITIONAL DETAILS REGARDING SURFACE COMPLEXATION MODELING

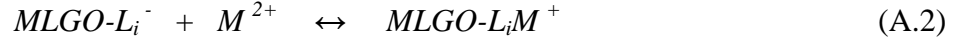
The following discussion provides additional details regarding background, approach, and application of the surface complexation models utilized in Chapter 2 of this dissertation.

### A.1 Chemical Equilibrium Modeling

The chemical equilibrium modeling associated with both potentiometric titrations and batch metal sorption was conducted using FITEQL 2.0 (Westall, 1982). We evaluated several different modeling approaches to account for the observed sorption behaviors, including a non-electrostatic model (NEM), a constant capacitance model (CCM), and a diffuse layer model (DLM). As will be seen, these models significantly differ in their assumptions regarding electrostatic effects at the multi-layer graphene oxide (GO) particle surface, but use the same basic approach to describe the interactions between the protons or metals and the MLGO surface. From the discussion in Chapter 2, we assume a 1:1 stoichiometry between MLGO surface sites and the target adsorbate, representing complexation reactions with protons ( $H^+$ ) and metals ( $M^{2+}$ ) using:



and



where  $L_i$  is assumed to be a discrete surface functional group type responsible for proton sorption and  $MLGO-$  represents the remainder of the MLGO particle to which the functional group is attached. In each model, FITEQL uses the measured extents of proton and metal sorption to constrain acidity constants ( $K_a$ ) for Reaction A.1 and metal-surface stability constants ( $K_{ads}$ ) for Reaction A.2. Respectively, these equilibrium constants are given by the following equations:

$$K_{a(i)} = \frac{[GO-L_i^-] * a_{H^+}}{[GO-L_iH^0]} e^{F\psi/RT} \quad (A.3)$$

and

$$K_{ads(i)} = \frac{[GO-L_iM^+]}{[GO-L_i^-] * a_{M^{2+}}} e^{F\psi/RT} \quad (A.4)$$

where  $\psi$  is the electrostatic potential,  $F$  is the faraday constant,  $R$  is the ideal gas constant,  $T$  is the temperature, brackets represent the molal concentration of surface species, and  $a_x$  represents the activity of the species in the associated subscript. FITEQL uses the Davies equation to calculate activity coefficients for aqueous ions.

Equation A.3 and Equation A.4 are comprised of two distinct terms: (1) a thermodynamic term (the first term on the right side of the equation), which measures the chemical affinity between the protons or metal ions and the MLGO particle surface sites; and (2) an electrostatic term (the second term on the right side of the equations, denoted as  $e^{F\psi/RT}$ ), which represents the energy needed to allow a charged species to approach a charged surface (Marmier et al., 1999). The NEM, the CCM, and the DLM each differ significantly in their treatment of the electrostatic term. For the NEM, the electrostatic term is set equal to 1, thereby indicating that electrostatic interactions do not significantly affect the sorption of a dissolved solute to a surface. The electrostatic term is therefore omitted from the Equation 2.3 and Equation 2.6 in Chapter 2. In the CCM, surface charge density ( $\sigma$ ) is a function of  $\psi$  and the Helmholtz capacitance ( $C$ ) as in the following relationship:

$$\sigma = C\psi \tag{A.5}$$

In the CCM of the potentiometric titration data, we iteratively varied the value of  $C$  to optimize the goodness-of-fit value  $V(Y)$  (discussed in Chapter 2) for each treatment replicate. This optimization process resulted in an average value of  $C$  for each ionic strength treatment that we then used in the CCM to establish  $pK_a$  values for each ionic strength treatment. For the DLM,  $\sigma$  and  $\psi$  are related through the following expression:

$$\sigma = 0.117 \sqrt{I} \sinh \frac{zF\psi}{RT} \tag{A.6}$$

where  $I$  is the ionic strength and  $z$  is the cation charge.

In order to solve for the acidity and metal-stability constants, additional inputs are required, including the pH for a given sorption measurement and the known equilibrium constants for the aqueous complexation reactions occurring in each system (Table B.1). Complexation between  $\text{ClO}_4^-$  and aqueous metals in the experimental system was assumed to be negligible. Our surface area measurements via the  $\text{N}_2$ -Brunauer, Emmett, and Teller (BET) method proved unreliable, consistent with the findings of other researchers (Szabó et al., 2006b). Hence, MLGO surface area input for the CCM and DLM was estimated at  $1807 \text{ m}^2 \text{ g}^{-1}$ , as calculated by Szabó et al. (2006b) using elemental composition and the size and weight of the repeating unit cells. The utilization of this surface area value assumes that protons and metals have access functional groups residing within the MLGO laminations. We show evidence to support this assumption in Chapter 2.

Applying this modeling exercise to the potentiometric titration data ultimately results in both  $\text{pK}_a$  values and individual site concentrations for each of the discrete types of functional groups present on the MLGO surface and active in the pH range of this study. Because different functional groups have distinct  $\text{pK}_a$  values, metal sorption measurements conducted as a function of pH place constraints on which sites are involved in the sorption reactions and the surface complexation modeling of these data can then be used to constrain the  $K_{ads}$  values for each important metal-MLGO sorption reaction. We are ultimately attempting to determine which of these models best accounts for the sorption behavior throughout our experimental range of pH and ionic strength. We evaluate the success of a model via its visual fit to the experimental data and its

goodness-of-fit or variance value  $V(Y)$ , which we obtain from the FITEQL model output. In addition, a successful model would yield calculated equilibrium constants ( $pK_a$  and  $K_{ads}$ ) from the experimental data that do not show a trend in value with changing ionic strengths. Consistency in these equilibrium constants would indicate that the model alone adequately accounts for the electrostatic effects occurring at the MLGO surface and these singular values for  $pK_a$  or  $K_{ads}$  could be utilized to model the sorption of protons and metals, respectively, throughout a range of environmental conditions.

## A.2 Electrostatic Modeling of the Potentiometric Titration Data

Regardless of the ionic strength of the electrolyte buffer, the MLGO particle suspensions provide substantial solution buffering capacity over a wide range of pH values, suggesting that multiple discrete surface sites are proton-active. Hence, for each replicate from the four different ionic strength treatments, we attempted to fit the titration data between pH 3.0 and pH 10.0 (or pH 3.2 and pH 10.0 for the two lowest ionic strengths) using 1- to 5-site NEM, CCM, and DLM surface complexation models. Each site associated with these models is assumed to be a discrete surface functional group, although the presence of an ensemble of functional groups with chemically-indistinguishable proton sorption behaviors cannot be ruled out. Given the similarity between forward and reverse titrations, we only fit forward titration curves from individual replicates, and subsequently averaged the  $V(Y)$  values across all ionic strengths as an initial assessment of the goodness-of-fit for the different models.

The 5-site NEM and 3-, 4-, and 5-site CCMs and DLMs all consistently failed to converge for MLGO replicates in all ionic strengths, indicating that the observed

buffering behaviors cannot constrain the parameters for these numbers of individual sites. Of the surface complexation models that did successfully converge, four provided reasonable fits to the potentiometric titration data, and we have compiled the calculated average  $pK_a$  and site concentrations from these models for each ionic strength in Table A.1. The  $V(Y)$  values averaged across all ionic strength treatments for the 3- and 4-site NEM, the 2-site CCM, and the 2-site DLM were 2.82, 0.48, 1.40, and 2.21, respectively. For each replicate of a given ionic strength, fitted curves from each of these models were also in good visual agreement with the titration data.

While several models yielded approximately similar results, due to multiple observations from the model output, we propose that the 4-site NEM exhibits the best fit to the experimental MLGO potentiometric titration data across the range of pH and ionic strength conditions. For example, in the DLM, we observe a strong positive trend in each model parameter as a function of ionic strength, which suggests that the model fails to accurately capture the electrostatic properties of the MLGO surfaces. The 4-site NEM and the CCM do not exhibit similar trends. In addition, while the 4-site NEM and the CCM both exhibit a modest degree of variation between the modeling results from the various ionic strengths, the estimated error (presented as a standard deviation) for the NEM, both within a given ionic strength and after averaging between ionic strengths, is substantially smaller than for the CCM. The greater degrees of variation present in the CCM likely stems from the need for an accurate value of the Helmholtz capacitance ( $C$ ). We attempted to estimate the value of  $C$  for each dataset by iterative-adjusting its value until the  $V(Y)$  was optimized to 1, and then utilized this estimate as input for the CCM for each ionic strength. However, this procedure yielded a large range of values for  $C$ ,

TABLE A.1

SITE CONCENTRATIONS AND ACIDITY CONSTANTS FROM THE NON-ELECTROSTATIC AND ELECTROSTATIC SURFACE COMPLEXATION MODELING

3-Site NEM												
Ionic Strength	<i>C</i> (F/m <sup>2</sup> )	Site 1		Site 2		Site 3		Site 4		Total	V(Y)	
		[Site <sub>1</sub> ] (mol/g)	pKa <sub>1</sub>	[Site <sub>2</sub> ] (mol/g)	pKa <sub>2</sub>	[Site <sub>3</sub> ] (mol/g)	pKa <sub>3</sub>	[Site <sub>4</sub> ] (mol/g)	pKa <sub>4</sub>	[Site <sub>T</sub> ] (mol/g)		
1 mM	AVE	-	4.8E-04	5.34	4.8E-04	7.57	1.3E-03	9.65	-	-	2.2E-03	2.25
	SD	-	5.4E-05	0.53	4.0E-05	0.36	1.9E-04	0.18	-	-	2.4E-04	
10 mM	AVE	-	5.2E-04	4.74	5.8E-04	7.62	1.2E-03	9.41	-	-	2.3E-03	4.82
	SD	-	7.3E-05	0.49	8.4E-05	0.35	1.1E-04	0.19	-	-	1.8E-04	
100 mM	AVE	-	5.6E-04	5.18	7.2E-04	7.70	1.3E-03	9.41	-	-	2.6E-03	3.24
	SD	-	7.1E-05	0.23	1.8E-04	0.42	1.2E-04	0.28	-	-	2.8E-04	
300 mM	AVE	-	5.6E-04	5.65	8.0E-04	7.89	1.5E-03	9.61	-	-	2.8E-03	0.98
	SD	-	7.9E-05	0.14	1.1E-04	0.24	1.1E-04	0.10	-	-	2.1E-04	
Combined	AVE	-	5.3E-04	5.23	6.4E-04	7.70	1.3E-03	9.52	-	-	2.5E-03	2.82
	SD	-	3.6E-05	0.38	1.4E-04	0.14	1.3E-04	0.13	-	-	2.8E-04	

4-Site NEM												
Ionic Strength	<i>C</i> (F/m <sup>2</sup> )	Site 1		Site 2		Site 3		Site 4		Total	V(Y)	
		[Site <sub>1</sub> ] (mol/g)	pKa <sub>1</sub>	[Site <sub>2</sub> ] (mol/g)	pKa <sub>2</sub>	[Site <sub>3</sub> ] (mol/g)	pKa <sub>3</sub>	[Site <sub>4</sub> ] (mol/g)	pKa <sub>4</sub>	[Site <sub>T</sub> ] (mol/g)		
1 mM	AVE	-	3.3E-04	4.50	4.2E-04	6.42	4.7E-04	8.34	1.4E-03	9.97	2.6E-03	0.21
	SD	-	1.0E-04	0.48	2.2E-05	0.11	6.8E-05	0.11	2.4E-04	0.12	3.1E-04	
10 mM	AVE	-	7.1E-04	3.59	3.8E-04	6.05	7.0E-04	8.33	1.0E-03	9.75	2.8E-03	0.40
	SD	-	3.5E-04	0.55	4.0E-05	0.16	5.3E-05	0.06	7.8E-05	0.09	4.3E-04	
100 mM	AVE	-	3.9E-04	4.02	4.6E-04	6.09	7.6E-04	8.16	1.2E-03	9.62	2.9E-03	0.84
	SD	-	7.4E-05	0.28	7.2E-05	0.16	2.4E-04	0.30	1.4E-04	0.35	4.0E-04	
300 mM	AVE	-	4.0E-04	5.29	4.0E-04	6.73	7.2E-04	8.29	1.4E-03	9.76	3.0E-03	0.47
	SD	-	4.5E-05	0.13	8.7E-05	0.10	1.8E-04	0.04	1.6E-04	0.08	2.5E-04	
Combined	AVE	-	4.6E-04	4.35	4.2E-04	6.32	6.6E-04	8.28	1.3E-03	9.78	2.8E-03	0.48
	SD	-	1.7E-04	0.73	3.7E-05	0.32	1.3E-04	0.08	1.9E-04	0.14	1.5E-04	

TABLE A.1 (CONTINUED)

2-Site CCM												
Ionic Strength	C (F/m <sup>2</sup> )	Site 1		Site 2		Site 3		Site 4		Total	V(Y)	
		[Site <sub>1</sub> ] (mol/g)	pKa <sub>1</sub>	[Site <sub>2</sub> ] (mol/g)	pKa <sub>2</sub>	[Site <sub>3</sub> ] (mol/g)	pKa <sub>3</sub>	[Site <sub>4</sub> ] (mol/g)	pKa <sub>4</sub>	[Site <sub>T</sub> ] (mol/g)		
1 mM	AVE	1.08	6.7E-04	5.63	3.2E-03	8.67	-	-	-	-	3.9E-03	1.60
	SD	0.30	2.4E-05	0.28	1.9E-03	0.33	-	-	-	-	1.9E-03	
10 mM	AVE	0.88	6.3E-04	4.44	2.9E-03	7.84	-	-	-	-	3.5E-03	1.23
	SD	0.12	1.4E-04	0.50	7.9E-04	0.20	-	-	-	-	9.0E-04	
100 mM	AVE	1.09	6.4E-04	4.98	2.9E-03	7.89	-	-	-	-	3.6E-03	1.71
	SD	0.25	7.4E-05	0.12	6.9E-04	0.22	-	-	-	-	7.3E-04	
300 mM	AVE	1.41	7.1E-04	5.73	2.8E-03	8.31	-	-	-	-	3.5E-03	1.05
	SD	0.15	1.4E-04	0.12	6.5E-04	0.09	-	-	-	-	6.5E-04	
Combined	AVE	1.11	6.6E-04	5.20	3.0E-03	8.18	-	-	-	-	3.6E-03	1.40
	SD	0.22	3.6E-05	0.60	1.8E-04	0.39	-	-	-	-	1.8E-04	

2-Site DLM												
Ionic Strength	C (F/m <sup>2</sup> )	Site 1		Site 2		Site 3		Site 4		Total	V(Y)	
		[Site <sub>1</sub> ] (mol/g)	pKa <sub>1</sub>	[Site <sub>2</sub> ] (mol/g)	pKa <sub>2</sub>	[Site <sub>3</sub> ] (mol/g)	pKa <sub>3</sub>	[Site <sub>4</sub> ] (mol/g)	pKa <sub>4</sub>	[Site <sub>T</sub> ] (mol/g)		
1 mM	AVE	-	8.2E-04	3.79	2.0E-03	6.42	-	-	-	-	2.8E-03	1.03
	SD	-	3.3E-05	0.27	4.9E-04	0.22	-	-	-	-	5.0E-04	
10 mM	AVE	-	6.7E-04	4.10	1.7E-03	6.85	-	-	-	-	2.3E-03	2.72
	SD	-	9.4E-05	0.37	1.2E-04	0.11	-	-	-	-	1.8E-04	
100 mM	AVE	-	7.0E-04	5.06	1.9E-03	7.65	-	-	-	-	2.6E-03	2.77
	SD	-	9.2E-05	0.14	1.9E-04	0.15	-	-	-	-	2.4E-04	
300 mM	AVE	-	7.6E-04	5.83	2.1E-03	8.24	-	-	-	-	2.8E-03	2.30
	SD	-	1.4E-04	0.10	2.3E-04	0.07	-	-	-	-	2.0E-04	
Combined	AVE	-	7.4E-04	4.70	1.9E-03	7.29	-	-	-	-	2.7E-03	2.21
	SD	-	6.8E-05	0.93	1.7E-04	0.81	-	-	-	-	2.3E-04	

indicating that we may not yet have an accurate estimate for this value, thereby contributing to additional error in the CCM for which it is needed. While an independent and accurate estimate of the Helmholtz capacitance could improve the CCM results, with our existing understanding of these systems, the 4-site NEM provides the most robust model for the potentiometric titration results in these systems.

### A.3 Electrostatic Modeling of Batch Cd Sorption Modeling

Using the  $pK_a$  values and site concentrations calculated from the 2-site CCM for the potentiometric titration data, we utilized the measured extents of Cd sorption to constrain stability constants ( $K_{ads}$ ) values for the Cd-MLGO interaction. These efforts failed to result in a consistent value for  $K_{ads}$  across the range of ionic strength treatments (Table A.2). As a result, in Chapter 2, we devise a model that accounts for ionic strength effects as a competition between Na and Cd or Pb for available MLGO surface sites.

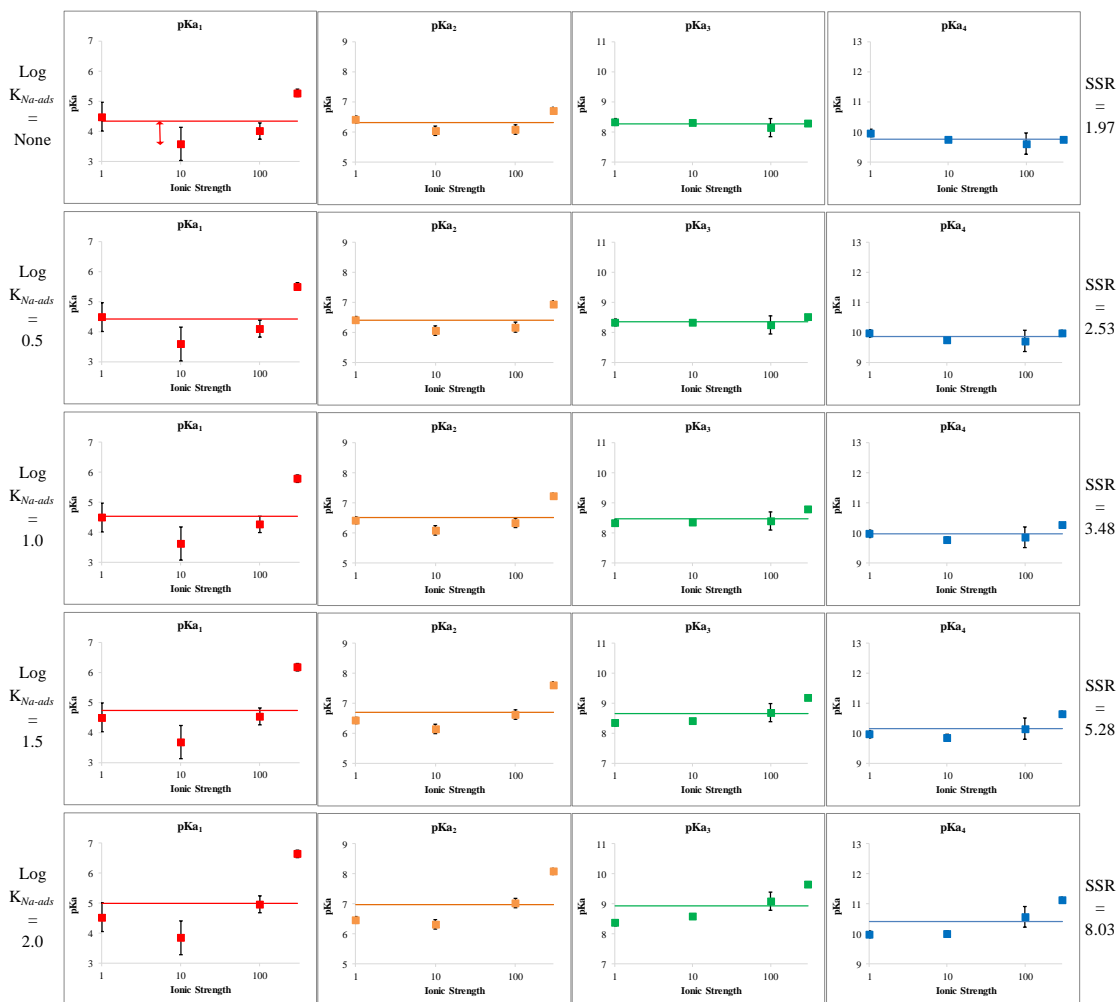
TABLE A.2

CD-MLGO STABILITY CONSTANTS CALCULATED FROM A CCM FOR EACH  
 IONIC STRENGTH TREATMENT

2-Site CCM		
Ionic Strength	Site 1	Error
	Log $K_{Cd-ads}$	V(Y)
1 mM	6.20	0.01
10 mM	5.72	0.35
100 mM	4.37	1.90
300 mM	3.80	1.79

APPENDIX B:  
ADDITIONAL FIGURES AND TABLES FOR CHAPTER 2

Figure B.1:  $pK_a$  values for each MLGO surface site calculated from models that incorporate Na-MLGO interactions with the indicated value of  $\text{Log } K_{Na-ads}$ . These  $pK_a$  values are plotted as a function of ionic strength. Each point is calculated as the average  $pK_a$  from the modeling of three to seven potentiometric titration replicates, with error bars indicating the standard deviations. Replicate data are provided in Table B.4. Horizontal lines indicate the average  $pK_a$  for a given surface site and  $\text{Log } K_{Na-ads}$  treatment across ionic strength (i.e., the average  $pK_a$  within a given panel). The arrow in the top-left panel provides an illustration of the measured distance between an individual  $pK_a$  value and value depicted by the horizontal line. We define this distance as the *residual*, and the sum of all squared residuals (SSR) for a given row is provided at the end of each row. We define a successful model as one that yields calculated  $pK_a$  values from the experimental data that do not vary as a function of ionic strength, and thus we use the SSR values as the metric by which we evaluate this goal.



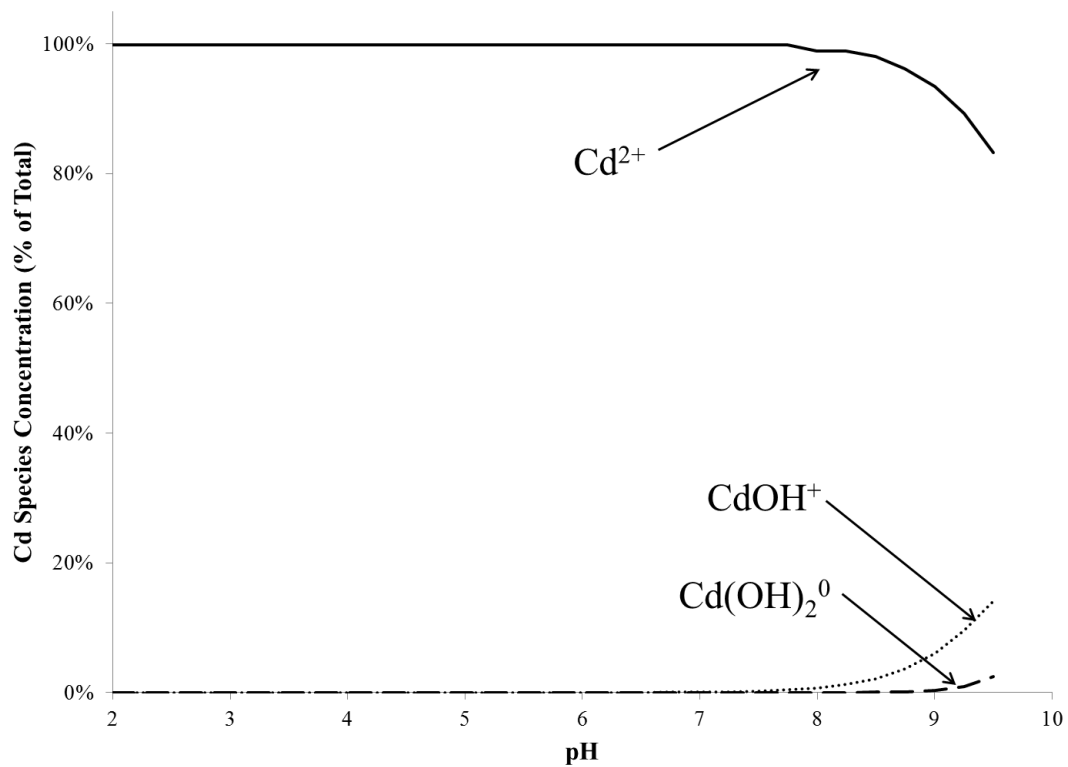


Figure B.2: Modeled Cd speciation as a function of pH for 100 mM ionic strength systems containing 1 ppm Cd. Speciation plots for all ionic strength solutions between 1 mM and 300 mM are virtually identical.

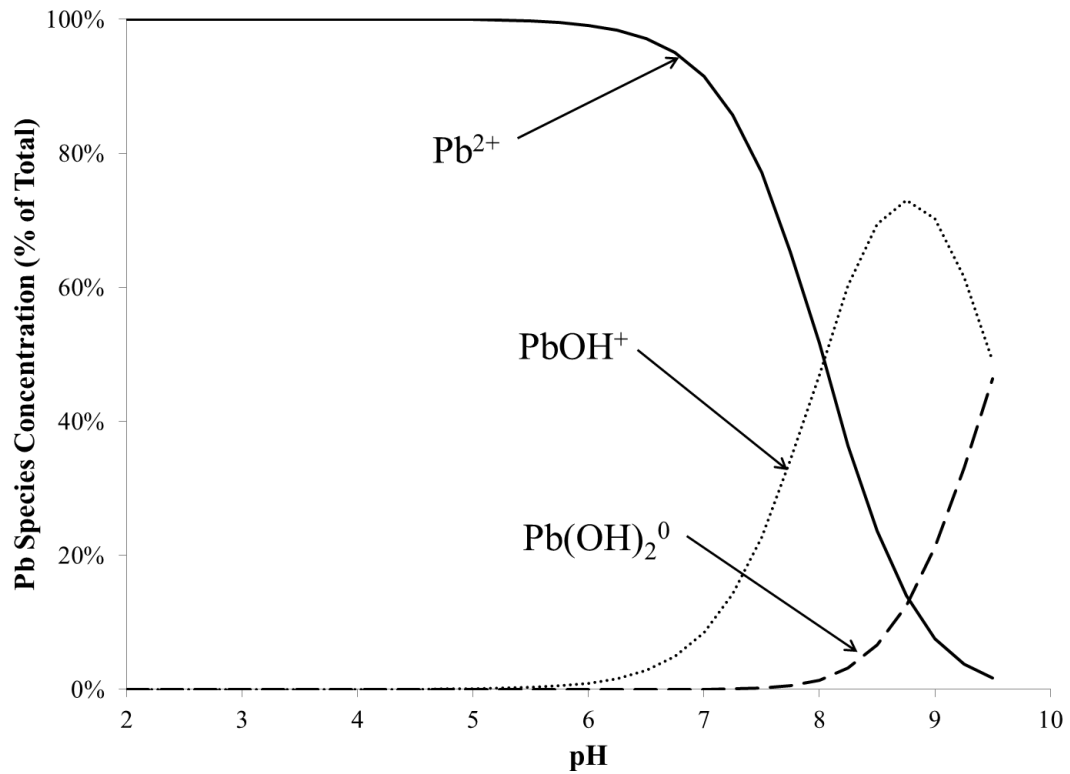


Figure B.3: Modeled Pb speciation as a function of pH for 100 mM ionic strength systems containing 1 ppm Pb. Speciation plots for all ionic strength solutions between 1 mM and 300 mM are virtually identical.

TABLE B.1

LOG K VALUES FOR CD AND PB AQUEOUS COMPLEXATION REACTIONS

UTILIZED IN FITEQL

Reaction	Log K
<i>General</i>	
$\text{H}_2\text{O} - \text{H}^+ \leftrightarrow \text{OH}^-$	-14.00
$\text{Na}^+ + \text{H}_2\text{O} - \text{H}^+ \leftrightarrow \text{NaOH}^0$	-14.18
$\text{H}_2\text{CO}_3^0 - \text{H}^+ \leftrightarrow \text{HCO}_3^-$	-6.35
$\text{H}_2\text{CO}_3^0 - 2\text{H}^+ \leftrightarrow \text{CO}_3^{2-}$	-16.67
<i>Pb - Aqueous Complexes</i>	
$\text{Pb}^{2+} + \text{H}_2\text{O} - \text{H}^+ \leftrightarrow \text{PbOH}^+$	-7.71
$\text{Pb}^{2+} + 2\text{H}_2\text{O} - 2\text{H}^+ \leftrightarrow \text{Pb(OH)}_2^0$	-17.12
$\text{Pb}^{2+} + 3\text{H}_2\text{O} - 3\text{H}^+ \leftrightarrow \text{Pb(OH)}_3^-$	-28.06
$2\text{Pb}^{2+} + \text{H}_2\text{O} - \text{H}^+ \leftrightarrow \text{Pb}_2(\text{OH})^{3+}$	-6.36
$3\text{Pb}^{2+} + 4\text{H}_2\text{O} - 4\text{H}^+ \leftrightarrow \text{Pb}_3(\text{OH})_4^{2+}$	-23.88
$4\text{Pb}^{2+} + 4\text{H}_2\text{O} - 4\text{H}^+ \leftrightarrow \text{Pb}_4(\text{OH})_4^{4+}$	-20.88
$6\text{Pb}^{2+} + 8\text{H}_2\text{O} - 8\text{H}^+ \leftrightarrow \text{Pb}_6(\text{OH})_8^{4+}$	-43.61
<i>Cd - Aqueous Complexes</i>	
$\text{Cd}^{2+} + \text{H}_2\text{O} - \text{H}^+ \leftrightarrow \text{CdOH}^+$	-10.10
$\text{Cd}^{2+} + 2\text{H}_2\text{O} - 2\text{H}^+ \leftrightarrow \text{Cd(OH)}_2^0$	-20.30
$\text{Cd}^{2+} + 3\text{H}_2\text{O} - 3\text{H}^+ \leftrightarrow \text{Cd(OH)}_3^-$	-31.70
$\text{Cd}^{2+} + 4\text{H}_2\text{O} - 4\text{H}^+ \leftrightarrow \text{Cd(OH)}_4^{2-}$	-47.30
$2\text{Cd}^{2+} + \text{H}_2\text{O} - \text{H}^+ \leftrightarrow \text{Cd}_2(\text{OH})^{3+}$	-9.40
$4\text{Cd}^{2+} + 4\text{H}_2\text{O} - 4\text{H}^+ \leftrightarrow \text{Cd}_4(\text{OH})_4^{4+}$	-32.80

SOURCE: Marell and Smith (1977)

TABLE B.2

CALCULATED STABILITY CONSTANTS FOR CD-MLGO INTERACTIONS FOR  
 MODELS THAT INCORPORATE VARYING AFFINITIES ASSOCIATED WITH  
 NA-MLGO BINDING

Active Sites	Site 1			Site 2			Site 3			Site 4			Errors	
	Log K <sub>Na-ads</sub>	Log K <sub>a</sub>	Log K <sub>Cd-ads</sub>	Log K <sub>Na-ads</sub>	Log K <sub>a</sub>	Log K <sub>Cd-ads</sub>	Log K <sub>Na-ads</sub>	Log K <sub>a</sub>	Log K <sub>Cd-ads</sub>	Log K <sub>Na-ads</sub>	Log K <sub>a</sub>	Log K <sub>Cd-ads</sub>	SSR H <sup>+</sup>	SSR Cd <sup>2+</sup>
Site 1	N/A	4.35	5.09	-	-	-	-	-	-	-	-	-	1.97	3.65
	0.50	4.44	5.20	-	-	-	-	-	-	-	-	-	2.53	3.34
	1.00	4.55	5.34	-	-	-	-	-	-	-	-	-	3.48	3.11
	1.50	4.74	5.59	-	-	-	-	-	-	-	-	-	5.28	3.08
	2.00	5.00	5.91	-	-	-	-	-	-	-	-	-	8.03	3.25
Site 1 & 2	N/A	4.35	4.75	N/A	6.32	5.71	-	-	-	-	-	-	1.97	3.88
	0.50	4.44	4.87	0.50	6.41	5.77	-	-	-	-	-	-	2.53	3.47
	1.00	4.55	5.01	1.00	6.52	5.84	-	-	-	-	-	-	3.48	2.95
	1.50	4.74	5.24	1.50	6.71	5.98	-	-	-	-	-	-	5.28	2.31
	2.00	5.00	5.54	2.00	6.97	6.18	-	-	-	-	-	-	8.03	1.90
Site 1 & 3	N/A	4.35	4.81	-	-	-	N/A	8.28	6.93	-	-	-	1.97	3.62
	0.50	4.44	4.94	-	-	-	0.50	8.36	6.96	-	-	-	2.53	3.26
	1.00	4.55	5.09	-	-	-	1.00	8.48	7.00	-	-	-	3.48	2.80
	1.50	4.74	5.34	-	-	-	1.50	8.67	6.95	-	-	-	5.28	1.98
	2.00	5.00	5.66	-	-	-	2.00	8.93	6.85	-	-	-	8.03	1.10
Site 1 & 4	N/A	4.35	4.82	-	-	-	-	-	-	N/A	9.77	8.11	1.97	3.61
	0.50	4.44	4.94	-	-	-	-	-	-	0.50	9.86	8.15	2.53	3.26
	1.00	4.55	5.09	-	-	-	-	-	-	1.00	9.98	8.18	3.48	2.80
	1.50	4.74	5.35	-	-	-	-	-	-	1.50	10.16	8.14	5.28	2.06
	2.00	5.00	5.67	-	-	-	-	-	-	2.00	10.42	7.87	8.03	1.04
Site 1, 2, & 4	N/A	4.35	dnc	N/A	6.32	dnc	-	-	-	N/A	9.77	dnc	1.97	dnc
	0.50	4.44	dnc	0.50	6.41	dnc	-	-	-	0.50	9.86	dnc	2.53	dnc
	1.00	4.55	5.03	1.00	6.52	4.44	-	-	-	1.00	9.98	6.81	3.48	1.78
	1.50	4.74	5.29	1.50	6.71	5.12	-	-	-	1.50	10.16	7.15	5.28	1.35
	2.00	5.00	5.63	2.00	6.97	5.39	-	-	-	2.00	10.42	7.45	8.03	0.99
Site 1, 3, & 4	N/A	4.35	dnc	-	-	-	N/A	8.28	dnc	N/A	9.77	dnc	1.97	dnc
	0.50	4.44	dnc	-	-	-	0.50	8.36	dnc	0.50	9.86	dnc	2.53	dnc
	1.00	4.55	dnc	-	-	-	1.00	8.48	dnc	1.00	9.98	dnc	3.48	dnc
	1.50	4.74	dnc	-	-	-	1.50	8.67	dnc	1.50	10.16	dnc	5.28	dnc
	2.00	5.00	5.64	-	-	-	2.00	8.93	6.53	2.00	10.42	6.83	8.03	0.94

TABLE B.3

CALCULATED STABILITY CONSTANTS FOR PB-MLGO INTERACTIONS FOR  
 MODELS THAT INCORPORATE VARYING AFFINITIES ASSOCIATED WITH  
 NA-MLGO BINDING

Active Sites	Site 1			Site 2			Site 3			Site 4			Errors	
	Log $K_{Na-ads}$	Log $K_a$	Log $K_{Pb-ads}$	Log $K_{Na-ads}$	Log $K_a$	Log $K_{Pb-ads}$	Log $K_{Na-ads}$	Log $K_a$	Log $K_{Pb-ads}$	Log $K_{Na-ads}$	Log $K_a$	Log $K_{Pb-ads}$	SSR $H^+$	SSR $Pb^{2+}$
Site 1	N/A	4.35	6.07	-	-	-	-	-	-	-	-	-	1.97	1.77
	0.50	4.44	6.14	-	-	-	-	-	-	-	-	-	2.53	1.65
	1.00	4.55	6.23	-	-	-	-	-	-	-	-	-	3.48	1.54
	1.50	4.47	6.40	-	-	-	-	-	-	-	-	-	5.28	1.42
	2.00	5.00	6.66	-	-	-	-	-	-	-	-	-	8.03	1.38
Site 1 & 2	N/A	4.35	5.68	N/A	6.32	6.92	-	-	-	-	-	-	1.97	0.60
	0.50	4.44	5.77	0.50	6.41	6.96	-	-	-	-	-	-	2.53	0.58
	1.00	4.55	5.89	1.00	6.52	7.01	-	-	-	-	-	-	3.48	0.53
	1.50	4.47	6.09	1.50	6.71	7.12	-	-	-	-	-	-	5.28	0.48
	2.00	5.00	6.36	2.00	6.97	7.26	-	-	-	-	-	-	8.03	0.46
Site 1 & 3	N/A	4.35	5.80	-	-	-	N/A	8.28	7.99	-	-	-	1.97	0.41
	0.50	4.44	5.88	-	-	-	0.50	8.36	8.02	-	-	-	2.53	0.39
	1.00	4.55	5.99	-	-	-	1.00	8.48	8.09	-	-	-	3.48	0.36
	1.50	4.47	6.18	-	-	-	1.50	8.67	8.20	-	-	-	5.28	0.30
	2.00	5.00	6.46	-	-	-	2.00	8.93	8.36	-	-	-	8.03	0.26
Site 1 & 4	N/A	4.35	5.80	-	-	-	-	-	-	N/A	9.77	9.15	1.97	0.41
	0.50	4.44	5.88	-	-	-	-	-	-	0.50	9.86	9.75	2.53	0.56
	1.00	4.55	5.99	-	-	-	-	-	-	1.00	9.98	9.70	3.48	0.46
	1.50	4.47	6.18	-	-	-	-	-	-	1.50	10.16	9.62	5.28	0.33
	2.00	5.00	6.46	-	-	-	-	-	-	2.00	10.42	9.52	8.03	0.26
Site 1 & 2OH	N/A	4.35	5.83	N/A	6.32	0.71 OH	-	-	-	-	-	-	1.97	0.41
	0.50	4.44	5.91	0.50	6.41	0.70 OH	-	-	-	-	-	-	2.53	0.39
	1.00	4.55	6.01	1.00	6.52	0.71 OH	-	-	-	-	-	-	3.48	0.34
	1.50	4.47	6.20	1.50	6.71	0.80 OH	-	-	-	-	-	-	5.28	0.28
	2.00	5.00	6.48	2.00	6.97	0.97 OH	-	-	-	-	-	-	8.03	0.24
Site 1 & 3OH	N/A	4.35	5.83	-	-	-	N/A	8.28	2.25 OH	-	-	-	1.97	0.42
	0.50	4.44	5.91	-	-	-	0.50	8.36	2.22 OH	-	-	-	2.53	0.39
	1.00	4.55	6.01	-	-	-	1.00	8.48	2.25 OH	-	-	-	3.48	0.35
	1.50	4.47	6.21	-	-	-	1.50	8.67	2.36 OH	-	-	-	5.28	0.30
	2.00	5.00	6.48	-	-	-	2.00	8.93	2.55 OH	-	-	-	8.03	0.24
Site 1 & 4OH	N/A	4.35	5.83	-	-	-	-	-	-	N/A	9.77	3.42 OH	1.97	0.42
	0.50	4.44	5.91	-	-	-	-	-	-	0.50	9.86	3.94 OH	2.53	0.45
	1.00	4.55	6.01	-	-	-	-	-	-	1.00	9.98	3.86 OH	3.48	0.40
	1.50	4.47	6.21	-	-	-	-	-	-	1.50	10.16	3.79 OH	5.28	0.32
	2.00	5.00	6.48	-	-	-	-	-	-	2.00	10.42	3.71 OH	8.03	0.24

NOTE: Site combinations designated with an "OH" are those that model the surface interaction between  $PbOH^+$  and the designated MLGO surface site.

TABLE B.4

SITE CONCENTRATIONS AND ACIDITY CONSTANTS FOR EACH  
 EXPERIMENTAL REPLICATE AS A FUNCTION OF IONIC STRENGTH AND NA-  
 MLGO AFFINITY

Log $K_{Na-ads}$ = N/A											
Ionic Strength		pK <sub>a</sub> Values				[Site] (mol/g)					V(Y)
		Site 1	Site 2	Site 3	Site 4	Site 1	Site 2	Site 3	Site 4	Total	
1 mM	R1	5.04	6.55	8.43	10.07	2.9E-04	4.0E-04	4.8E-04	1.6E-03	2.8E-03	0.06
	R2	4.16	6.35	8.36	10.01	4.4E-04	4.3E-04	5.3E-04	1.3E-03	2.7E-03	0.39
	R3	4.29	6.37	8.22	9.83	2.4E-04	4.4E-04	4.0E-04	1.2E-03	2.3E-03	0.17
	AVE	4.50	6.42	8.34	9.97	3.2E-04	4.2E-04	4.7E-04	1.4E-03	2.6E-03	0.21
	SD	0.48	0.11	0.11	0.12	1.0E-04	2.2E-05	6.8E-05	2.4E-04	3.1E-04	0.17
10 mM	R1	4.77	6.40	8.40	9.95	2.4E-04	3.1E-04	7.4E-04	1.1E-03	2.4E-03	0.24
	R2	3.41	6.01	8.32	9.71	6.8E-04	3.8E-04	6.7E-04	1.0E-03	2.7E-03	0.36
	R3	3.62	6.00	8.30	9.69	4.5E-04	3.6E-04	6.5E-04	9.8E-04	2.4E-03	0.33
	R4	3.50	5.97	8.36	9.72	6.6E-04	3.7E-04	6.9E-04	9.7E-04	2.7E-03	0.56
	R5	3.08	5.95	8.38	9.74	1.2E-03	3.9E-04	7.1E-04	9.5E-04	3.2E-03	0.54
	R6	3.54	6.07	8.24	9.76	5.9E-04	3.8E-04	6.7E-04	9.9E-04	2.6E-03	0.32
	R7	3.21	5.98	8.29	9.69	1.2E-03	4.4E-04	8.0E-04	1.2E-03	3.6E-03	0.45
	AVE	3.59	6.05	8.33	9.75	7.1E-04	3.8E-04	7.0E-04	1.0E-03	2.8E-03	0.40
	SD	0.55	0.16	0.06	0.09	3.5E-04	4.0E-05	5.3E-05	7.8E-05	4.3E-04	0.12
100 mM	R1	3.79	6.21	8.27	9.68	5.1E-04	5.7E-04	7.3E-04	1.3E-03	3.1E-03	0.55
	R2	4.04	6.04	8.38	9.77	3.3E-04	4.4E-04	8.7E-04	1.2E-03	2.8E-03	0.28
	R3	3.93	5.92	7.95	9.42	3.3E-04	3.7E-04	5.2E-04	1.3E-03	2.5E-03	0.46
	R4	4.14	5.90	7.57	8.93	3.2E-04	3.9E-04	3.9E-04	1.1E-03	2.2E-03	3.64
	R5	3.69	6.12	8.24	9.74	4.5E-04	5.1E-04	7.9E-04	1.1E-03	2.8E-03	0.48
	R6	4.01	6.09	8.32	9.96	4.5E-04	5.1E-04	1.0E-03	1.5E-03	3.5E-03	0.36
	R7	4.55	6.34	8.38	9.85	3.5E-04	4.5E-04	9.7E-04	1.1E-03	2.9E-03	0.11
	AVE	4.02	6.09	8.16	9.62	3.9E-04	4.6E-04	7.6E-04	1.2E-03	2.8E-03	0.84
	SD	0.28	0.16	0.30	0.35	7.4E-05	7.2E-05	2.4E-04	1.4E-04	4.0E-04	1.24
300 mM	R1	5.20	6.85	8.30	9.65	4.1E-04	4.8E-04	5.0E-04	1.3E-03	2.7E-03	0.39
	R2	5.23	6.60	8.25	9.79	3.3E-04	3.1E-04	8.6E-04	1.4E-03	3.0E-03	0.51
	R3	5.25	6.75	8.27	9.75	4.2E-04	4.8E-04	6.4E-04	1.3E-03	2.9E-03	0.15
	R4	5.48	6.70	8.35	9.83	4.3E-04	3.4E-04	8.6E-04	1.7E-03	3.3E-03	0.85
	AVE	5.29	6.73	8.29	9.76	4.0E-04	4.0E-04	7.2E-04	1.4E-03	3.0E-03	0.47
SD	0.13	0.10	0.04	0.08	4.5E-05	8.7E-05	1.8E-04	1.5E-04	2.5E-04	0.29	
Combined	AVE	4.35	6.32	8.28	9.77	4.6E-04	4.2E-04	6.6E-04	1.3E-03	2.8E-03	0.48
	SD	0.73	0.32	0.08	0.15	1.7E-04	3.7E-05	1.3E-04	1.9E-04	1.5E-04	

TABLE B.4 (CONTINUED)

Log $K_{Na-ads} = 0.5$											
Ionic Strength		pK <sub>a</sub> Values				[Site] (mol/g)					V(Y)
		Site 1	Site 2	Site 3	Site 4	Site 1	Site 2	Site 3	Site 4	Total	
<b>1 mM</b>	R1	5.04	6.55	8.44	10.10	3.0E-04	4.0E-04	4.8E-04	1.6E-03	2.8E-03	0.06
	R2	4.17	6.35	8.37	10.00	4.4E-04	4.3E-04	5.3E-04	1.3E-03	2.7E-03	0.39
	R3	4.29	6.37	8.22	9.84	2.4E-04	4.4E-04	4.0E-04	1.2E-03	2.3E-03	0.17
	AVE	4.50	6.42	8.34	9.98	3.2E-04	4.2E-04	4.7E-04	1.4E-03	2.6E-03	0.21
	SD	0.47	0.11	0.11	0.13	1.0E-04	2.1E-05	6.8E-05	2.4E-04	3.1E-04	0.17
<b>10 mM</b>	R1	4.78	6.41	8.41	9.96	2.4E-04	3.1E-04	7.4E-04	1.1E-03	2.4E-03	0.24
	R2	3.43	6.02	8.33	9.72	6.8E-04	3.8E-04	6.7E-04	1.0E-03	2.7E-03	0.36
	R3	3.63	6.02	8.31	9.70	4.5E-04	3.6E-04	6.5E-04	9.8E-04	2.4E-03	0.33
	R4	3.51	5.98	8.38	9.73	6.6E-04	3.7E-04	6.9E-04	9.7E-04	2.7E-03	0.56
	R5	3.09	5.96	8.39	9.76	1.2E-03	3.9E-04	7.1E-04	9.5E-04	3.2E-03	0.54
	R6	3.56	6.09	8.25	9.77	5.9E-04	3.8E-04	6.7E-04	9.9E-04	2.6E-03	0.32
	R7	3.22	5.99	8.30	9.71	1.2E-03	4.4E-04	8.0E-04	1.2E-03	3.6E-03	0.45
	AVE	3.60	6.07	8.34	9.76	7.1E-04	3.8E-04	7.0E-04	1.0E-03	2.8E-03	0.40
	SD	0.55	0.16	0.06	0.09	3.5E-04	4.0E-05	5.3E-05	7.7E-05	4.3E-04	0.12
<b>100 mM</b>	R1	3.89	6.31	8.37	9.78	5.1E-04	5.7E-04	7.3E-04	1.3E-03	3.1E-03	0.55
	R2	4.14	6.14	8.47	9.87	3.3E-04	4.4E-04	8.7E-04	1.2E-03	2.8E-03	0.28
	R3	4.02	6.01	8.04	9.51	3.3E-04	3.7E-04	5.2E-04	1.3E-03	2.5E-03	0.46
	R4	4.23	5.99	7.67	9.03	3.2E-04	3.9E-04	3.9E-04	1.1E-03	2.2E-03	3.64
	R5	3.79	6.22	8.34	9.83	4.5E-04	5.1E-04	7.9E-04	1.1E-03	2.8E-03	0.48
	R6	4.10	6.19	8.42	10.10	4.5E-04	5.1E-04	1.0E-03	1.5E-03	3.5E-03	0.36
	R7	4.65	6.44	8.48	9.95	3.5E-04	4.5E-04	9.7E-04	1.1E-03	2.9E-03	0.11
	AVE	4.12	6.19	8.26	9.72	3.9E-04	4.6E-04	7.6E-04	1.2E-03	2.8E-03	0.84
	SD	0.28	0.16	0.30	0.35	7.4E-05	7.2E-05	2.4E-04	1.4E-04	4.0E-04	1.24
<b>300 mM</b>	R1	5.43	7.08	8.53	9.88	4.1E-04	4.8E-04	5.0E-04	1.3E-03	2.7E-03	0.39
	R2	5.46	6.83	8.47	10.00	3.3E-04	3.1E-04	8.6E-04	1.4E-03	2.9E-03	0.51
	R3	5.48	6.97	8.50	9.98	4.2E-04	4.8E-04	6.4E-04	1.3E-03	2.9E-03	0.15
	R4	5.71	6.93	8.58	10.10	4.3E-04	3.4E-04	8.6E-04	1.7E-03	3.3E-03	0.85
	AVE	5.52	6.95	8.52	9.99	4.0E-04	4.0E-04	7.2E-04	1.4E-03	3.0E-03	0.47
	SD	0.13	0.10	0.05	0.09	4.6E-05	8.7E-05	1.8E-04	1.5E-04	2.5E-04	0.29
<b>Combined</b>	AVE	4.44	6.41	8.36	9.86	4.6E-04	4.2E-04	6.6E-04	1.3E-03	2.8E-03	0.48
	SD	0.81	0.39	0.11	0.14	1.7E-04	3.7E-05	1.3E-04	1.9E-04	1.5E-04	0.27

TABLE B.4 (CONTINUED)

Log $K_{Na-ads} = 1.0$											
Ionic Strength		pK <sub>a</sub> Values				[Site] (mol/g)					V(Y)
		Site 1	Site 2	Site 3	Site 4	Site 1	Site 2	Site 3	Site 4	Total	
<b>1 mM</b>	R1	5.05	6.56	8.44	10.10	3.0E-04	4.0E-04	4.8E-04	1.6E-03	2.8E-03	0.06
	R2	4.17	6.35	8.37	10.00	4.4E-04	4.3E-04	5.3E-04	1.3E-03	2.7E-03	0.39
	R3	4.29	6.38	8.23	9.84	2.4E-04	4.4E-04	4.0E-04	1.2E-03	2.3E-03	0.17
	AVE	4.50	6.43	8.35	9.98	3.2E-04	4.2E-04	4.7E-04	1.4E-03	2.6E-03	0.21
	SD	0.48	0.11	0.11	0.13	1.0E-04	2.1E-05	6.8E-05	2.4E-04	3.1E-04	0.17
<b>10 mM</b>	R1	4.81	6.44	8.44	9.99	2.4E-04	3.1E-04	7.4E-04	1.1E-03	2.4E-03	0.24
	R2	3.45	6.05	8.36	9.75	6.8E-04	3.8E-04	6.7E-04	1.0E-03	2.7E-03	0.36
	R3	3.65	6.04	8.34	9.73	4.5E-04	3.6E-04	6.5E-04	9.8E-04	2.4E-03	0.33
	R4	3.54	6.01	8.40	9.75	6.6E-04	3.7E-04	6.9E-04	9.7E-04	2.7E-03	0.56
	R5	3.12	5.98	8.42	9.78	1.2E-03	3.9E-04	7.1E-04	9.5E-04	3.2E-03	0.54
	R6	3.58	6.11	8.27	9.79	5.9E-04	3.8E-04	6.7E-04	9.9E-04	2.6E-03	0.32
	R7	3.24	6.02	8.33	9.73	1.2E-03	4.4E-04	8.0E-04	1.2E-03	3.6E-03	0.45
	AVE	3.63	6.09	8.37	9.79	7.1E-04	3.8E-04	7.0E-04	1.0E-03	2.8E-03	0.40
	SD	0.55	0.16	0.06	0.09	3.5E-04	4.0E-05	5.3E-05	7.7E-05	4.3E-04	0.12
<b>100 mM</b>	R1	4.04	6.46	8.52	9.93	5.1E-04	5.7E-04	7.3E-04	1.3E-03	3.1E-03	0.55
	R2	4.29	6.29	8.63	10.00	3.3E-04	4.4E-04	8.7E-04	1.2E-03	2.8E-03	0.28
	R3	4.18	6.17	8.20	9.67	3.3E-04	3.7E-04	5.1E-04	1.3E-03	2.5E-03	0.46
	R4	4.39	6.15	7.82	9.18	3.2E-04	3.9E-04	3.9E-04	1.1E-03	2.2E-03	3.64
	R5	3.94	6.37	8.49	9.99	4.5E-04	5.1E-04	7.9E-04	1.1E-03	2.8E-03	0.48
	R6	4.26	6.34	8.57	10.20	4.5E-04	5.1E-04	1.0E-03	1.5E-03	3.5E-03	0.36
	R7	4.80	6.59	8.63	10.10	3.5E-04	4.5E-04	9.7E-04	1.1E-03	2.9E-03	0.11
	AVE	4.27	6.34	8.41	9.87	3.9E-04	4.6E-04	7.6E-04	1.2E-03	2.8E-03	0.84
	SD	0.28	0.16	0.30	0.34	7.4E-05	7.2E-05	2.4E-04	1.4E-04	4.0E-04	1.24
<b>300 mM</b>	R1	5.71	7.35	8.81	10.20	4.1E-04	4.8E-04	5.0E-04	1.3E-03	2.7E-03	0.39
	R2	5.74	7.11	8.75	10.30	3.3E-04	3.1E-04	8.6E-04	1.4E-03	2.9E-03	0.51
	R3	5.75	7.25	8.78	10.30	4.2E-04	4.8E-04	6.4E-04	1.3E-03	2.9E-03	0.15
	R4	5.98	7.21	8.86	10.30	4.3E-04	3.4E-04	8.6E-04	1.7E-03	3.3E-03	0.85
	AVE	5.80	7.23	8.80	10.28	4.0E-04	4.0E-04	7.2E-04	1.4E-03	3.0E-03	0.47
	SD	0.12	0.10	0.05	0.05	4.6E-05	8.7E-05	1.8E-04	1.5E-04	2.5E-04	0.29
<b>Combined</b>	AVE	4.55	6.52	8.48	9.98	4.6E-04	4.2E-04	6.6E-04	1.3E-03	2.8E-03	0.48
	SD	0.91	0.49	0.21	0.21	1.7E-04	3.7E-05	1.3E-04	1.9E-04	1.5E-04	0.26

TABLE B.4 (CONTINUED)

Log $K_{Na-ads} = 1.5$											
Ionic Strength		pK <sub>a</sub> Values				[Site] (mol/g)					V(Y)
		Site 1	Site 2	Site 3	Site 4	Site 1	Site 2	Site 3	Site 4	Total	
<b>1 mM</b>	R1	5.06	6.56	8.45	10.10	3.0E-04	4.0E-04	4.8E-04	1.6E-03	2.8E-03	0.06
	R2	4.18	6.36	8.38	10.00	4.4E-04	4.3E-04	5.3E-04	1.3E-03	2.7E-03	0.39
	R3	4.30	6.39	8.24	9.85	2.4E-04	4.4E-04	4.0E-04	1.2E-03	2.3E-03	0.17
	AVE	4.51	6.44	8.36	9.98	3.2E-04	4.2E-04	4.7E-04	1.4E-03	2.6E-03	0.21
	SD	0.48	0.11	0.11	0.13	1.0E-04	2.1E-05	6.8E-05	2.4E-04	3.1E-04	0.17
<b>10 mM</b>	R1	4.88	6.51	8.51	10.10	2.4E-04	3.1E-04	7.4E-04	1.1E-03	2.4E-03	0.24
	R2	3.52	6.12	8.43	9.81	6.8E-04	3.8E-04	6.7E-04	1.0E-03	2.7E-03	0.36
	R3	3.72	6.11	8.41	9.79	4.5E-04	3.6E-04	6.5E-04	9.8E-04	2.4E-03	0.33
	R4	3.61	6.08	8.47	9.82	6.6E-04	3.7E-04	6.9E-04	9.7E-04	2.7E-03	0.56
	R5	3.19	6.05	8.48	9.85	1.2E-03	3.9E-04	7.1E-04	9.5E-04	3.2E-03	0.54
	R6	3.65	6.18	8.34	9.86	5.9E-04	3.8E-04	6.7E-04	9.9E-04	2.6E-03	0.32
	R7	3.31	6.09	8.39	9.80	1.2E-03	4.4E-04	8.0E-04	1.2E-03	3.6E-03	0.45
	AVE	3.70	6.16	8.43	9.86	7.1E-04	3.8E-04	7.0E-04	1.0E-03	2.8E-03	0.40
	SD	0.55	0.16	0.06	0.11	3.5E-04	4.0E-05	5.3E-05	7.7E-05	4.3E-04	0.12
<b>100 mM</b>	R1	4.33	6.75	8.81	10.20	5.1E-04	5.7E-04	7.3E-04	1.3E-03	3.1E-03	0.55
	R2	4.58	6.58	8.92	10.30	3.3E-04	4.4E-04	8.7E-04	1.2E-03	2.8E-03	0.28
	R3	4.46	6.46	8.48	9.96	3.3E-04	3.7E-04	5.1E-04	1.3E-03	2.5E-03	0.46
	R4	4.68	6.43	8.11	9.47	3.2E-04	3.9E-04	3.9E-04	1.1E-03	2.2E-03	3.64
	R5	4.23	6.66	8.78	10.30	4.5E-04	5.1E-04	7.9E-04	1.1E-03	2.8E-03	0.48
	R6	4.54	6.63	8.86	10.50	4.5E-04	5.1E-04	1.0E-03	1.5E-03	3.5E-03	0.36
	R7	5.09	6.88	8.92	10.40	3.5E-04	4.5E-04	9.7E-04	1.1E-03	2.9E-03	0.11
	AVE	4.56	6.63	8.70	10.16	3.9E-04	4.6E-04	7.6E-04	1.2E-03	2.9E-03	0.84
	SD	0.28	0.16	0.30	0.35	7.4E-05	7.2E-05	2.4E-04	1.4E-04	4.0E-04	1.24
<b>300 mM</b>	R1	6.10	7.75	9.20	10.50	4.1E-04	4.8E-04	5.0E-04	1.3E-03	2.7E-03	0.39
	R2	6.14	7.50	9.15	10.70	3.3E-04	3.1E-04	8.6E-04	1.4E-03	2.9E-03	0.51
	R3	6.15	7.64	9.17	10.70	4.2E-04	4.8E-04	6.4E-04	1.3E-03	2.9E-03	0.15
	R4	6.38	7.60	9.25	10.70	4.3E-04	3.4E-04	8.6E-04	1.7E-03	3.3E-03	0.85
	AVE	6.19	7.62	9.19	10.65	4.0E-04	4.0E-04	7.2E-04	1.4E-03	3.0E-03	0.47
	SD	0.13	0.10	0.04	0.10	4.6E-05	8.8E-05	1.8E-04	1.5E-04	2.5E-04	0.29
<b>Combined</b>	AVE	4.74	6.71	8.67	10.16	4.6E-04	4.2E-04	6.6E-04	1.3E-03	2.8E-03	0.48
	SD	1.05	0.64	0.38	0.35	1.7E-04	3.7E-05	1.3E-04	1.9E-04	1.5E-04	

TABLE B.4 (CONTINUED)

Log $K_{Na-ads} = 2.0$											
Ionic Strength		pK <sub>a</sub> Values				[Site] (mol/g)					V(Y)
		Site 1	Site 2	Site 3	Site 4	Site 1	Site 2	Site 3	Site 4	Total	
<b>1 mM</b>	R1	5.08	6.59	8.47	10.10	2.9E-04	4.0E-04	4.8E-04	1.6E-03	2.8E-03	0.06
	R2	4.20	6.38	8.40	10.00	4.4E-04	4.3E-04	5.3E-04	1.3E-03	2.7E-03	0.39
	R3	4.33	6.41	8.26	9.87	2.4E-04	4.4E-04	4.0E-04	1.2E-03	2.3E-03	0.17
	AVE	4.54	6.46	8.38	9.99	3.2E-04	4.2E-04	4.7E-04	1.4E-03	2.6E-03	0.20
	SD	0.48	0.11	0.11	0.12	1.0E-04	2.1E-05	6.8E-05	2.4E-04	3.0E-04	0.17
<b>10 mM</b>	R1	5.05	6.67	8.67	10.20	2.4E-04	3.1E-04	7.5E-04	1.1E-03	2.4E-03	0.23
	R2	3.68	6.28	8.59	9.97	6.9E-04	3.8E-04	6.7E-04	1.0E-03	2.7E-03	0.35
	R3	3.89	6.27	8.57	9.95	4.5E-04	3.6E-04	6.5E-04	9.8E-04	2.4E-03	0.32
	R4	3.77	6.24	8.63	9.98	6.6E-04	3.7E-04	6.9E-04	9.7E-04	2.7E-03	0.55
	R5	3.34	6.21	8.64	10.00	1.2E-03	3.9E-04	7.1E-04	9.6E-04	3.3E-03	0.53
	R6	3.81	6.34	8.50	10.00	5.9E-04	3.8E-04	6.7E-04	9.9E-04	2.6E-03	0.31
	R7	3.47	6.24	8.55	9.95	1.2E-03	4.4E-04	8.0E-04	1.2E-03	3.6E-03	0.44
	AVE	3.86	6.32	8.59	10.01	7.2E-04	3.8E-04	7.0E-04	1.0E-03	2.8E-03	0.39
	SD	0.56	0.16	0.06	0.09	3.6E-04	4.0E-05	5.3E-05	8.0E-05	4.4E-04	0.12
<b>100 mM</b>	R1	4.74	7.15	9.21	10.60	5.1E-04	5.7E-04	7.3E-04	1.3E-03	3.1E-03	0.55
	R2	4.98	6.99	9.32	10.70	3.3E-04	4.4E-04	8.7E-04	1.2E-03	2.8E-03	0.27
	R3	4.87	6.86	8.89	10.40	3.3E-04	3.7E-04	5.1E-04	1.3E-03	2.5E-03	0.46
	R4	5.08	6.84	8.51	9.87	3.2E-04	3.9E-04	3.9E-04	1.1E-03	2.2E-03	3.64
	R5	4.64	7.06	9.18	10.70	4.5E-04	5.1E-04	7.9E-04	1.1E-03	2.8E-03	0.48
	R6	4.95	7.03	9.26	10.90	4.5E-04	5.1E-04	1.0E-03	1.5E-03	3.5E-03	0.36
	R7	5.50	7.28	9.33	10.80	3.5E-04	4.5E-04	9.7E-04	1.1E-03	2.9E-03	0.11
	AVE	4.97	7.03	9.10	10.57	3.9E-04	4.6E-04	7.6E-04	1.2E-03	2.9E-03	0.84
	SD	0.28	0.16	0.30	0.35	7.4E-05	7.2E-05	2.4E-04	1.4E-04	4.0E-04	1.24
<b>300 mM</b>	R1	6.56	8.21	9.66	11.00	4.1E-04	4.8E-04	5.0E-04	1.3E-03	2.7E-03	0.39
	R2	6.60	7.97	9.61	11.20	3.3E-04	3.1E-04	8.6E-04	1.4E-03	2.9E-03	0.51
	R3	6.61	8.11	9.63	11.10	4.2E-04	4.8E-04	6.4E-04	1.3E-03	2.9E-03	0.15
	R4	6.84	8.06	9.71	11.20	4.3E-04	3.4E-04	8.6E-04	1.7E-03	3.3E-03	0.85
	AVE	6.65	8.09	9.65	11.13	4.0E-04	4.0E-04	7.2E-04	1.4E-03	3.0E-03	0.47
	SD	0.13	0.10	0.04	0.10	4.6E-05	8.8E-05	1.8E-04	1.5E-04	2.5E-04	0.29
<b>Combined</b>	AVE	5.00	6.97	8.93	10.42	4.6E-04	4.2E-04	6.6E-04	1.3E-03	2.8E-03	0.48
	SD	1.19	0.80	0.57	0.54	1.8E-04	3.7E-05	1.3E-04	1.8E-04	1.5E-04	

APPENDIX C:  
ADDITIONAL FIGURES AND TABLES FOR CHAPTER 3

TABLE C.1

## LOG K VALUES FOR AQUEOUS URANYL COMPLEXATION REACTIONS

## UTILIZED IN FITEQL

Reaction	Log K
<i>General</i>	
$\text{H}_2\text{O} - \text{H}^+ \leftrightarrow \text{OH}^-$	-14.00
$\text{Na}^+ + \text{H}_2\text{O} - \text{H}^+ \leftrightarrow \text{NaOH}^0$	-14.18
$\text{H}_2\text{CO}_3^0 - \text{H}^+ \leftrightarrow \text{HCO}_3^-$	-6.35
$\text{H}_2\text{CO}_3^0 - 2\text{H}^+ \leftrightarrow \text{CO}_3^-$	-16.67
<i>U - Aqueous Complexes</i>	
$\text{UO}_2^{2+} + \text{H}_2\text{O} - \text{H}^+ \leftrightarrow \text{UO}_2(\text{OH})^+$	-5.25
$\text{UO}_2^{2+} + 2\text{H}_2\text{O} - 2\text{H}^+ \leftrightarrow \text{UO}_2(\text{OH})_2^0$	-12.15
$\text{UO}_2^{2+} + 3\text{H}_2\text{O} - 3\text{H}^+ \leftrightarrow \text{UO}_2(\text{OH})_3^-$	-20.25
$\text{UO}_2^{2+} + 4\text{H}_2\text{O} - 4\text{H}^+ \leftrightarrow \text{UO}_2(\text{OH})_4^{2-}$	-32.40
$2\text{UO}_2^{2+} + \text{H}_2\text{O} - \text{H}^+ \leftrightarrow (\text{UO}_2)_2(\text{OH})^{3+}$	-2.70
$2\text{UO}_2^{2+} + 2\text{H}_2\text{O} - 2\text{H}^+ \leftrightarrow (\text{UO}_2)_2(\text{OH})_2^{2+}$	-5.62
$3\text{UO}_2^{2+} + 5\text{H}_2\text{O} - 5\text{H}^+ \leftrightarrow (\text{UO}_2)_3(\text{OH})_5^+$	-15.55
$3\text{UO}_2^{2+} + 7\text{H}_2\text{O} - 7\text{H}^+ \leftrightarrow (\text{UO}_2)_3(\text{OH})_7^-$	-32.22
$4\text{UO}_2^{2+} + 7\text{H}_2\text{O} - 7\text{H}^+ \leftrightarrow (\text{UO}_2)_4(\text{OH})_7^+$	-21.90
$3\text{UO}_2^{2+} + 4\text{H}_2\text{O} - 4\text{H}^+ \leftrightarrow (\text{UO}_2)_3(\text{OH})_4^{2+}$	-11.90
$\text{UO}_2^{2+} + \text{H}_2\text{CO}_3^0 - 2\text{H}^+ \leftrightarrow (\text{UO}_2)(\text{CO}_3)^0$	-6.74
$\text{UO}_2^{2+} + 2\text{H}_2\text{CO}_3^0 - 4\text{H}^+ \leftrightarrow (\text{UO}_2)(\text{CO}_3)_2^{2-}$	-16.75
$\text{UO}_2^{2+} + 3\text{H}_2\text{CO}_3^0 - 6\text{H}^+ \leftrightarrow (\text{UO}_2)(\text{CO}_3)_3^{4-}$	-28.20
$3\text{UO}_2^{2+} + 6\text{H}_2\text{CO}_3^0 - 12\text{H}^+ \leftrightarrow (\text{UO}_2)_3(\text{CO}_3)_6^{6-}$	-46.08
$2\text{UO}_2^{2+} + 3\text{H}_2\text{O} + \text{H}_2\text{CO}_3^0 - 5\text{H}^+ \leftrightarrow (\text{UO}_2)_2(\text{CO}_3)(\text{OH})_3^-$	-17.54
$3\text{UO}_2^{2+} + 3\text{H}_2\text{O} + \text{H}_2\text{CO}_3^0 - 5\text{H}^+ \leftrightarrow (\text{UO}_2)_3(\text{CO}_3)(\text{OH})_3^+$	-16.03
$11\text{UO}_2^{2+} + 12\text{H}_2\text{O} + 6\text{H}_2\text{CO}_3^0 - 24\text{H}^+ \leftrightarrow (\text{UO}_2)_{11}(\text{CO}_3)_6(\text{OH})_{12}^{2-}$	-63.67

SOURCE: Martell and Smith (1977)

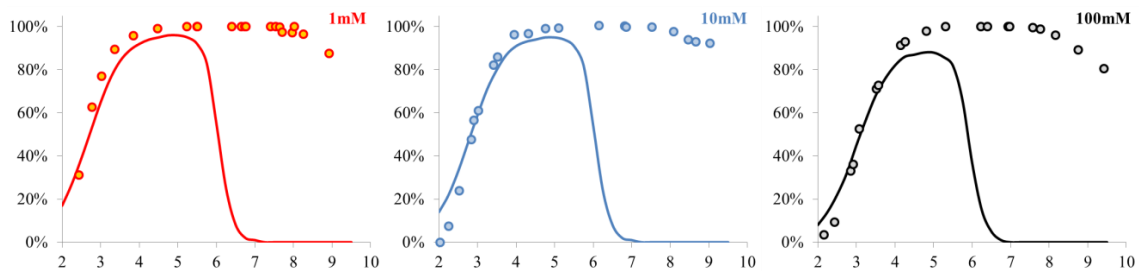


Figure C.1: Predicted of U sorption behavior using a non-electrostatic model that assumes sorption of  $UO_2^{2+}$  to Site 1 only ( $\text{Log } K_{ads} = 5.76$ ) and a  $\text{Log } K_{Na-ads} = 1.0$ . Prediction curves are shown in relation to actual measured replicate U sorption extents for three ionic strength treatments. Axes are as follows: X (pH); Y (%U Sorbed).

APPENDIX D:  
ADDITIONAL FIGURES AND TABLES FOR CHAPTER 4

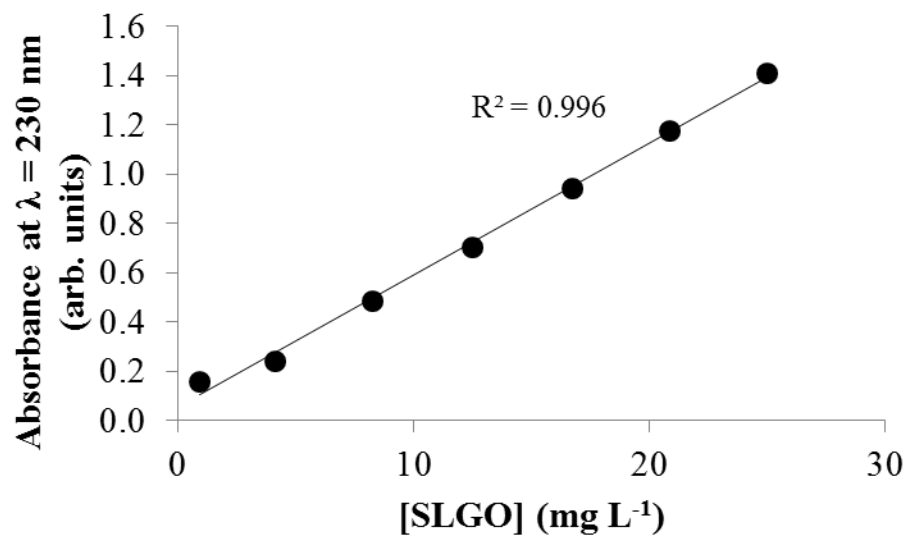


Figure D.1: Regression analysis showing a linear relationship between SLGO concentration and UV-vis absorbance at  $\lambda = 230$  nm.

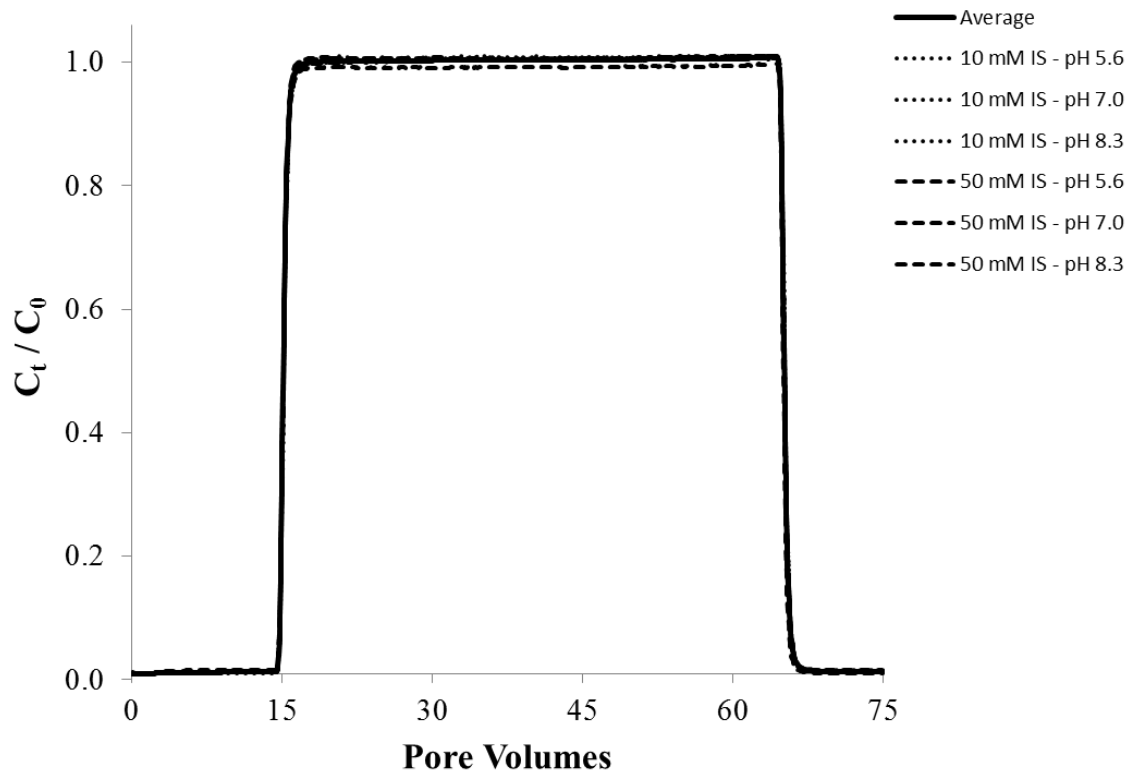
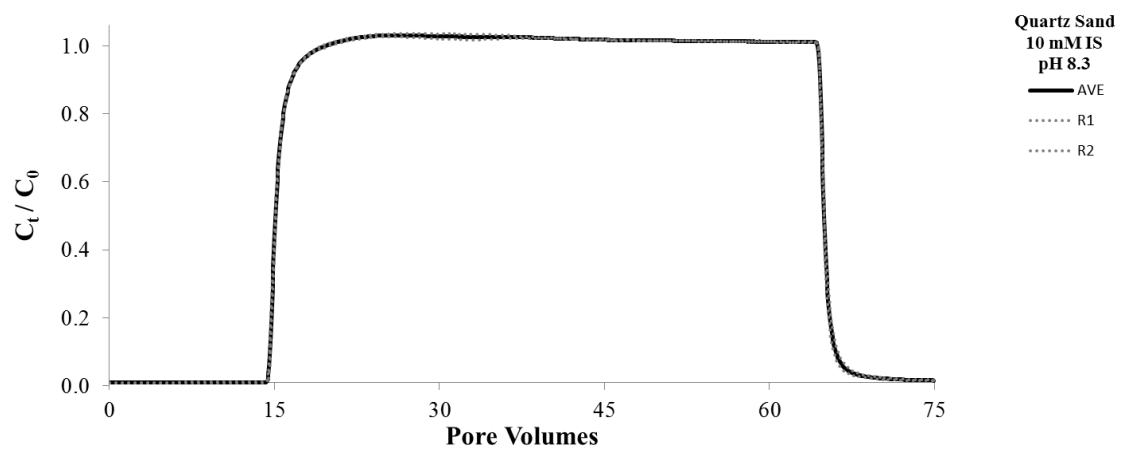
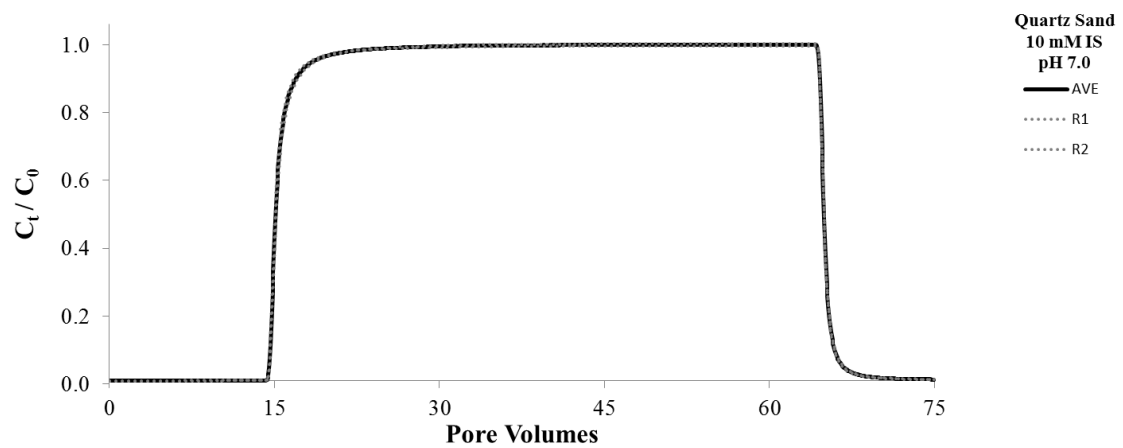
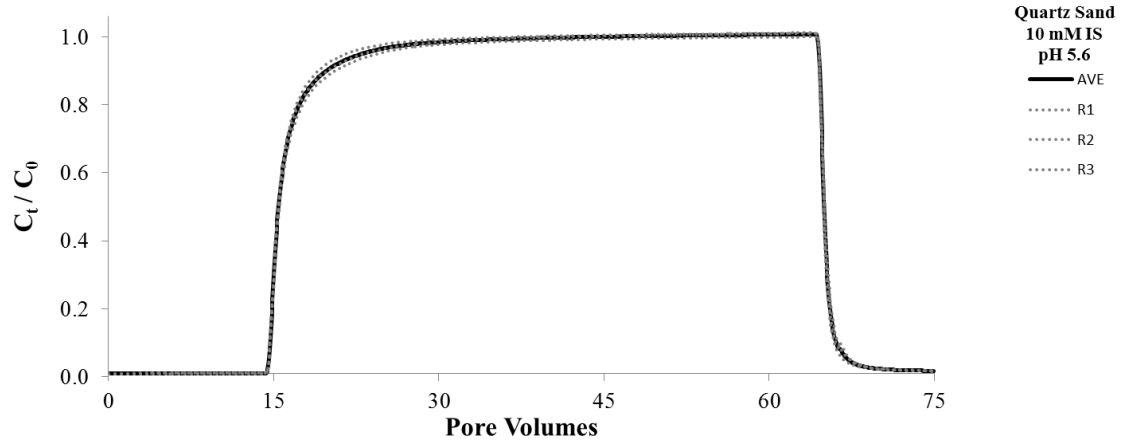
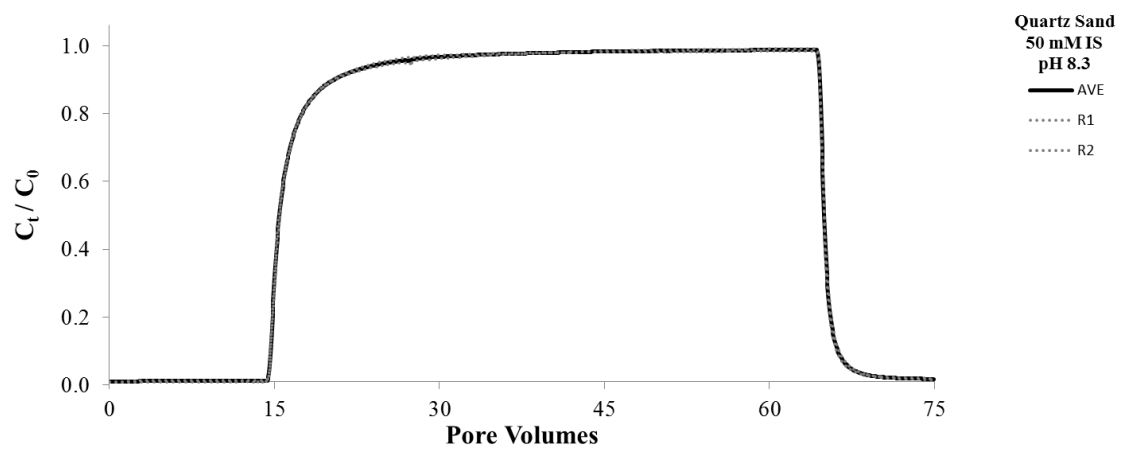
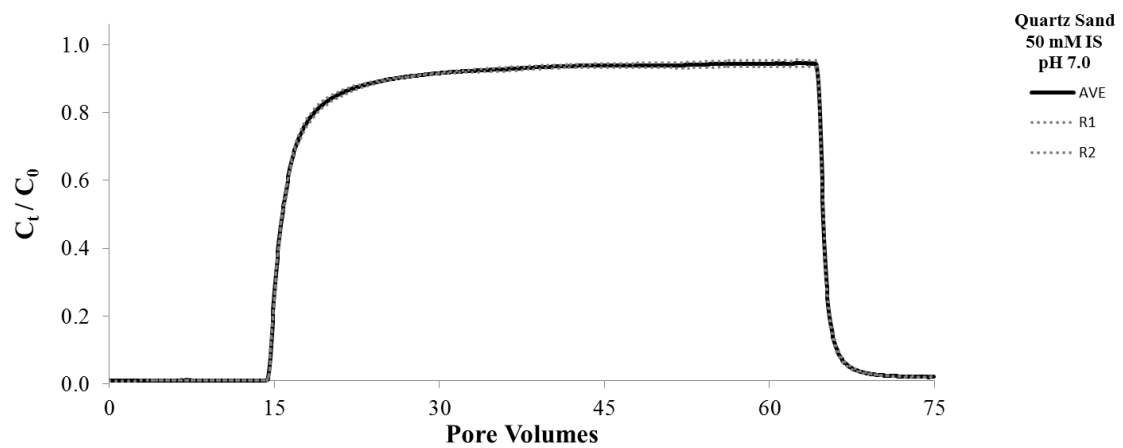
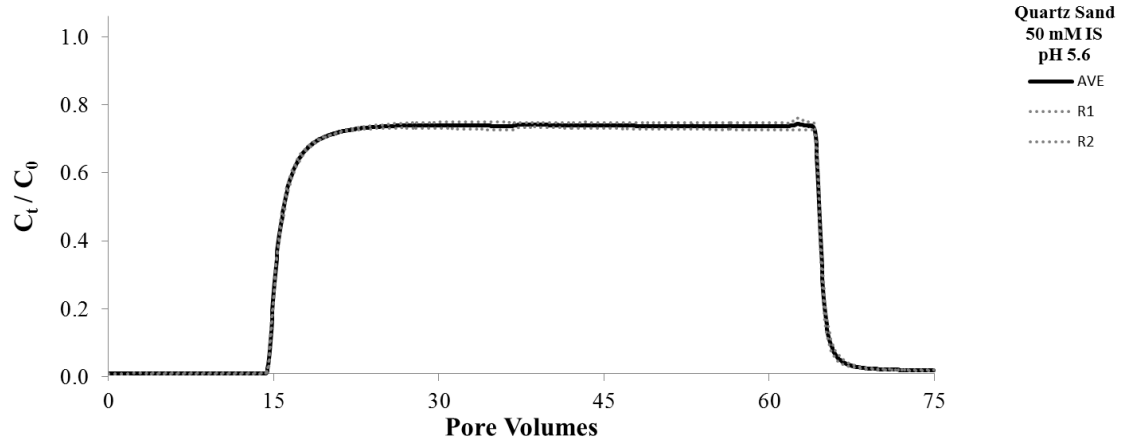


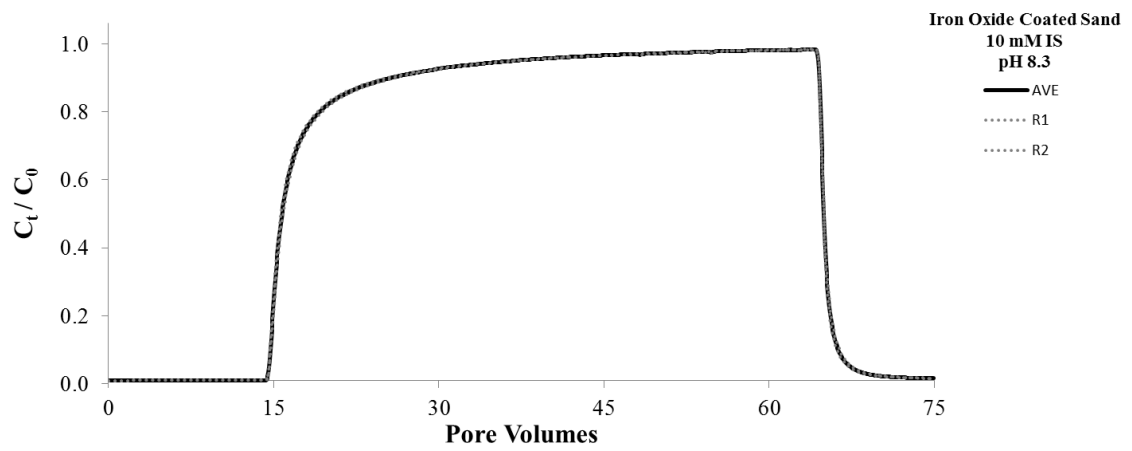
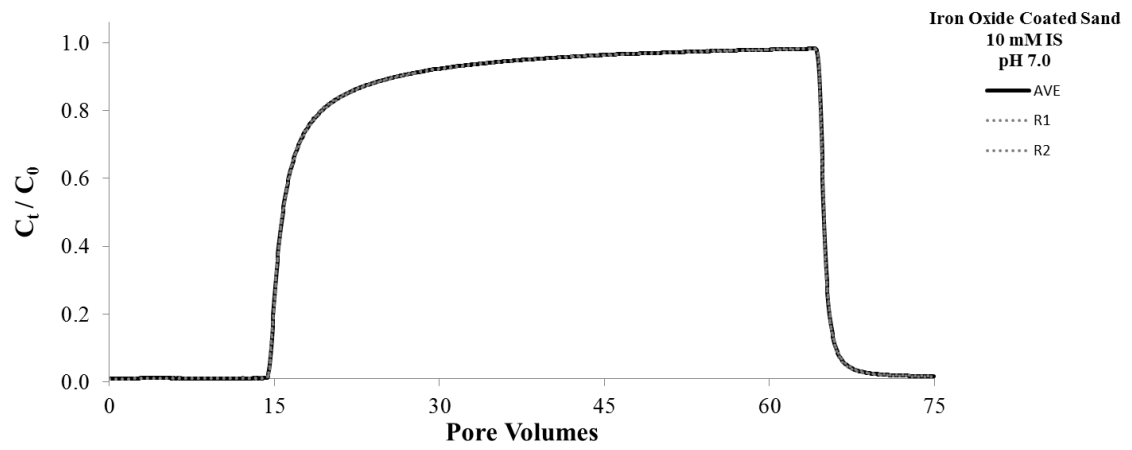
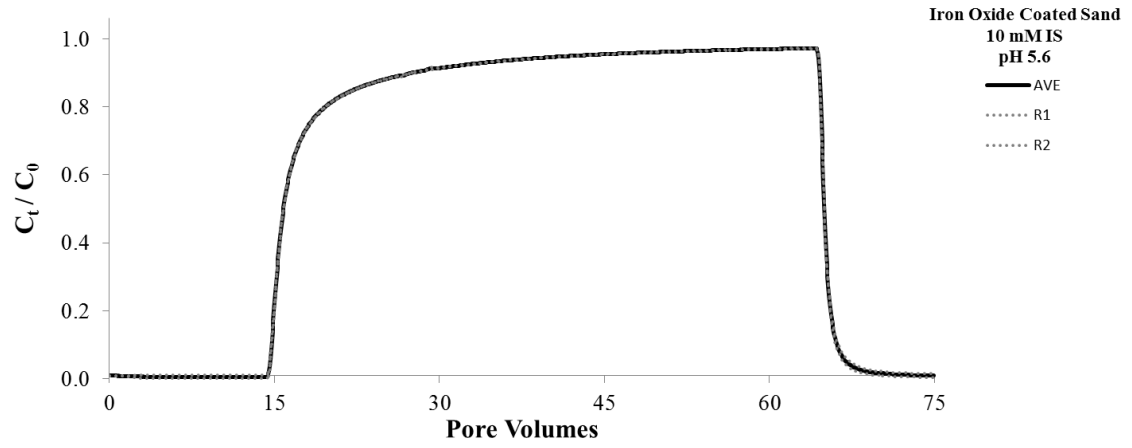
Figure D.2: Breakthrough of the conservative NaBr tracer through quartz sand in the electrochemical environments listed in the figure legend. Virtually all breakthrough curves directly overlapped, so we averaged them and used this average curve for comparison to SLGO nanosheet transport, as depicted in Figure 4.5 in the text.

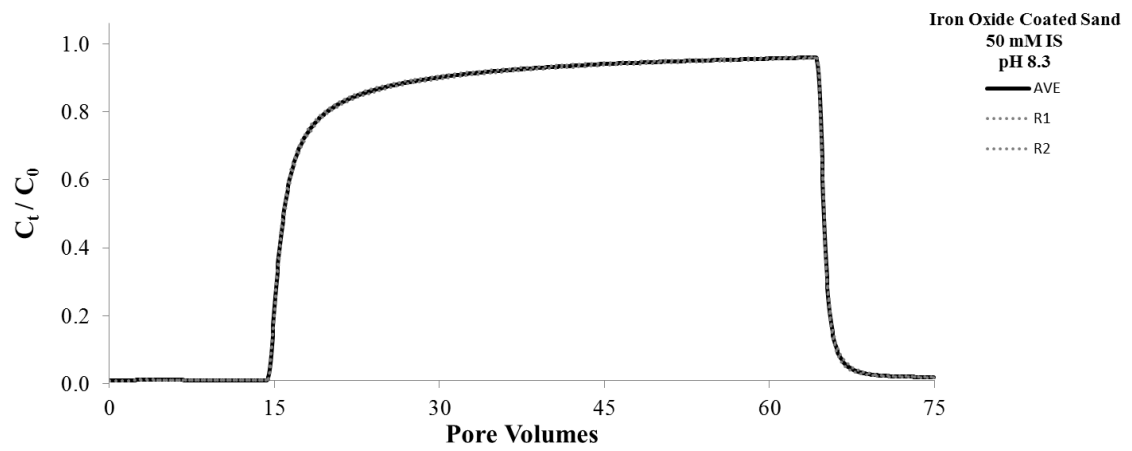
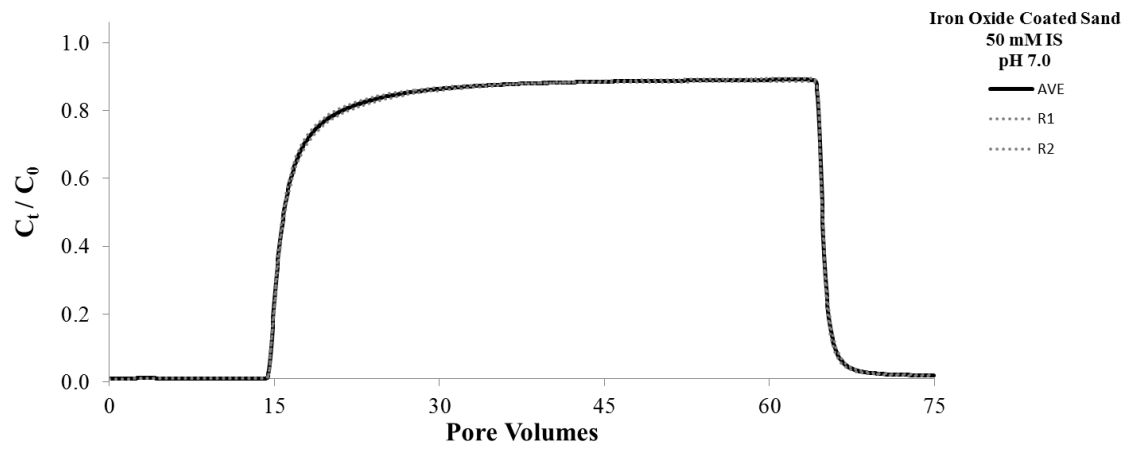
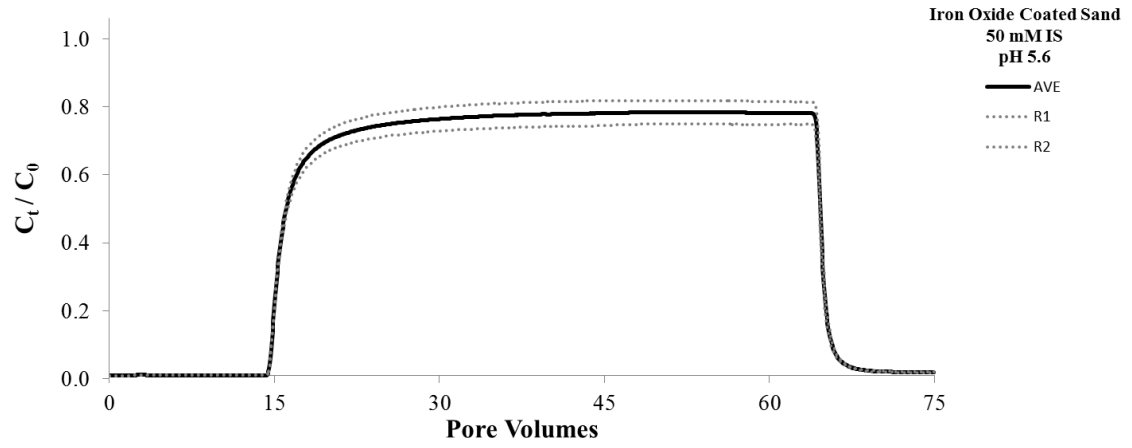
APPENDIX E:  
REPLICATE BREAKTHROUGH CURVES FOR CHAPTER 4

The following figures illustrate the duplicate (or, rarely, triplicate) breakthrough curves for each pH, ionic strength, and mineral grain treatment, which form the basis for the transport data shown in Chapter 4. In particular, the average curves from each of the following panels are presented on Figure 4.5. Experimental conditions are noted on each panel, with indicated pH values being the influent pH. Often, replicate breakthrough curves and/or average breakthrough curves cannot be discerned because they directly overlap. The timing of several important features related to these experiments is presented on Figure 4.5. We note that the abbreviation *IS* on the following panels translates to *ionic strength*.









## BIBLIOGRAPHY

- Abdelouas, A., Lutze, W., Nuttall, E., 1998. Chemical reactions of uranium in ground water at a mill tailings site. *J. Contam. Hydrol.* 34, 343–61.
- Acik, M., Mattevi, C., Gong, C., Lee, G., Cho, K., Chhowalla, M., Chabal, Y.J., 2010. The role of intercalated water in multilayered graphene oxide. *ACS Nano* 4, 5861–8.
- Alessi, D.S., Henderson, J.M., Fein, J.B., 2010. Experimental measurement of monovalent cation adsorption onto *Bacillus subtilis* cells. *Geomicrobiol. J.* 27, 464–72.
- Allen, M.J., Tung, V.C., Kaner, R.B., 2010. Honeycomb carbon: A review of graphene. *Chem. Rev.* 110, 132–45.
- Barton, C.S., Stewart, D.I., Morris, K., Bryant, D.E., 2004. Performance of three resin-based materials for treating uranium-contaminated groundwater within a PRB. *J. Hazard. Mater.* 116, 191–204.
- Beasley, T., Dixon, P., Mann, L., 1998. <sup>99</sup>Tc, <sup>236</sup>U, and <sup>237</sup>Np in the Snake river plain aquifer at the Idaho National Engineering and Environmental Laboratory, Idaho Falls, Idaho. *Environ. Sci. Technol.* 32, 3875–81.
- Bethke, C., Brady, P., 2000. How the K<sub>d</sub> approach undermines ground water cleanup. *Ground Water* 38, 435–43.
- Bradbury, M., Baeyens, B., 2002. Sorption of Eu on Na- and Ca-montmorillonites: Experimental investigations and modelling with cation exchange and surface complexation. *Geochim. Cosmochim. Acta* 66, 2325–34.
- Brodie, B., 1859. On the atomic weight of graphite. *Phil. Trans. R. Soc. Lond.* 149, 249–59.
- Cassagneau, T., Fendler, J., 1998. High density rechargeable lithium-ion batteries self-assembled from graphite oxide nanoplatelets and polyelectrolytes. *Adv. Mater.* 877–81.
- Cassagneau, T., Guérin, F., Fendler, J.H., 2000. Preparation and characterization of ultrathin films layer-by-layer self-assembled from graphite oxide nanoplatelets and polymers. *Langmuir* 16, 7318–24.

- Catalano, J.G., McKinley, J.P., Zachara, J.M., Heald, S.M., Smith, S.C., Brown, G.E., 2006. Changes in uranium speciation through a depth sequence of contaminated Hanford sediments. *Environ. Sci. Technol.* 40, 2517–24.
- Chen, C., Hu, J., Xu, D., Tan, X., Meng, Y., Wang, X., 2008. Surface complexation modeling of Sr (II) and Eu (III) adsorption onto oxidized multiwall carbon nanotubes. *J. Colloid Interface Sci.* 323, 33–41.
- Chen, C., Yang, Q.-H., Yang, Y., Lv, W., Wen, Y., Hou, P.-X., Wang, M., Cheng, H.-M., 2009. Self-assembled free-standing graphite oxide membrane. *Adv. Mater.* 21, 3007–11.
- Chisholm-Brause, C., Berg, J., Matzner, R., Morris, D., 2001. Uranium(VI) sorption complexes on montmorillonite as a function of solution chemistry. *J. Colloid Interface Sci.* 233, 38–49.
- Chowdhury, I., Duch, M.C., Mansukhani, N.D., Hersam, M.C., Bouchard, D., 2013. Colloidal properties and stability of graphene oxide nanomaterials in the aquatic environment. *Environ. Sci. Technol.* 47, 6288–96.
- Chua, C.K., Pumera, M., 2013. Chemical reduction of graphene oxide: A synthetic chemistry viewpoint. *Chem. Soc. Rev.* 43, 291–312.
- Davis, J.A., Leckie, J.O., 1978. Surface ionization and complexation at the oxide/water interface II. Surface properties of amorphous iron oxyhydroxide and adsorption of metal ions. *J. Colloid Interface Sci.* 67, 90–107.
- Dickinson, M., Scott, T.B., 2010. The application of zero-valent iron nanoparticles for the remediation of a uranium-contaminated waste effluent. *J. Hazard. Mater.* 178, 171–9.
- Dogan, A.U., Dogan, M., Onal, M., Sarikaya, Y., Aburub, A., Wurster, D.E., 2006. Baseline studies of the Clay Minerals Society source clays: Specific surface area by the Brunauer Emmett Teller (BET) method. *Clays Clay Miner.* 54, 62–66.
- Dogan, M., Dogan, A.U., Yesilyurt, F.I., Alaygut, D., Buckner, I., Wurster, D.E., 2007. Baseline studies of The Clay Minerals Society special clays: Specific surface area by the Brunauer Emmett Teller (BET) method. *Clays Clay Miner.* 55, 534–41.
- Dreyer, D.R., Park, S., Bielawski, C.W., Ruoff, R.S., 2010. The chemistry of graphene oxide. *Chem. Soc. Rev.* 39, 228–40.
- Eda, G., Fanchini, G., Chhowalla, M., 2008. Large-area ultrathin films of reduced graphene oxide as a transparent and flexible electronic material. *Nat. Nanotechnol.* 3, 270–4.

- Fein, J., Boily, J., Yee, N., Gorman-Lewis, D., Turner, B.F., 2005. Potentiometric titrations of *Bacillus subtilis* cells to low pH and a comparison of modeling approaches. *Geochim. Cosmochim. Acta* 69, 1123–32.
- Gao, W., Alemany, L.B., Ci, L., Ajayan, P.M., 2009. New insights into the structure and reduction of graphite oxide. *Nat. Chem.* 1, 403–8.
- Gao, W., Majumder, M., Alemany, L.B., Narayanan, T.N., Ibarra, M.A., Pradhan, B.K., Ajayan, P.M., 2011. Engineered graphite oxide materials for application in water purification. *ACS Appl. Mater. Interfaces* 3, 1821–6.
- Gao, Y., Li, Y., Zhang, L., Huang, H., Hu, J., Shah, S.M., Su, X., 2012. Adsorption and removal of tetracycline antibiotics from aqueous solution by graphene oxide. *J. Colloid Interface Sci.* 368, 540–6.
- Gavrilescu, M., Pavel, L.V., Cretescu, I., 2009. Characterization and remediation of soils contaminated with uranium. *J. Hazard. Mater.* 163, 475–510.
- Geim, A.K., 2011. Nobel lecture: Random walk to graphene. *Rev. Mod. Phys.* 83, 851–62.
- Ginn, B., Fein, J., 2008. The effect of species diversity on metal adsorption onto bacteria. *Geochim. Cosmochim. Acta* 72, 3939–48.
- Goldberg, S., 1992. Use of surface complexation models in soil chemical systems. *Adv. Agron.* 47, 233–329.
- Goldberg, S., 1995. Adsorption models incorporated into chemical equilibrium models. *SSSA Spec. Publ.* 42, 75–95.
- Gómez-Navarro, C., Weitz, R.T., Bittner, A.M., Scolari, M., Mews, A., Burghard, M., Kern, K., 2007. Electronic transport properties of individual chemically reduced graphene oxide sheets. *Nano Lett.* 7, 3499–503.
- Hartono, T., Wang, S., Ma, Q., Zhu, Z., 2009. Layer structured graphite oxide as a novel adsorbent for humic acid removal from aqueous solution. *J. Colloid Interface Sci.* 333, 114–9.
- Hummers Jr., W., Offeman, R., 1958. Preparation of graphitic oxide. *J. Am. Chem. Soc.* 208, 1339.
- Hyun, S.P., Fox, P.M., Davis, J.A., Campbell, K.M., Hayes, K.F., Long, P.E., 2009. Surface complexation modeling of U(VI) adsorption by aquifer sediments from a former mill tailings site at Rifle, Colorado. *Environ. Sci. Technol.* 43, 9368–73.

- Ion, A.C., Alpatova, A., Ion, I., Culetu, A., 2011. Study on phenol adsorption from aqueous solutions on exfoliated graphitic nanoplatelets. *Mater. Sci. Eng. B* 176, 588–95.
- Jaisi, D.P., Saleh, N.B., Blake, R.E., Elimelech, M., 2008. Transport of single-walled carbon nanotubes in porous media: Filtration mechanisms and reversibility. *Environ. Sci. Technol.* 42, 8317–23.
- Jaisi, D.P., Elimelech, M., 2009. Single-walled carbon nanotubes exhibit limited transport in soil columns. *Environ. Sci. Technol.* 43, 9161–6.
- Johnson, K., Szymanowski, J., Borrok, D., 2007. Proton and metal adsorption onto bacterial consortia: Stability constants for metal–bacterial surface complexes. *Chem. Geol.* 239, 13–26.
- Kim, B.H., Hong, W.G., Yu, H.Y., Han, Y.-K., Lee, S.M., Chang, S.J., Moon, H.R., Jun, Y., Kim, H.J., 2012. Thermally modulated multilayered graphene oxide for hydrogen storage. *Phys. Chem. Chem. Phys.* 14, 1480–4.
- Kipp, G.G., Stone, J.J., Stetler, L.D., 2009. Arsenic and uranium transport in sediments near abandoned uranium mines in Harding County, South Dakota. *Appl. Geochemistry* 24, 2246–55.
- Konkena, B., Vasudevan, S., 2012. Understanding aqueous dispersibility of graphene oxide and reduced graphene oxide through pKa measurements. *J. Phys. Chem. Lett.* 3, 867–72.
- Koretsky, C., 2000. The significance of surface complexation reactions in hydrologic systems: A geochemist's perspective. *J. Hydrol.* 230, 127–71.
- Kretzschmar, R., Barmettler, K., Grolimund, D., Yan, Y., Borkovec, M., Sticher, H., 1997. Experimental determination of colloid deposition rates and collision efficiencies in natural porous media. *Water Resour. Res.* 33, 1129–37.
- Kretzschmar, R., Borkovec, M., Grolimund, D., Elimelech, M., 1999. Mobile subsurface colloids and their role in contaminant transport. *Adv. Agron.* 66, 121–93.
- Lanphere, J., Luth, C., Walker, S., 2013. Effects of solution chemistry on the transport of graphene oxide in saturated porous media. *Environ. Sci. Technol.* 47, 4255–61.
- Lee, D.W., De Los Santos V, L., Seo, J.W., Leon Felix, L., Bustamante D.A., Cole, J.M., Barnes, C.H.W., 2010. The structure of graphite oxide: Investigation of its surface chemical groups. *J. Phys. Chem. B* 114, 5723–8.
- Lerf, A., He, H., Forster, M., Klinowski, J., 1998. Structure of graphite oxide revisited. *J. Phys. Chem. B* 102, 4477–82.

- Li, D., Müller, M.B., Gilje, S., Kaner, R.B., Wallace, G.G., 2008. Processable aqueous dispersions of graphene nanosheets. *Nat. Nanotechnol.* 3, 101–5.
- Liu, Z., Wang, Z.-M., Yang, X., Ooi, K., 2002. Intercalation of organic ammonium ions into layered graphite oxide. *Langmuir* 18, 4926–32.
- Liu, Q., Shi, J., Sun, J., Wang, T., Zeng, L., Jiang, G., 2011. Graphene and graphene oxide sheets supported on silica as versatile and high-performance adsorbents for solid-phase extraction. *Angew. Chem. Int. Ed. Engl.* 50, 5913–7.
- Loh, K.P., Bao, Q., Eda, G., Chhowalla, M., 2010. Graphene oxide as a chemically tunable platform for optical applications. *Nat. Chem.* 2, 1015–24.
- Lü, K., Zhao, G., Wang, X., 2012. A brief review of graphene-based material synthesis and its application in environmental pollution management. *Chinese Sci. Bull.* 57, 1223–34.
- Marmier, N., Delisée, A., Fromage, F., 1999. Surface complexation modeling of Yb(III), Ni(II), and Cs(I) sorption on magnetite. *J. Colloid Interface Sci.* 211, 54–60.
- Martell, A.E., Smith, R.M., 1977. *Critical Stability Constants*. Plenum, New York, USA.
- Morrison, S.J., Spangler, R.R., 1992. Extraction of uranium and molybdenum from aqueous solutions: A survey of industrial materials for use in chemical barriers for uranium mill tailings remediation. *Environ. Sci. Technol.* 26, 1922–31.
- Murphy, R.J., Lenhart, J.J., Honeyman, B.D., 1999. The sorption of thorium (IV) and uranium (VI) to hematite in the presence of natural organic matter. *Colloids Surfaces A: Physicochem. Eng. Asp.* 157, 47–62.
- Nakajima, T., Matsuo, Y., 1994. Formation process and structure of graphite oxide. *Carbon* 32, 469–475.
- Novoselov, K.S., Geim, A.K., Morozov, S.V., Jiang, D., Zhang, Y., Dubonos, S. V., Grigorieva, I. V, Firsov, A.A., 2004. Electric field effect in atomically thin carbon films. *Science* 306, 666–9.
- Pagnanelli, F., Bornoroni, L., Moscardini, E., Toro, L., 2006. Non-electrostatic surface complexation models for protons and lead (II) sorption onto single minerals and their mixture. *Chemosphere* 63, 1063–73.
- Park, S., Ruoff, R.S., 2009. Chemical methods for the production of graphenes. *Nat. Nanotechnol.* 4, 217–24.

- Peigney, A., Laurent, C., Flahaut, E., Bacsa, R.R., Rousset, A., 2001. Specific surface area of carbon nanotubes and bundles of carbon nanotubes. *Carbon* 39, 507–14.
- Petit, C., Seredych, M., Bandosz, T.J., 2009. Revisiting the chemistry of graphite oxides and its effect on ammonia adsorption. *J. Mater. Chem.* 19, 9176–85.
- Redman, J.A., Walker, S.L., Elimelech, M., 2004. Bacterial adhesion and transport in porous media: Role of the secondary energy minimum. *Environ. Sci. Technol.* 38, 1777–85.
- Ren, X., Wang, S., Yang, S., Li, J., 2009. Influence of contact time, pH, soil humic/fulvic acids, ionic strength and temperature on sorption of U(VI) onto MX-80 bentonite. *J. Radioanal. Nucl. Chem.* 283, 253–59.
- Ryan, J.N., Elimelech, M., 1996. Colloid mobilization and transport in groundwater. *Colloids Surfaces A: Physicochem. Eng. Asp.* 107, 1–56.
- Seredych, M., Bandosz, T.J., 2007. Removal of ammonia by graphite oxide via its intercalation and reactive adsorption. *Carbon* 45, 2130–32.
- Seredych, M., Petit, C., Tamashausky, A. V., Bandosz, T.J., 2009. Role of graphite precursor in the performance of graphite oxides as ammonia adsorbents. *Carbon* 47, 445–56.
- Shock, E., Koretsky, C., 1995. Metal-organic complexes in geochemical processes: Estimation of standard partial molal thermodynamic properties of aqueous complexes between metal cations and monovalent organic acid ligands at high pressures and temperatures. *Geochim. Cosmochim. Acta* 59, 1497–532.
- Sitko, R., Turek, E., Zawisza, B., Malicka, E., Talik, E., Heimann, J., Gagor, A., Feist, B., Wrzalik, R., 2013. Adsorption of divalent metal ions from aqueous solutions using graphene oxide. *Dalton Trans.* 42, 5682–9.
- Smith, J., Gao, B., Funabashi, H., Tran, T.N., Luo, D., Ahner, B.A., Steenhuis, T.S., Hay, A.G., Walter, M.T., 2008. Pore-scale quantification of colloid transport in saturated porous media. *Environ. Sci. Technol.* 42, 517–23.
- Song, L., Elimelech, M., 1993. Dynamics of colloid deposition in porous media: Modeling the role of retained particles. *Colloids Surfaces A: Physicochem. Eng. Asp.* 73, 49–63.
- Stankovich, S., Dikin, D.A., Piner, R.D., Kohlhaas, K.A., Kleinhammes, A., Jia, Y., Wu, Y., Nguyen, S.T., Ruoff, R.S., 2007. Synthesis of graphene-based nanosheets via chemical reduction of exfoliated graphite oxide. *Carbon* 45, 1558–65.

- Stubbs, J.E., Elbert, D.C., Veblen, D.R., Zhu, C., 2006. Electron microbeam investigation of uranium-contaminated soils from Oak Ridge, TN, USA. *Environ. Sci. Technol.* 40, 2108–113.
- Sun, Y., Wang, Q., Chen, C., Tan, X., Wang, X., 2012. Interaction between Eu(III) and graphene oxide nanosheets investigated by batch and extended X-ray absorption fine structure spectroscopy and by modeling techniques. *Environ. Sci. Technol.* 46, 6020–7.
- Sylwester, E., Hudson, E., Allen, P., 2000. The structure of uranium(VI) sorption complexes on silica, alumina, and montmorillonite. *Geochim. Cosmochim. Acta* 64, 2431–8.
- Szabó, T., Berkesi, O., Forgó, P., 2006a. Evolution of surface functional groups in a series of progressively oxidized graphite oxides. *Chem. Mater.* 18, 2740–9.
- Szabó, T., Tombácz, E., Illés, E., Dékány, I., 2006b. Enhanced acidity and pH-dependent surface charge characterization of successively oxidized graphite oxides. *Carbon* 44, 537–45.
- Tong, M., Ding, J., Shen, Y., Zhu, P., 2010. Influence of biofilm on the transport of fullerene (C60) nanoparticles in porous media. *Water Res.* 44, 1094–103.
- Turner, G.D., Zachara, J.M., McKinley, J.P., Smith, S.C., 1996. Surface-charge properties and  $\text{UO}_2^{2+}$  adsorption of a subsurface smectite. *Geochim. Cosmochim. Acta* 60, 3399–414.
- Waite, T., Davis, J., Payne, T., 1994. Uranium(VI) adsorption to ferrihydrite: Application of a surface complexation model. *Cosmochim. Acta.* 58, 5465–78.
- Wang, G., Yang, J., Park, J., Gou, X., Wang, B., Liu, H., Yao, J., 2008. Facile synthesis and characterization of graphene nanosheets. *J. Phys. Chem. C* 112, 8192–5.
- Wang, Y., Li, Z., Wang, J., Li, J., Lin, Y., 2011. Graphene and graphene oxide: Biofunctionalization and applications in biotechnology. *Trends Biotechnol.* 29, 205–12.
- Westall, J.C., 1982. FITEQL: A Computer Program for the Determination of Chemical Equilibrium Constants from Experimental Data, Version 2.0, Report 82-02; Department of Chemistry, Oregon State University.
- Westall, J.C., Jones, J., 1995. Models for association of metal ions with heterogeneous environmental sorbents. 1. Complexation of Co (II) by leonardite humic acid as a function of pH and  $\text{NaClO}_4$ . *Environ. Sci. Technol.* 29, 951–9.

- Yang, S.-T., Chang, Y., Wang, H., Liu, G., Chen, S., Wang, Y., Liu, Y., Cao, A., 2010. Folding/aggregation of graphene oxide and its application in Cu<sup>2+</sup> removal. *J. Colloid Interface Sci.* 351, 122–7.
- Yang, S., Hu, J., Chen, C., Shao, D., Wang, X., 2011. Mutual effects of Pb(II) and humic acid adsorption on multiwalled carbon nanotubes/polyacrylamide composites from aqueous solutions. *Environ. Sci. Technol.* 45, 3621–7.
- Yao, K., Habibian, M., O'Melia, C., 1971. Water and waste water filtration. Concepts and applications. *Environ. Sci. Technol.* 5, 1105–12.
- Zhang, Y., Small, J.P., Pontius, W. V., Kim, P., 2005. Fabrication and electric-field-dependent transport measurements of mesoscopic graphite devices. *Appl. Phys. Lett.* 86, 073104.
- Zhang, J., Yang, H., Shen, G., Cheng, P., Zhang, J., Guo, S., 2010. Reduction of graphene oxide via L-ascorbic acid. *Chem. Commun.* 46, 1112–4.
- Zhang, W., Zhou, C., Zhou, W., Lei, A., 2011. Fast and considerable adsorption of methylene blue dye onto graphene oxide. *Bull. Environ. Contam. Tox.* 87, 86–90.
- Zhao, G., Li, J., Ren, X., Chen, C., Wang, X., 2011a. Few-layered graphene oxide nanosheets as superior sorbents for heavy metal ion pollution management. *Environ. Sci. Technol.* 45, 10454–62.
- Zhao, G., Ren, X., Gao, X., Tan, X., Li, J., Chen, C., Huang, Y., Wang, X., 2011b. Removal of Pb(II) ions from aqueous solutions on few-layered graphene oxide nanosheets. *Dalton Trans.* 40, 10945–52.
- Zhao, G., Wen, T., Yang, X., Yang, S., Liao, J., Hu, J., Shao, D., Wang, X., 2012. Preconcentration of U(VI) ions on few-layered graphene oxide nanosheets from aqueous solutions. *Dalton Trans.* 41, 6182–8.
- Zhu, Y., Murali, S., Cai, W., Li, X., Suk, J.W., Potts, J.R., Ruoff, R.S., 2010. Graphene and graphene oxide: Synthesis, properties, and applications. *Adv. Mater.* 22, 3906–24.